



Saku Levikari

# ACOUSTIC EMISSION TESTING OF MULTILAYER CERAMIC CAPACITORS



Saku Levikari

## **ACOUSTIC EMISSION TESTING OF MULTILAYER CERAMIC CAPACITORS**

Dissertation for the degree of Doctor of Science (Technology) to be presented with due permission for public examination and criticism in the Viipuri Hall at Lappeenranta–Lahti University of Technology LUT, Lappeenranta, Finland, on the 25<sup>th</sup> of March, 2022, at noon.

Acta Universitatis  
Lappeenrantaensis 1011

Supervisors	Professor Pertti Silventoinen LUT School of Energy Systems Lappeenranta–Lahti University of Technology LUT Finland
	Tommi J. Kärkkäinen, D.Sc. (Tech.) LUT School of Energy Systems Lappeenranta–Lahti University of Technology LUT Finland
Reviewers	Professor Huai Wang The Faculty of Engineering and Science Aalborg University Denmark
	Professor Daswin De Silva Centre for Data Analytics and Cognition La Trobe University Australia
Opponent	Laura Frisk, D.Sc (Tech.) CEO Trelic Oy Finland

ISBN 978-952-335-779-2  
ISBN 978-952-335-780-8 (PDF)  
ISSN-L 1456-4491  
ISSN 1456-4491

Lappeenranta–Lahti University of Technology LUT  
LUT University Press 2022

# Abstract

**Saku Levikari**

**Acoustic Emission Testing of Multilayer Ceramic Capacitors**

Lappeenranta 2022

90 pages

Acta Universitatis Lappeenrantaensis 1011

Diss. Lappeenranta–Lahti University of Technology LUT

ISBN 978-952-335-779-2, ISBN 978-952-335-780-8 (PDF)

ISSN-L 1456-4491, ISSN 1456-4491

Capacitors are among the three fundamental passive electrical components alongside inductors and resistors. They are found in nearly every electronic circuit, with the function of storing electrical energy and filtering out unwanted components within electric signals or currents. In recent years, the usage of electronics devices has seen an exponential growth, even to a degree that has led to component shortages. The increasing reliance on electronics across industrial and automotive electronics, residential sectors, and consumer devices places an emphasis on the reliability of electrical devices, in which capacitors play a key role. In an electronic device, a failing capacitor can cause unexpected behavior or result in a total failure of the device, which can result in a costly or dangerous situation, especially if the said device happens to play a crucial role, e.g., in an industrial plant or an airliner.

The multilayer ceramic capacitor (MLCC) is the most widely used capacitor type across the electronics industry, with several trillions of units produced annually. The MLCC has become a preferred choice both in consumer and power electronics owing to its favorable electrical characteristics and a small yet efficient form factor. However, the design of the MLCC has its downsides, most notably a brittle structure that is prone to mechanical damage, such as cracks. For failures in electrical devices, capacitors have been estimated to be the culprit in 30% of the cases, and for MLCCs over half of the failures result from hidden cracks that are left undetected on the production line, but cause a sudden failure in the field.

Although new MLCCs can be electrically tested before being installed onto the circuit board, a majority of hidden damage is caused by subsequent tasks on the assembly line. Excess thermal or physical stress from soldering or improper handling of circuit board assemblies can cause cracks or delamination, which may not affect the electrical operation of the component at first, but can cause premature failure in the field. Thus, such types of damage are very challenging to be detected, especially after the electrical device has been assembled.



This doctoral dissertation proposes a new, nondestructive technique for identifying latent damage, such as cracks in MLCCs at the end of the assembly line. The method takes advantage of the piezoelectric effect inherent to most MLCC designs: under electrical excitation, the body of the MLCC starts to vibrate. By measuring the vibrational characteristics of the component by using a contact sensor, hidden structural faults can be detected. Experimental acoustic measurements are performed on hundreds of intact and damaged MLCCs, and signal processing techniques are developed for the acoustic data.

Furthermore, the applicability of the method to assembly line use is considered by developing a machine learning classification system that can reliably discriminate faulty components from intact ones. Methods are developed that allow the classifier system to be trained solely on intact samples, making the method applicable in a production environment.

**Keywords:** ceramic capacitors, nondestructive testing, acoustic measurements, machine learning, one-class learning

# Acknowledgments

In 2015, I started working on my master's thesis in Lappeenranta University of Technology on the topic of acoustic emission measurements for MLCCs. The research, carried out in the Laboratory of Applied Electronics in collaboration with ABB, eventually became the basis of this dissertation.

I would like to express my gratitude to Dr. Caroline Andersson at ABB Switzerland and Mr. Juha Tamminen at ABB Drives, who were in a key role in organizing and conducting experimental work during this research. Your contribution to each of the articles in this dissertation has been invaluable. Also, a big thank you to Mr. Kjell Inman, Mr. Martti Mattila, and everybody else at ABB who helped to make this dissertation a reality.

I want to thank professor Huai Wang and professor Daswin De Silva for reviewing and commenting upon this dissertation, an effort which truly helped to refine this work.

Special thanks to my supervisor, professor Pertti Silventoinen, for providing an environment where one can easily focus on conducting research, without having to worry about bureaucratic obstacles. Working under your guidance has been a pleasure.

I would like to express my gratitude to my supervisor Dr. Tommi Kärkkäinen for continuous guidance throughout this entire work. I would also like to thank each and every one of my colleagues at 6405, past and present: Dr. Juhamatti Korhonen, Dr. Raimo Juntunen, Dr. Heikki Järvisalo, Dr. Jari Honkanen, Dr. Janne Hannonen, Mr. Henri M. Aalto, Mr. Antti Immonen, Mr. Janne Jäppinen, Ms. Katriina Korpinen, Mr. Mikko Nykyri, Mr. Juuso Rautio, Mr. Otto Salminen and Mr. Jesse Tolvanen. With all the absurd coffee table conversations (badness 10000), you have created a truly unique working environment.

I am particularly grateful to Dr. Hanna Niemelä, who time after time provided her assistance to improve the language of this dissertation.

I wish to thank my parents, Askö, Leena, and Jussi, as well as my brother, Juuso, for all the support they have provided throughout my life. Finally, I would like to express my deepest gratitude to my wife, Milla, for her endless support and encouragement throughout my studies and career. Also, very special thanks to our cat, Vilma, who slept on my lap most of the nights in February–April of 2021 when I wrote the majority of this dissertation.

Lappeenranta, December 16<sup>th</sup>, 2021

Saku Levikari



*Never follow the crowd, go where it's empty*

— Arnold Schwarzenegger



# Contents

<b>Abstract</b>	<b>3</b>
<b>Acknowledgments</b>	<b>5</b>
<b>Contents</b>	<b>9</b>
<b>Nomenclature</b>	<b>11</b>
<b>List of publications</b>	<b>15</b>
<b>1 Introduction</b>	<b>17</b>
1.1 Multilayer Ceramic Capacitors . . . . .	18
1.2 MLCC screening methods . . . . .	20
1.2.1 Optical methods . . . . .	21
1.2.2 Acoustic methods . . . . .	21
1.3 Scope of the dissertation . . . . .	22
<b>2 Research methods</b>	<b>25</b>
2.1 Acoustic emission testing . . . . .	25
2.1.1 Acoustic emissions in MLCCs . . . . .	25
2.2 Overview of the research methods . . . . .	26
<b>3 Measurements and data preprocessing</b>	<b>29</b>
3.1 Acoustic measurements . . . . .	29
3.2 Acoustic characterization process and instrumentation . . . . .	32
3.3 MLCC sample inspection and labeling . . . . .	35
3.4 Signal preprocessing . . . . .	39
<b>4 Feature extraction</b>	<b>43</b>
4.1 Amplitude and frequency . . . . .	44
4.2 Phase . . . . .	45
4.3 Feature exploration . . . . .	45
4.4 Acoustic data set . . . . .	49
<b>5 Analysis and classification methods</b>	<b>53</b>
5.1 Distance-based comparison of acoustic signals . . . . .	53
5.2 Machine learning classifiers . . . . .	55
5.2.1 Support vector machine . . . . .	58
5.2.2 One-class support vector machine . . . . .	59
5.2.3 OSVM hyperparameter optimization . . . . .	60

5.2.4	Cliffhanger algorithm . . . . .	61
5.3	Evaluation methods . . . . .	66
5.3.1	Confusion river graph . . . . .	67
<b>6</b>	<b>Results and discussion</b>	<b>69</b>
6.1	OSVM test protocol . . . . .	69
6.2	OSVM test results . . . . .	70
6.2.1	Overview . . . . .	70
6.2.2	Further analysis . . . . .	71
6.2.3	Comparison with binary classifiers . . . . .	76
<b>7</b>	<b>Conclusions and future research</b>	<b>79</b>
7.1	Future work . . . . .	80
	<b>References</b>	<b>83</b>
	<b>Publications</b>	<b>91</b>

# Nomenclature

## Roman letters

$A$	Amplitude
$b$	Bias term of SVM decision plane
$C$	Capacitance
$c$	Chirp (frequency sweep)
$D$	Number of dimensions
$E$	Electric field
$e$	Amplitude envelope
$f$	Frequency
$i, j$	Vector or matrix indices
$m$	Median
$N$	Number of data points
$P$	Polarization
$v$	Error vector
$\mathbf{w}$	Normal vector of SVM decision plane
$W$	Weight matrix
$x$	Data point (vector)

## Greek letters

$\alpha$	Support vector weight
$\epsilon$	Absolute permittivity
$\epsilon_0$	Vacuum permittivity
$\gamma$	SVM gaussian kernel bandwidth hyperparameter
$\kappa$	Kernel function
$\mu$	Arithmetic mean
$\nu$	SVM regularizer hyperparameter
$\Phi$	A mapping between two sets
$\phi$	Phase
$\sigma$	Standard deviation
$\theta$	Linear regression parameter vector

## Subscripts

c	Critical point
ref	Reference



## Superscripts

T	Matrix transpose
---	------------------

## Other symbols

diag	Diagonal matrix
$\hat{\theta}$	Estimate of $\theta$
$\mathcal{H}$	Hilbert transformation
$\langle \cdot, \cdot \rangle$	Inner product
lpf	Lowpass filter
$\mu\text{Str}$	Microstrain
$n_{\text{grid}}$	Number of grid points per axis in grid search
$\mathbb{R}$	Real numbers
$Re$	Real part of a complex number
sgn	Signum function

## Acronyms

A	Accuracy matrix
AC	Alternating current
ANN	Artificial neural network
AUC	Area under curve
BaTiO <sub>3</sub>	Barium titanate (ceramic dielectric)
C-scan	Two-dimensional ultrasound imaging method
CNN	Convolutional neural network
CR	Confusion river graph
DS	Downsampling
EMI	Electromagnetic interference
FN	False negative
FNN	Feedforward neural network
FP	False positive
FPR	False positive rate
GDR	Group delay ripple
GLS	Generalized least squares
$k$ -NN	$k$ -nearest neighbors
LOOCV	Leave-one-out cross-validation
LSTM	Long short-term memory recurrent neural network
MCC	Matthews correlation coefficient
MLCC	Multilayer ceramic capacitor
NDT	Nondestructive testing
OSVM	One-class support vector machine
PCA	Principal component analysis
PCB	Printed circuit board

RBF	Radial basis function
RF	Random forest
SOM	Self-organizing map
SV	Set of support vectors
SVM	Support vector machine
TN	True negative
TNR	True negative rate
TP	True positive
TPR	True positive rate



# List of publications

The results of this study are documented in the following three scientific journal articles. The rights have been granted by the publishers to include the publications in the dissertation.

## **Publication I**

Levikari, S., Kärkkäinen, T., Andersson, C., Tamminen, J., and Silventoinen, P. (2018), "Acoustic Phenomena in Damaged Ceramic Capacitors," *IEEE Transactions on Industrial Electronics*, Vol. 61, Iss. 1, pp. 570–577.

## **Publication II**

Levikari, S., Kärkkäinen, T., Andersson, C., Tamminen, J., and Silventoinen, P. (2019), "Acoustic Detection of Cracks and Delamination in Multilayer Ceramic Capacitors," *IEEE Transactions on Industry Applications*, Vol. 55, Iss. 2, pp. 1787–1794.

## **Publication III**

Levikari, S., Kärkkäinen, T., Andersson, C., Tamminen, J., and Silventoinen, P. (2020), "Nondestructive Acoustic Testing of Ceramic Capacitors using One-Class Support Vector Machine with Automated Hyperparameter Selection," *IEEE Access*, Online, Vol. 8, pp. 226337–226351.

## **Author's contribution**

In **Publication I**, the author was responsible for performing the literature review, developing the acoustic measurement technique, designing and constructing the measurement setup, performing the acoustic measurements, developing the analytics methods, and performing the analyses on the acoustic data. He was also the corresponding author for the publication.

In **Publication II**, the author was responsible for performing the literature review, analyzing the X-ray and cross-section images provided by ABB, developing preprocessing and denoising techniques for the measurement data, performing feature extraction and statistical analysis on the data, and developing and testing the machine learning classifier on the data. He was also the corresponding author for the publication.

In **Publication III**, the author was responsible for performing the literature review, developing the technique for extracting phase information from the acoustic signals, developing feature extraction techniques for the acoustic data, developing and testing the hyperparameter optimization algorithm, and performing the analysis on the acoustic data. He was also the corresponding author for the publication.

# 1 Introduction

The ongoing energy transition has resulted in an exponential growth in the market for electrical and electronic devices. On the global scale of energy generation and consumption, the role of electricity is expected to increase from the current 21% to over 50% by 2050 (IRENA, 2021). This change is reflected especially in the market for power electronics.

The purpose of power electronics is to supply the load (e.g., an electric motor) with an optimal flow of electrical energy (Mohan et al., 2003). This is achieved by using devices that perform conversions between alternating current (AC) and direct current (DC), i.e., power electronic converters. Power electronics are becoming more prominent in renewable energy production (Randall et al., 2016) and are used for a wide range of applications across residential, commercial, industrial, transportation, and other sectors (Mohan et al., 2003). Power electronic converters have largely superseded older technologies based on linear electronics, such as transformers, owing to improvements in efficiency, size, weight, and cost (Mohan et al., 2003). Today, approximately 80% of all electricity passes through power electronic devices, and this number is expected to ultimately reach 100% (Kumar et al., 2020).

As modern society becomes increasingly dependent on electronics, the reliability of the technology becomes more crucial. Abrupt failures of electronics, power electronics in particular, cause costly repairs, downtime, and in worst cases, even life-threatening situations. For example, on-premises power failures have been listed as the leading cause for data center outages (Lawrence and Ascierto, 2018), the cost of which can exceed \$ 500 000 per hour (Ponemon Institute, 2016). On the other hand, the average failure rate for consumer electronics has been estimated to be approximately 15% by the fourth year of operation (Consumer Reports, 2006), with computers and laptops exceeding 30% (Consumer Reports, 2011).

While an electronic device can fail for countless reasons, it has been estimated that approximately 30% of failures can be traced back to capacitors (Sood, 2013). Capacitors are one of the three fundamental passive electronic components along with resistors and inductors. Their function is to store electric energy in the form of an electric field, and they are often used as fast energy storages or for filtering out unwanted components in electric signals.

A failing capacitor can cause damage to other components within the electronic device, which may result in abnormal or degraded performance, or even a total failure of the device. One way of preventing such failures is to screen the capacitors of the device on the production line, revealing defective components before the device enters the field. Unfortunately, not every type of fault can be detected by using the current testing methods, which results in unexpected and costly field failures. As more and more capacitors are being deployed in electronic systems, new quality assurance methods are needed.

In the focus of this dissertation is a type of capacitor known as the multilayer ceramic capacitor (MLCC) and challenges associated with it, especially stress-related mechanical damage during assembly. Such types of latent damage are especially problematic, because often they do not initially affect the electrical properties of the capacitor, thus passing conventional electrical quality assurance tests undetected. However, when the device is taken to field use, the size of the fault within the capacitor can grow, resulting in an abrupt failure of the component. As a solution, a new nondestructive quality assurance testing method for MLCCs is introduced, capable of revealing types of latent damage that could evade conventional electrical tests.

## 1.1 Multilayer Ceramic Capacitors

Multilayer ceramic capacitor (MLCC) is the most widely used capacitor type in the electronics industry, with more than  $10^{12}$  units produced annually (Ho et al., 2010). The demand for MLCCs has seen a dramatic increase over the last decade leading to shortages of components, with miniature capacitors being used in consumer electronics and automotive industry, and larger ones being deployed in industrial applications and power electronics (Zogbi, 2018; Carbone, 2018; James, 2018).

The popularity of the MLCC is due to its high capacitance per volume and favorable high-frequency characteristics (Ko et al., 2014), combined with a monolithic, surface-mount design. These properties are achieved by the structure of the MLCC, which consists of stacked electrodes with a ceramic dielectric in between as shown in Fig. 1.1. The stacked structure facilitates a high electrode surface area per volume, and the high permittivity of the ceramic dielectric material allows for a very thin dielectric layer between the electrodes, with the thickness below one micrometer (Hahn et al., 2007).

MLCCs are commonly divided into three classes based on the type of the ceramic dielectric material (Kemet Electronics Corporation, 2020). Class I MLCCs use mainly calcium zirconate, which gives these capacitors stable capacitance across a wide temperature range, albeit with a relatively low capacitance. On the other hand, the dielectrics in class II and the rarely used class III MLCCs are based on barium titanate ( $\text{BaTiO}_3$ ), which gives the capacitors high permittivity and capacitance, but the capacitance is more strongly dependent on temperature than in class I MLCCs. Thus, class I MLCCs are

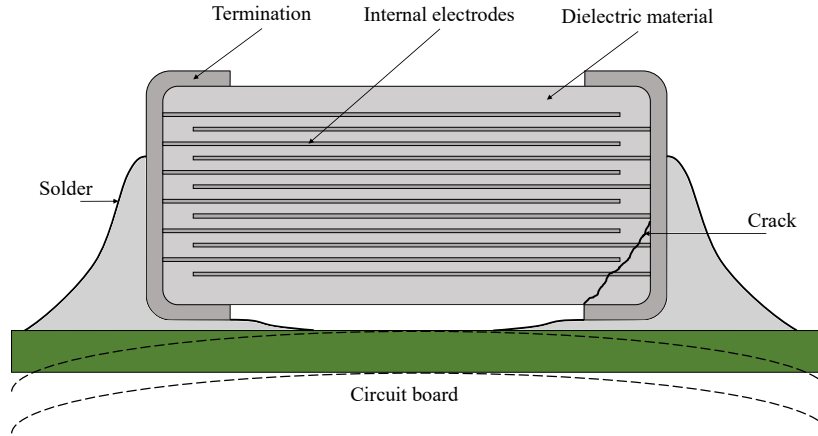


Figure 1.1. Schematic of the structure of an MLCC.

typically found in applications that require high temperature stability, whereas class II MLCCs are more common for smoothing, bypass, coupling, and decoupling applications (IEC 60384-1:2016). This doctoral dissertation focuses on class II capacitors, which often play a vital role in power electronic systems. For example, if an MLCC being used as a bypass capacitor fails in the open circuit mode, the quality of the input voltage for the system declines. On the other hand, a failure in the short-circuit mode results in a total loss of input voltage.

While the use of ceramic  $\text{BaTiO}_3$  as the material for the body of class II MLCCs facilitates high permittivity and capacitance per volume, it also makes the components vulnerable to mechanical damage, as the brittle ceramic material can fracture under external force. Cracks have been identified as the most prevalent failure mode in MLCCs (Teverovsky, 2018), e.g., from physical mishandling of PCB assemblies on the production line. Certain applications also require manual soldering of MLCCs, which increases the risk of fracture as a result of uneven thermal expansion (Teverovsky, 2018). In particular, MLCCs with larger case sizes (1812 and up) have been shown to be vulnerable to bending-related cracks (Keimasi et al., 2008), and material or manufacturing defects are also likely to elevate the risk of mechanical damage (Teverovsky, 2018).

Excess thermal or mechanical stresses often result in cracks within the dielectric material, propagating from the end terminations toward the ceramic body of the component. Another example of stress-induced damage is delamination between the internal electrodes and the dielectric material, or between the capacitor body and its end terminations or solder joints (Ahmar and Wiese, 2015). Cracks in the ceramic body can be observed in electrical tests as a reduced capacitance, if the crack cuts off some of the internal electrodes. On the other hand, smaller cracks or delaminations residing in the ceramic body itself are more difficult to detect, because the component may display normal characteristics in the electrical testing. However, when the device is taken to operational use, such



faults can grow over time because of thermal and electrical stresses. This can result in a decrease in capacitance or an open circuit if the crack cuts through all the electrodes. Furthermore, in humid environments, water penetrating the capacitor body through a crack can deteriorate the dielectric material (Wang et al., 2003). Metal migration from the end terminations by dendritic growth can also cause the capacitor to short-circuit (Teverovsky, 2018). Similarly, oxygen vacancy migration has been observed to deteriorate the dielectric material in high electrode density MLCCs, although this phenomenon is related to the high temperature associated with the manufacturing process of the capacitor instead of mechanical stress (Brown, 2018). Such faults can eventually lead to a malfunction or a premature failure of the electronic device, depending on the role of the malfunctioning capacitor.

Although the probability of a field failure of a single MLCC is extremely small, they do frequently occur because of the sheer number of capacitors in use. As a recent example, MLCC thermal cracking was found to be the root cause for field failures for a series of pacemakers manufactured between 2017 and 2019. With a calculated rate of occurrence of only 0.006%, nine failures were reported, one of which contributed to a patient death (Medtronic, 2019). MLCCs have also been identified as the root cause of early-life failure in applications where mechanical forces, vibration, or extreme temperature changes are common, such as automotive electronics (Jacob, 2016), oil industry (Bescup, 2016), and computer hardware (Wallossek, 2020).

## 1.2 MLCC screening methods

Screening for faulty components at the production line level is an effective way of avoiding early failures of electronic devices (U.S. Department of Defense, 1988). Common production line screening methods on MLCCs include electrical tests for capacitance and insulation resistance, performed on procurement lots before assembly (Teverovsky, 2012). However, over 50% of cracks in MLCCs can be traced back to the PCB assembly process (Lambert, 2014), which will occur after the electrical tests have taken place. Moreover, latent damage, such as cracks in the passive region of the dielectric material, can evade conventional electrical tests, as the fault does not extend to the active area of the capacitor body. Thus, there is a need for a nondestructive testing (NDT) method for the detection of such latent damage in MLCCs.

Latent damage in MLCCs is a well-known problem that has been a subject of study since the 1970s (Teverovsky, 2018). While there are common quality assurance methods, such as electrical testing, optical inspection, and noncontact ultrasound imaging, these techniques are typically used to screen out manufacturing defects within the components, rather than using them for assembled devices at the end of the production line (Teverovsky, 2018). Moreover, the ability of these methods to detect internal damage such as cracks and delamination is limited: optical inspection only reaches the surface of

the capacitor, and the resolution of C-scan ultrasound imaging has only allowed the detection of vertically spanning faults (Teverovsky, 2018). In addition to the aforementioned screening techniques, various approaches based on optical and acoustic measurements have been proposed.

### 1.2.1 Optical methods

Different optical imaging techniques have been widely studied for MLCC quality assurance purposes. For instance, Chan et al. (1995, 2000) developed a method based on laser speckle measurement, which detects the deformation of the capacitor body caused by Joule heating under DC tests. However, it is unclear whether the method is applicable to defects strictly in the passive region of the component. More conventional X-ray imaging techniques have also gained interest recently, as the accuracy of the 2D and 3D imaging methods has increased enough to facilitate the detection of cracks (Andersson et al., 2016) and breakdown defects within the dielectric (Ingman et al., 2019). Other methods, such as neutron radiography (Kieran, 1981), have also been proposed in the past.

### 1.2.2 Acoustic methods

In addition to electrical testing and optical imaging, various acoustic techniques have been studied for the screening task, likely the most widely used one being ultrasound imaging. While this technique has traditionally been limited to larger, horizontal damages, a newer ultrasonic microscopy technique capable of detecting vertically spanning cracks has been developed (Adams, 2009). However, it is infeasible for production line use as the method requires submerging the component in water, and thus, it is mainly used in research and development. Moreover, ultrasound methods are limited to regions not covered by the metal end terminations (Teverovsky, 2018), where the cracks often originate from. In addition to acoustic imaging, methods based on observing the mechanical and resonance characteristics of the MLCC body have been proposed. For instance, Kahn and Checkaneck (1983) placed MLCCs under a mechanical ram equipped with an ultrasound transducer to observe the acoustic emissions from the cracking of the dielectric. Later, the laser-induced vibration testing technique by Erdahl and Ume (2004, 2005) was able to detect flex cracks in MLCCs of sizes 0603 and 0805. However, the applicability to larger case sizes, which are more prone to flex cracks, is unknown.

Some of the screening methods proposed in the past have taken advantage of the piezoelectric properties of  $\text{BaTiO}_3$ , the dielectric material used in class II MLCCs. For example, Bechou et al. (1996) used radio-frequency tone bursts to excite DC-biased MLCCs to vibration and observed the subsequent decay by using electrical measurements. The mechanical resonance modes of the ceramic body of the capacitor could be observed as peaks within the impedance curve of the component. Johnson et al. (2014, 2017) subjected ca-

capacitors to AC voltage at radio frequencies and observed changes in the amplitude and phase of the capacitor body by using an ultrasound transducer. The piezoelectric properties of  $\text{BaTiO}_3$  are also the basis of the screening method proposed in this dissertation.

### 1.3 Scope of the dissertation

The objective of this dissertation was to investigate whether acoustic measurement techniques could be employed in screening MLCCs for structural damage in a nondestructive manner. As a result, this dissertation presents a new, nondestructive method for screening out latent mechanical damages in class II MLCCs. The method can be applied to soldered capacitors at the end of a production line, where the risk of damage caused by mechanical impacts and stress is high.

The main scientific contribution of this dissertation is the introduction of an acoustic measurement technique for MLCCs, along with the development of computational methods for identifying damaged capacitors based on acoustic emission data. Noise and artifacts contained within the acoustic signals are identified as major challenges to the acoustic screening technique. To this end, filtering and preprocessing techniques are developed for acoustic measurement data. Furthermore, in order to achieve reliable, automated identification of damaged MLCCs, classification methods for acoustic data are required. As a solution, a data pipeline consisting of feature extraction methods and a machine learning classifier is presented. An optimization algorithm is developed for the classifier, facilitating training of the machine learning model using only dozens of intact MLCCs as examples. Based on experimental data, the proposed approach is capable of identifying at least two-thirds of damaged components, while maintaining a low 3% rate of false alarms on intact capacitors.

In **Publication I**, the concept of measuring acoustic emissions from MLCCs under AC voltage excitation with a point-contact sensor is presented. Acoustic measurements are performed on two intact test circuit boards populated with MLCCs of various case sizes and capacitance values. The test boards are then subjected to controlled bending to inflict mechanical damage to the MLCCs, and the acoustic measurements are then repeated. The capacitor samples are inspected using X-ray imaging and cross-section microscopy to reveal which components had suffered cracks or delamination from the bending. Correlation between changes in acoustic signatures and the occurrence of damage within the MLCCs is observed at the population level.

**Publication II** introduces a new method for processing the acoustic data from MLCCs. Filtering techniques are applied to the measured acoustic waveforms to remove noise caused by electromagnetic interference from the measurement setup. Characteristic resonance amplitudes and frequencies are then extracted as feature vectors from the denoised waveforms, and correlation between the features and the types of damage is observed.

A binary support vector machine is then fitted to data from damaged and bent-but-not-damaged MLCCs to demonstrate algorithmic detection of mechanical damage in the components.

In **Publication III**, the data preprocessing pipeline is improved by extracting the phase information from the acoustic waveforms, and new numerical features are extracted from the amplitude and phase responses. The identification of damaged MLCCs is approached as a one-class learning problem, and the classification task is performed using the one-class support vector machine. A new algorithm for optimizing the hyperparameters of the OSVM is presented, and the effectiveness of the algorithm is evaluated on several commonly used benchmark datasets. Lastly, detection of damaged MLCCs is demonstrated using the combination of the OSVM and the proposed optimization algorithm, and the role of the features extracted from the acoustic data is evaluated.



## 2 Research methods

The starting point of this study was to investigate the use of acoustic testing methods for detecting latent mechanical damage in MLCC-type ceramic capacitors. The research started as a spin-off of an ABB quality assurance project called Beyond Burn-in, which was set to investigate cracking problems observed in large MLCCs found in power electronics applications. While the capacitors can contain manufacturing defects, cracks are often caused later on the assembly line, where the circuit board may be subjected to thermal and mechanical stresses. Because existing methods, namely X-ray imaging, were unsuitable for screening large quantities of components at the production line level, the aim of this study was to find a simpler, alternative method that could be applied to assembly line screening.

### 2.1 Acoustic emission testing

Acoustic emission testing has seen a wide use in many fields of engineering for applications like structural health monitoring (SHM) and nondestructive testing (NDT). Because MLCCs are capable of generating acoustic emissions with no other external excitation than AC voltage, it was hypothesized that the acoustic emissions generated by the capacitors could be used in detecting changes in the structural condition of components. Consequently, the research focused on acoustic emission measurements at the early stages of the study.

#### 2.1.1 Acoustic emissions in MLCCs

Acoustic emissions related to class II MLCCs are well-documented in the literature. When subjected to alternating voltage, mechanical vibrations arise within an MLCC body as a result of the piezoelectric properties of the ceramic dielectric material,  $\text{BaTiO}_3$ . Below the Curie point, the atoms of a  $\text{BaTiO}_3$  molecule are arranged in a tetragonal shape, which results in an electric dipole that can be polarized. The  $\text{BaTiO}_3$  molecules form a crystalline structure consisting of grains under a micrometer in size (Lee and Aksay, 2001). The grains are further divided into domains where the grains share a common

spontaneous polarization  $P$ , which relates to the dielectric constant  $\epsilon$  of the medium as (Lee and Aksay, 2001)

$$\epsilon \approx \frac{P}{\epsilon_0 + E}. \quad (2.1)$$

Applying voltage over an MLCC introduces an external electric field within the dielectric, causing the net polarization over the grain domains (Yang, 2005) to reverse, thereby yielding a higher capacitance according to (2.1) (Skelly and Waugh, 2009). This also causes displacement within the  $\text{BaTiO}_3$  molecules, resulting in deformation of the dielectric, a phenomenon known as the inverse piezoelectric effect (Ousten et al., 1998). The piezoelectric behavior of class II MLCCs is a well-known phenomenon, and capacitors with a type X7R dielectric have even been studied for their micro-actuating properties for applications such as scanning probe microscopes (Chen and Feng, 2014). Under AC voltage, the oscillatory deformation of the capacitor body can cause the circuit board under the component to resonate at audible frequencies, producing a buzzing noise (Ahmar and Wiese, 2015; Ko et al., 2014). However, the mechanical resonance frequencies of MLCC bodies are far above the human hearing range, typically within hundreds of kilohertz to over a megahertz (Levikari et al., 2018; Ko et al., 2014).

The amplitude and frequency of the mechanical resonances exhibited by an MLCC are affected by the structural and material properties of the capacitor body. In addition, the resonant characteristics of an MLCC body can be altered as a result of physical damage, such as cracks or delamination. Thus, the acoustic emissions arising from the piezoelectric properties of type II MLCCs can also convey information about the structural condition of the capacitor. This mechanism is also the basic principle behind the acoustic emissions testing method introduced in this dissertation.

## 2.2 Overview of the research methods

The research methods and results presented in this dissertation are based on acoustic emission data empirically collected from MLCCs. As the objective was to develop an NDT method that could be applied on an assembly line, acoustic experiments were conducted on a large sample of MLCCs, comprising both pristine and damaged components of various case sizes and capacitance values.

The acoustic experiments were conducted on capacitors soldered onto custom-built test PCBs. The design and layout of the PCBAs facilitated simultaneous electrical monitoring of 120 MLCCs per PCB assembly, and the PCB itself was designed such that it could be subjected to an industry-standard bending procedure for inflicting damage to the component samples. This design feature facilitated the collection of acoustic data from the same individual component samples before and after subjecting the PCB to mechanical stress.

First, preliminary acoustic experiments were conducted on a small number of intact and

damaged MLCC samples to find a suitable configuration for the measurement setup for data acquisition in a larger scale. During these tests, it was concluded that the acoustic emissions from an MLCC could be obtained by placing a piezoelectric point contact sensor directly on top of the component. A visual inspection of acoustic waveforms also revealed dissimilarities between data from intact and damaged MLCC samples. The developed acoustic characterization process was thus deemed a suitable method for collecting acoustic data from MLCCs.

Next, the study entered the full-scale data acquisition phase, during which acoustic data were collected from hundreds of MLCC samples. The acoustic characterization process was fully performed on several test PCB assemblies. After the characterization, two of the PCBs were subjected to controlled bending, after which they were recharacterized. Finally, the MLCC samples on the bent PCBs were X-ray imaged and cross-sectioned to reveal which of the components samples had actually suffered physical damage from the bending. The results from the X-ray and cross-section analysis were later used as ground-truth labels for the analysis of acoustic data.

With all the data collected, the study moved on to the analysis phase. First, a population-level study was conducted in order to reveal whether or not damaged MLCCs would systematically exhibit acoustic responses dissimilar to pristine ones. The results of the study, also included in **Publication I**, confirmed that mechanical damage alters the acoustic signature of the MLCCs. Next, the relationship between different features of the acoustic waveforms and types of damage were inspected in **Publication II**, and a simple machine-based classification between damaged and undamaged MLCC samples was successfully demonstrated. As a result, machine-learning-based classification was chosen as the primary approach for the rest of the development of the acoustic NDT method.

Based on the results from **Publications I** and **II**, two major challenges concerning the acoustic NDT method were identified: noise in the acoustic data and the accuracy of the ground truth labels assigned to the MLCC samples based on the results from the X-ray and cross-section analyses. The noise in the acoustic data was found out to be electromagnetic interference originating from the measurement setup itself. Many of the signatures in acoustic data related to mechanical faults were of a significantly lower amplitude than the noise component. On the other hand, labeling of the MLCC samples on the bent PCB assemblies proved to be a challenging task, resulting in inaccuracies in the ground truth labels.

To overcome the challenges related to measurement noise, signal preprocessing was a key priority when analyzing the acoustic data. Various filtering techniques were developed and evaluated, with the results reported in **Publication II**. Another task, critical for machine-learning-based classification, was feature engineering, i.e., extracting information from the acoustic data so that the extracted features were relevant for the classification task and robust to measurement noise. After evaluating several feature extraction techniques, a functional feature set was developed and reported in **Publication III**.



However, the challenges related to acquiring labeled samples for training the machine learning classifier remained an open problem. Although the classifier was trained using data from intact and damaged MLCCs in **Publication II**, the process of producing annotated samples of acoustic data from damaged MLCCs was labor-intensive and inaccurate. As a solution, the use of outlier detection methods and one-class machine learning classifiers was inspected. Although the research eventually focused on the use of one-class machine learning models, optimizing the hyperparameters of such models to the specific task of identifying damaged MLCCs proved challenging. After a review of various optimization techniques found in the literature, a new optimization algorithm was eventually developed and tested on publicly available data sets. The optimization algorithm was introduced in **Publication III**, along with the test results on common benchmark data sets.

Finally, the concept of acoustic-emission-based nondestructive testing was demonstrated using a combination of techniques developed during the research project, comprising the acoustic measurement process itself, signal denoising, feature extraction, hyperparameter optimization, and model training. The classification results obtained using the combination of hyperparameter optimization and one-class classification were compared with those obtained using conventional two-class machine learning models, showing performance on a par with the conventional methods.

## 3 Measurements and data preprocessing

### 3.1 Acoustic measurements

The results and analyses presented in **Publications I, II, and III** were all based on the same experimental data, collected during the writing of the author's Master's thesis. The experiments were conducted on soldered MLCCs of four case sizes and capacitance values. **Publication I** presents the first observations on the effects of mechanical damage on MLCCs of different case sizes, whereas **Publications II and III** focus on the capacitors with the largest case size of 2220.

The capacitors inspected in the study were from three different manufacturers and represented four different case sizes between imperial 1206 and 2220, as commonly found in power electronics systems. Developing an NDT method for such physically large MLCCs is particularly relevant, as they have been shown to be significantly more prone to bending-related damage than their smaller counterparts (Keimasi et al., 2008). A total of 360 capacitors were soldered onto three test PCBs, one labeled as type A and the other two labeled as type B (see Tables 3.1 and 3.2), with an identical setup of MLCCs on each PCB type. The design of the test PCBs facilitated subjecting the boards to an industry-standard bending procedure for inflicting stress-related damage to the MLCCs (see Table

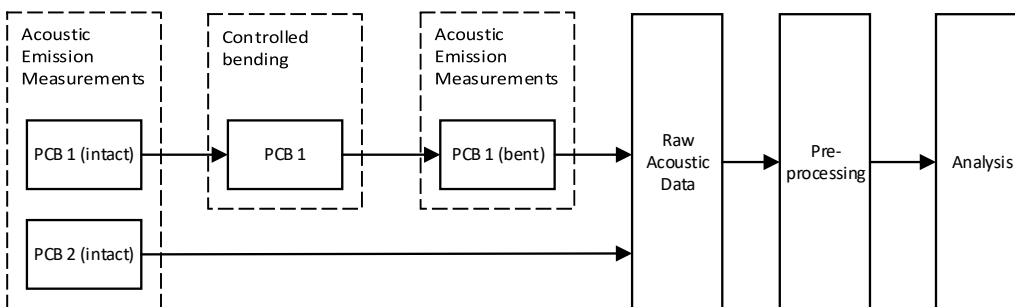


Figure 3.1. Overview of the acoustic measurements. Both PCBs 1 and 2 were test boards of type B, containing MLCCs of larger case sizes than those on the type A PCBs. Capacitors from both PCB types were included in the initial analysis, but the components on type B PCBs were chosen for further study.

3.3 for details). The acoustic measurements were performed twice on selected PCBs, both before and after subjecting the test boards to the bending procedure, after which the acoustic data were preprocessed for further analysis (see Fig. 3.1). By performing the measurements on the same exact components before and after bending, it was ensured that no mechanical differences between batches of capacitors or individual components would bias the results of further analysis.

The component samples on type A PCBs were labeled as C1 through C120, and the samples on type B PCBs were labeled as C121—C240. The capacitors were assembled as columns of ten samples each so that the MLCCs in a given column shared an identical capacitance, case size, voltage rating, manufacturer, orientation and termination type. The set of test capacitors included both MLCC with normal terminations and capacitors with flex terminations, which, according to the manufacturers, are more resilient against bending damage. Because the components do not experience uniform stress during the bending process, the components were assembled in three different orientations ( $0^\circ$ ,  $45^\circ$ , and  $90^\circ$ ) relative to the direction of bending. A summary of the test components is given in Table 3.4. The test PCBs and components were provided by ABB Ltd, and the PCBs were originally assembled for the “Beyond Burn-in” project.

The first acoustic characterization was performed on intact test PCBs at Lappeenranta University of Technology. The PCBs were then carefully packaged and mailed to ABB Schweiz Ltd, Turgi, Switzerland, where mechanical damage was inflicted to the components by subjecting the test PCBs to controlled bending using an industry-standard Zwick/Roell Z010 four-point bending setup. The test circuit boards were subjected to a bending displacement of 18 mm, while continuously monitoring the capacitors for short-circuits. The bending strain was measured using strain gauges attached to the centerline of the board, with strain values ranging from  $5800\mu\text{Str}$  to  $8000\mu\text{Str}$ , with an average strain level of  $6000\mu\text{Str}$ . Both PCBs underwent a single bending procedure, after which the boards were removed and the components were inspected using X-ray for flex cracks using a Phoenix Nanomex machine.

After the bending procedure and X-ray inspection, the PCBs were mailed back to Finland, where the acoustic characterization process was repeated using the same exact measurement setup as during the first characterization run. Preliminary comparisons of acoustic data from before and after the bending procedure were performed at this point by comparing the envelopes of the acoustic responses (discussed in greater detail in Chapter 5). However, based on the acoustic data, more components seemed to be affected by the bending than what the X-ray images suggested. In particular, MLCCs of case size 2220 seemed to exhibit changes that were not explained by the X-ray inspection. This was attributed at least partially to the limitations of X-ray imaging. To gain confirmation of which of the components were actually damaged during the bending process, the 2220-sized MLCCs were cross-sectioned to verify which component samples were damaged.

Although the first analysis in **Publication I** included each MLCC type featured on the test PCBs (see Table 3.4), the further analysis in **Publications II** and **III** focused specif-

Table 3.1. Details about the MLCCs on test PCB type A

MLCC nr	col	Size	Orientation	Type	Producer	C
C1-C10	<i>a</i>	1206	0°	Normal	TDK	4.7 $\mu$ F
C11-C20	<i>b</i>	1206	0°	Flex	Kemet	4.7 $\mu$ F
C21-C30	<i>c</i>	1206	45°	Normal	TDK	4.7 $\mu$ F
C31-C40	<i>d</i>	1206	45°	Flex	Kemet	4.7 $\mu$ F
C41-C50	<i>e</i>	1206	90°	Normal	TDK	4.7 $\mu$ F
C51-C60	<i>f</i>	1206	90°	Flex	Kemet	4.7 $\mu$ F
C61-C70	<i>g</i>	1210	0°	Normal	TDK	10 $\mu$ F
C71-C80	<i>h</i>	1210	0°	Flex	Kemet	10 $\mu$ F
C81-C90	<i>i</i>	1210	45°	Normal	TDK	10 $\mu$ F
C91-C100	<i>j</i>	1210	45°	Flex	Kemet	10 $\mu$ F
C101-C110	<i>k</i>	1210	90°	Normal	TDK	10 $\mu$ F
C111-C120	<i>l</i>	1210	90°	Flex	Kemet	10 $\mu$ F

Table 3.2. Details about the MLCCs on test PCB type B

MLCC nr	col	Size	Orientation	Type	Producer	C
C121-C130	<i>a</i>	1812	0°	Normal	TDK	22 $\mu$ F
C131-C140	<i>b</i>	1210	0°	Flex	AVX	10 $\mu$ F
C141-C150	<i>c</i>	1812	45°	Normal	TDK	22 $\mu$ F
C151-C160	<i>d</i>	1210	45°	Flex	AVX	10 $\mu$ F
C161-C170	<i>e</i>	1812	90°	Normal	TDK	22 $\mu$ F
C171-C180	<i>f</i>	1210	90°	Flex	AVX	10 $\mu$ F
C181-C190	<i>g</i>	2220	0°	Normal	TDK	22 $\mu$ F
C191-C200	<i>h</i>	2220	0°	Flex	Kemet	22 $\mu$ F
C201-C210	<i>i</i>	2220	45°	Normal	TDK	22 $\mu$ F
C211-C220	<i>j</i>	2220	45°	Flex	Kemet	22 $\mu$ F
C221-C230	<i>k</i>	2220	90°	Normal	TDK	22 $\mu$ F
C231-C240	<i>l</i>	2220	90°	Flex	Kemet	22 $\mu$ F

Table 3.3. Test board specifications

Material	FR-4
Dimensions	39.0cm by 30.4cm
Thickness	1.55 mm
Copper layers	2
Coatings	None
Solder	SAC: 96.5Sn-3.0Ag-0.5Cu

Table 3.4. Overview of the MLCCs assembled on the test boards

Size	Type	Producer	Code number	Series	V rating	C
1206	Normal	TDK	C2316X7R1E475K160AC	C-series	24 V	4.7 $\mu$ F
1206	Flex	Kemet	C1206X475K3RACAUTO	FT caps	24 V	4.7 $\mu$ F
1210	Normal	TDK	C3225X7R1E106M250AC	C-series	24 V	10 $\mu$ F
1210	Flex	AVX	12103C106M4Z2A	Flexitem	24 V	10 $\mu$ F
1210	Flex	Kemet	C1210X106M3RACTU	FT caps	24 V	10 $\mu$ F
1812	Normal	TDK	C5432X7R1E226M250KC	C-series	24 V	22 $\mu$ F
2220	Normal	TDK	C5750X7R1E226M250KA	C-series	24 V	22 $\mu$ F
2220	Flex	Kemet	C2220X226K3RACAUTO	FT caps	24 V	22 $\mu$ F

ically on 2220-sized MLCCs. The shift in the focus of the research was due to several reasons, the most prominent one being that smaller case sizes are less likely to get damaged by PCB bending (Keimasi et al., 2008). Similar observations were also made during the acoustic experiments. After subjecting the test PCBs to 6000 $\mu$ Str bending strain, the X-ray analysis revealed cracks in only one out of 60 MLCCs of the 1206 case size. The 1210-sized components were also resilient to bending strain, with the X-ray showing damage in two out of 90 component samples, and the subsequent cross-sectioning revealing six additional damaged samples. On the other hand, the 1812-sized components were damaged in greater numbers, with clearly observable flex cracks present during the X-ray analysis in 20 out of 30 component samples. The cracks also caused notable changes to the acoustic response of the components. While only five out of 60 samples of the 2220 size showed cracks in the X-ray inspection, the subsequent cross-section inspection revealed additional 32 damaged samples.

### 3.2 Acoustic characterization process and instrumentation

The acoustic measurements, which formed the basis of **Publications I, II, and III**, were conducted on MLCC samples soldered onto test PCBs, which were attached to a custom-

Table 3.5. Equipment used for Acoustic Emission measurements

Device	Make and model
Signal generator	Agilent 33250A
Point contact sensor	KRN Services KRNBB-PC
Preamplifier	KRN Services AMP-1BB-J
Oscilloscope	Keysight InfiniiVision MSO-X 4104A

built fixture. The measurements were performed by applying electrical excitation to the component under test, and resulting acoustic waveforms were measured using a piezo-electric point contact sensor. The sensor was housed in a 3D-printed fixture, and additional weights were attached to the sensor in order to provide repeatable sensor placement and downward force. The test setup (see Fig. 3.2) was assembled in an anechoic chamber to minimize the effect of any external sounds or other mechanical vibrations. A circuit diagram of the measurement setup is shown in Fig. 3.3, with the measurement equipment listed in Table 3.5.

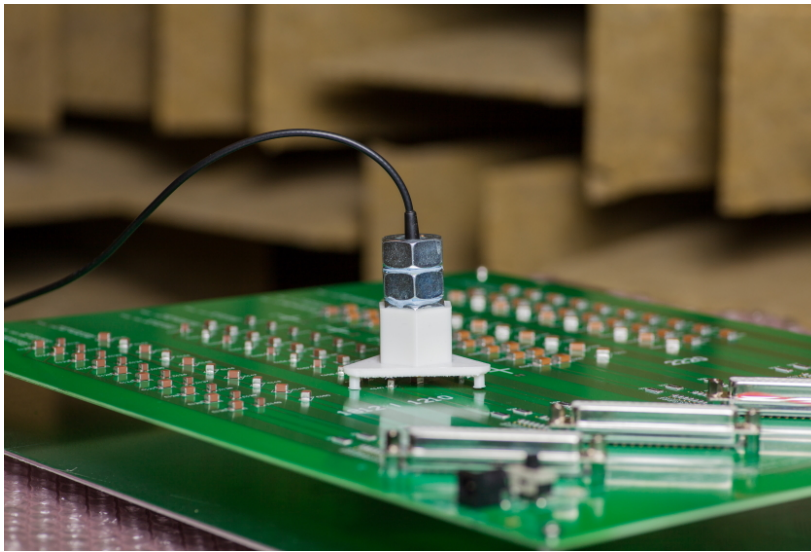


Figure 3.2. Acoustic measurement setup.

The MLCC samples were acoustically characterized one by one. During the acoustic characterization process, the component under test was subjected to a pulsed voltage waveform with a linearly increasing frequency, causing the MLCC body to vibrate mechanically. The vibrations were captured using a point contact sensor, and the resulting waveforms were recorded using an oscilloscope for further analysis.

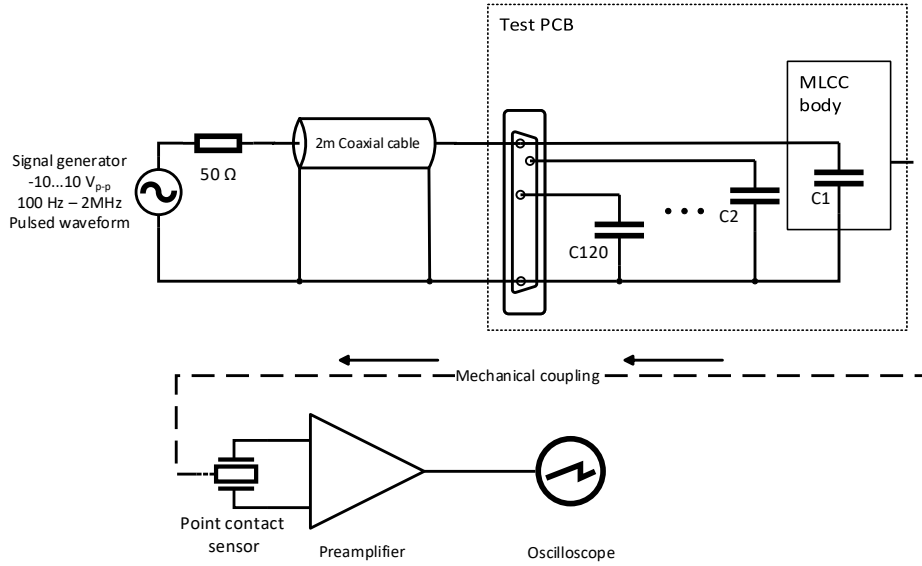


Figure 3.3. Circuit diagram of the measurement setup.

### Signal generator

During the acoustic characterization, each MLCC was subjected to a voltage chirp of 100 ms in duration to excite the component to vibration. An Agilent 33250A signal generator was used as the source of the excitation signal. Each capacitor was subjected to a voltage of -10 V to 10 V using a pulsed waveform with a 80% duty cycle. The asymmetrical waveform was observed to yield a higher acoustic emission amplitude than the sine wave of the same voltage, likely because of the higher signal energy associated with the pulsed waveform. The high duty cycle may also result in a higher amplitude because of the polarization of the dielectric, as discussed in section 1.1. The frequency of the excitation signal was increased linearly from 100 Hz to 2 MHz to cover the usable frequency range of the point contact sensor, maximizing the information about the acoustic properties of the component. The duration of the chirp was set to 100 ms, as chirps of longer durations would have required reducing the sampling rate of the oscilloscope because of memory limitations. On the other hand, chirps shorter than 100 ms were observed to result in a waveform with wider, less defined resonance peaks.

### Point contact sensor

The resonance frequencies of the ceramic body of an MLCC range from hundreds of kilohertz to over a megahertz (Ko et al., 2014), depending on the dimensions of the ceramic body. In order to measure the acoustic behavior of the component and capture the resonant frequencies, a vibration sensor with a wide frequency range was required. A KRN

Services KRNBB-PC Broadband point-contact sensor was chosen for the task, as the sensor has a sensitivity of  $15 \text{ mV/nm} \pm 4 \text{ dB}$  over a frequency range of 20 kHz–1 MHz, with a maximum frequency of 2.5 MHz (KRN Services, 2015). The outer body of the sensor was equipped with M14 threads, to which four hex nuts were attached to provide additional weight when placing the sensor on a capacitor. The nickel-coated tip of the sensor was covered with a piece of Kapton tape to prevent the sensor from short-circuiting the exposed terminations of the capacitor.

### Preamplifier

The point contact sensor was connected to a KRN Services AMP-1BB-J single channel broadband preamplifier with a coaxial cable. The amplifier has a -3 dB bandwidth over a frequency range of 18.2 kHz–2 MHz, with a gain of 28.1 dB at 300 kHz (KRN Services, 2014).

### Oscilloscope

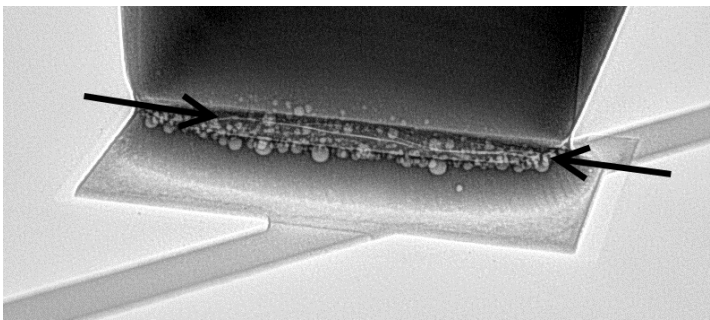
A Keysight InfiniiVision MSO-X 4104A oscilloscope was chosen for recording the raw waveforms from the preamplifier, because the oscilloscope was capable of capturing the acoustic waveform data at a sampling rate of 20 MHz over a duration of 100 ms, enough to cover the acoustic response of the component under test in a sampling rate ten times higher than the highest excitation frequency. The preamplifier was connected to one of the inputs of the oscilloscope by using a coaxial cable.

## 3.3 MLCC sample inspection and labeling

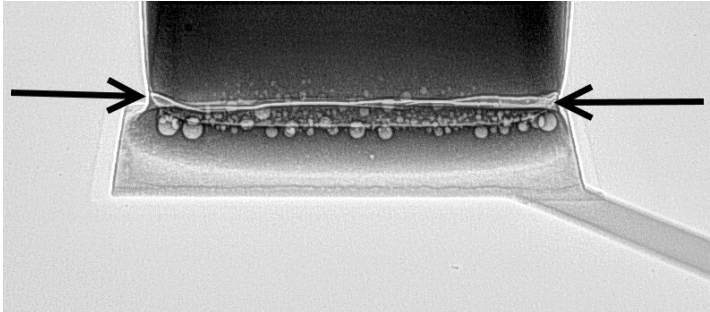
In order to verify which MLCC samples on the bent PCBs were damaged during the bending process, all the samples on the bent PCBs were X-ray inspected using a Phoenix Nanomex machine. The 2D X-ray images were inspected visually for flex cracks, and each component sample was assigned a label according to whether any cracks could be observed. Cracks observed during the inspection were typically located near the bottom edges of the ceramic body, close to the end terminations where the stress caused by PCB bending was highest. Some of the samples contained cracks only at one corner, or spanning partially alongside the edge of the ceramic body (see Fig. 3.4a), whereas some other samples contained cracks spanning across the edge of the component (see Fig. 3.4b).

With the MLCC samples labeled using the X-ray inspection, the acoustic waveforms were initially analyzed by visually looking for differences between the waveforms of samples labeled as damaged and undamaged. It was observed that the acoustic data from the bent





(a) Flex crack extending partially across the end termination of a capacitor



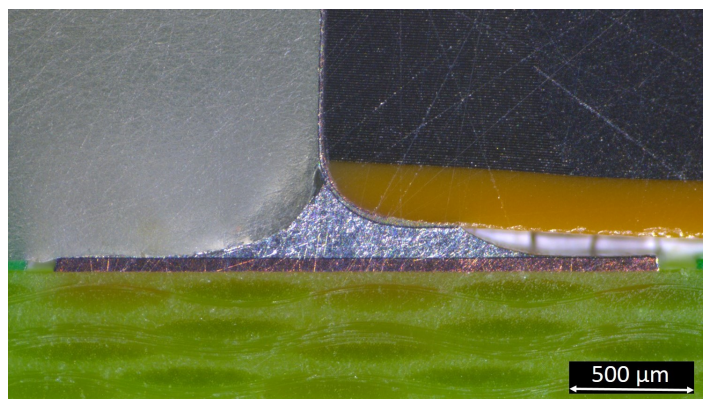
(b) Flex crack extending fully across the end termination of a capacitor

Figure 3.4. X-ray images of two MLCC samples with cracks of different severity. The endpoints of each crack are indicated by black arrows.

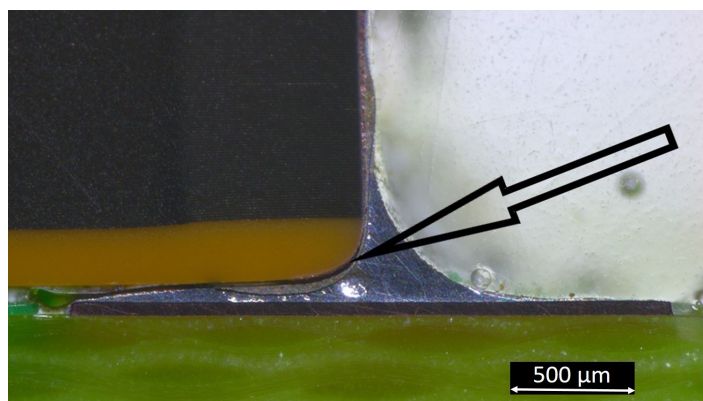
MLCCs suggested a presence of a higher number of damaged components than what could be observed in the X-ray images, especially for 2220-sized MLCCs. This was suspected to be due to the limitations of the X-ray imaging method, because in order to reveal cracks within the dielectric material, the imaging had to be performed at the angle of the crack. Thus, it was possible that some of the cracks were missed because of the wrong imaging angle. It was also acknowledged that delamination within an MLCC could not typically be observed in the X-ray inspection. To confirm the inspection results, the PCBs were carefully packed and sent back to Switzerland, where each of the 2220-sized MLCC samples was cross-sectioned.

The cross-sectioning was performed by cutting the MLCCs off of the PCB and casting the components in clear two-phase epoxy. The samples were then ground to a desired depth using a Struers Rotopol-11, after which the sample surfaces were polished for optical microscopy. Next, the samples were imaged using a Leica M205C optical microscope to reveal cracks or delaminations within the components. As with the X-ray images, the cross-section images were each inspected by eye, and the component samples were assigned a label according to whether the sample was undamaged or it contained a crack, delamination, or both.

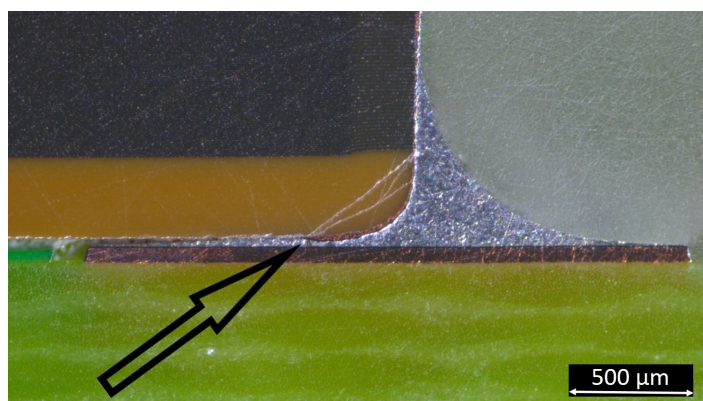
While cross-sectioning can be used for determining different types of mechanical damage in the ceramic body of an MLCC, it only provides information at the specific depth to which the sample has been ground. Moreover, recognizing delaminations from the cross-section images proved to be a challenging task, because small cracks (see Fig. 3.5c) in cross-section images could be mistaken for scratches in the surface of the sample, and vice versa. In some cases, the material interfaces within the sample (see Fig. 3.5a) could also be mistaken for delamination (see Fig. 3.5b). The gaps resulting from the bending would also at least partially close up as the bending stress was relieved, making the faults harder to identify. Therefore, although being an accurate method, the cross-sectioning is not a definite method for identifying damaged MLCCs, and the labels assigned to the component samples were considered not to be fully reliable. The MLCC samples on the PCBs that did not undergo the bending procedure were directly labeled as undamaged without further inspection, because the packaging and handling of the boards was performed carefully in order not to inflict damage onto the components.



(a) MLCC sample with no cracks or delamination visible



(b) MLCC sample showing delamination under the right-hand-side termination



(c) MLCC sample showing cracks in the passive area near the right-hand-side termination

Figure 3.5. Cross-section image examples from three different MLCCs. The MLCCs were all of the 2220 case size and had undergone the bending procedure. The damaged locations are indicated by arrows.

### 3.4 Signal preprocessing

Acoustic data from MLCCs were preliminarily analyzed by visually inspecting the waveforms from selected MLCC samples. When comparing the raw waveforms from known-pristine samples with those from samples with notable cracks visible in the X-ray, it was observed that the cracked samples exhibited more resonance peaks and increased resonance amplitudes compared with the undamaged ones, as shown in Fig. 3.6. Each capacitor case size also exhibited a fundamental resonance at a certain frequency, the amplitude of which was observed to be dependent on the case size of the component. Details about the observed fundamental frequencies are shown in Table 3.6.

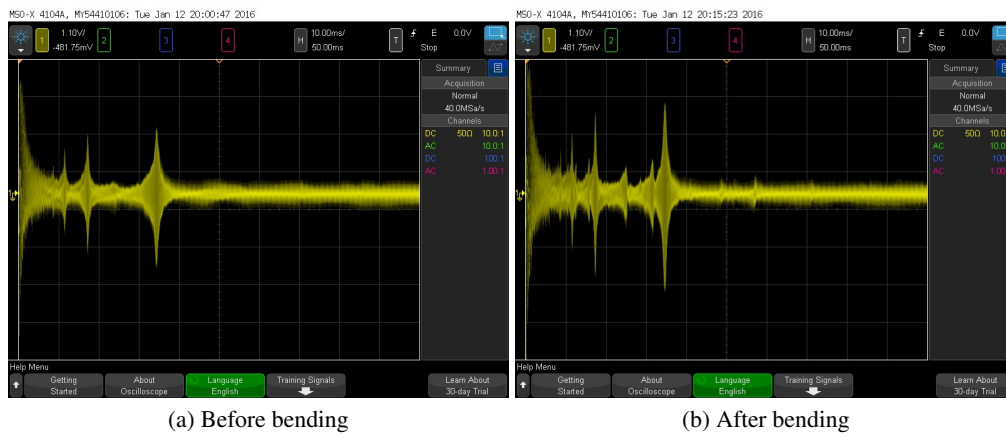


Figure 3.6. Raw acoustic data from a 1812-sized MLCC before and after inflicting physical damage to the component. An increase in the number of resonance peaks can be observed after damaging the body of the component.

The raw acoustic emission waveforms contained significant amounts of noise. While the acoustic resonances of the 1812-sized samples (such as in Fig. 3.6) were clearly observable from raw waveforms, the resonance amplitude of the larger 2220-sized MLCCs was significantly lower, comparable with the amplitude of the noise. 2220-sized components were also the primary focus of the study because of their vulnerability to bending damage. Therefore, to perform further analysis on the experimental data, developing denoising methods for the acoustic data without losing characteristics related to mechanical damage was critical.

Raw acoustic signals were investigated using the spectrograms in **Publication I**, which reveal that the majority of resonance peaks seen in the raw waveforms are actually from the same resonance mode (see Fig. 3.7). As the component samples were subjected to a frequency-swept excitation signal, the resonances were induced multiple times by the harmonic content of the pulsed waveform. These resonances were considered redundant for further analysis and needed to be removed, because they could obscure actual resonances

Table 3.6. Observed fundamental resonance modes, as measured from intact MLCCs

Case size	Amplitude (mean $\pm$ STD) (mV)	Frequency (mean $\pm$ STD) (kHz)
1206	$77 \pm 22$	$908 \pm 251$
1210	$142 \pm 39$	$706 \pm 43$
1812	$106 \pm 20$	$700 \pm 3.4$
2220	$21 \pm 6$	$595 \pm 360$

occurring at the same time during the electrical excitation.

In addition to the resonances caused by the harmonics, a significant amount of electromagnetic interference was present in the acoustic signals. Some of the EMI noise was unavoidable because of the design of the test PCB: the traces from the connectors to the MLCC samples were dozens of centimeters in length, and each sample was connected via two traces instead of a common ground plane. This resulted in loops up to  $\sim 100\text{cm}^2$ , which were a likely origin of the EMI noise, because the MLCC samples were excited with voltage signals up to 2MHz. Because the frequency of the excitation signal also matched the observed frequency of the acoustic response of the component, the EMI component could not be removed just by applying a lowpass filter to the acoustic signals.

In addition to noise removal, the size of the acoustic data had to be reduced because of the memory requirements, because each acoustic waveform contained  $2 \cdot 10^6$  datapoints. With the harmonics and EMI-related noise removed from the signals, the frequency content of the signals was considered expendable. Because each component sample was electrically excited throughout the same frequency range, and the mechanical vibration frequency of the MLCC matched that of the excitation signal, the instantaneous frequency of the mechanical vibration could be directly calculated knowing the time since the excitation signal started. Thus, the memory footprint of the data was reduced by calculating an amplitude envelope for each acoustic signal, preserving the overall shape of the signal while reducing the number of datapoints by a factor of 200. In addition to amplitude information, instantaneous phase was also calculated for each acoustic signal, and downsampled alike.

To clean EMI-related noise from the raw acoustic data, the acoustic signal of each MLCC was first filtered using an automated interval-dependent wavelet denoising algorithm, because this was observed to remove some of the noise within the signals. A second-order biorthogonal wavelet with eight vanishing moments was chosen for decomposing the signal, as it was observed to result in accurate approximation of the original signal and a smooth reconstructed waveform. The parameters for the wavelet denoising were experimentally selected by inspecting the raw acoustic waveforms. After wavelet denoising, the acoustic signals were highpass filtered in order to remove the high-amplitude burst at the beginning of the excitation chirp (see Figs. 3.7a and 3.7b). A fourth-order Butterworth

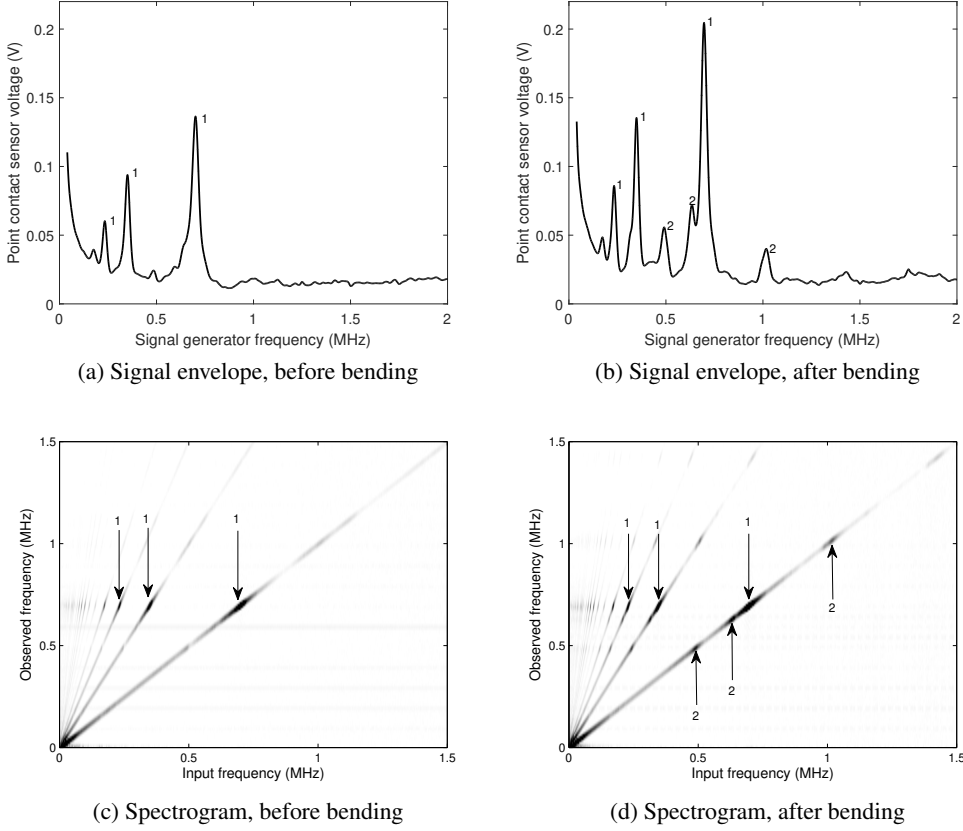


Figure 3.7. Signal envelopes and the corresponding spectrograms for a 1812-sized capacitor before and after inflicting damage to the component. The spectrograms show that the three highest peaks (1) observed in the envelope are the harmonics of a single resonance mode. Physical damage (flex cracks) in the component causes an increase in the amplitude of the resonance peak (1) and the emergence of three new resonance peaks (2).

filter with a cutoff frequency of 150 kHz was used as the highpass filter. After highpass filtering the signals, the harmonics were removed from the acoustic data by overlap-add-decomposition combined with lowpass filtering. First, each signal was divided into 64 blocks with a 50% overlap. The signal content of each block was windowed using the von Hann window function to remove abrupt transients at the endpoint of the block. The content of each block was then lowpass filtered using a second-order Butterworth filter, with a cutoff frequency 1.3 times the excitation signal frequency at the endpoint of the block.

After denoising the data and removing harmonics, the amplitude envelope  $e(t)$  was cal-

culated for each MLCC using the real part of the Hilbert transformation  $Re(\mathcal{H}(\cdot))$  as

$$e(t) = \text{DS} \left\{ \text{lpf} \left[ \sqrt{(u(t))^2 + Re\{\mathcal{H}(u(t))\}^2} \right] \right\}, \quad (3.1)$$

i.e., the resulting Hilbert-transformed signal was lowpass filtered (lpf) using a fourth-order Butterworth lowpass filter with a cutoff frequency of 75 kHz to remove ringing, and the resulting signal was then downsampled (DS) to 10 000 datapoints per signal for dimensionality reduction and a smaller memory footprint. The resulting amplitude envelope, with the harmonics removed, can be viewed as an estimate of the mechanical amplitude response of the capacitor body. The envelope signals (3.1) were used as the basis of analysis in **Publication II**, where the resonance peaks observed in the signal envelopes were correlated with the types of damage found in the MLCC samples. In addition to the amplitude response estimates, the phase response estimates were constructed from each measured signal, because physical damage was expected to change also the phase response of the ceramic body. Because the excitation signals were not measured during the acoustic measurements, the phase of the acoustic response relative to the excitation could not be calculated directly. Instead, the phase response was estimated by comparing the acoustic signal with an idealized representation  $c(t)$  of the excitation chirp signal

$$c(t) = \sin \left( 2\pi \left( f_0 t + \frac{k}{2} t^2 \right) \right), \quad (3.2)$$

where  $k = (2 \cdot 10^6 \text{ s}^{-1} - 100 \text{ s}^{-1})/0.1 \text{ s}$  is the chirp rate of the excitation signal, and  $f_0 = 100 \text{ s}^{-1}$  is the starting frequency of the chirp. The mechanical phase response of the capacitor body was then calculated using the idealized chirp signal  $c(t)$  as

$$\phi(t) = \text{DS} \left\{ \text{lpf} \left[ \angle \mathcal{H} \left( \frac{u(t)}{c(t)} \right) \right] \right\}, \quad (3.3)$$

where lpf denotes a fourth-order Butterworth filter with a cutoff frequency of 1 kHz, and DS denotes downsampling to 10 000 data points, using the same downsampling rate as in (3.1).

With the amplitude (3.1) and phase (3.3) data calculated, an acoustic data set was constructed by extracting a set of numerical features from the amplitude and phase response of each MLCC sample on two test PCBs. The first PCB was acoustically characterized only once without bending, whereas the other one was characterized both before and after bending the board. The feature extraction process is discussed in depth in Chapter 4. The data set was then used as a basis for constructing machine learning models in **Publications II** and **III**, which were used for identifying damaged MLCCs based on acoustic data. The machine learning methods are discussed in greater detail in Chapter 5.

## 4 Feature extraction

After conducting the acoustic measurements and preprocessing the measurement data, the aim was to develop a machine-learning-based classification technique for discriminating between damaged and nondamaged MLCC samples based on acoustic data. In order to do so, the acoustic data had to be processed so that it could be used as an input for a machine learning classifier.

A typical machine learning classifier works by mapping a number of predictor variables, or features, into an output value, which represents the quantity or quality of interest (Mehta et al., 2019). For the case of detecting damage in MLCCs, the output value was chosen to represent the predicted state of the component, with the integer 0 meaning “no damage” and 1 meaning “damage found.” The features, on the other hand, are variables that should carry some relevant information about the structural condition of the MLCC sample.

A naïve way of extracting features from the acoustic data would have been to use each data point in a signal envelope as a feature. However, this approach was abandoned because only the resonance frequencies within the envelope were considered relevant, and thus, the majority of the data points would just represent noise. Moreover, each MLCC sample would have been represented by a feature vector with a dimensionality very high ( $\mathbb{R}^{10^4}$ ) compared with the total number of component samples (approximately 100). This leads to a situation that is challenging from the machine learning perspective, also known as *the curse of dimensionality* (Russell and Norvig, 2009). Thus, it is often preferred to limit the number of feature variables (Dougherty, 2013).

Several feature extraction approaches for acoustic envelope data were evaluated. For instance, the acoustic envelopes were approached as time series data, and long short-term memory recurrent neural networks (LSTM) were trained to classify an acoustic envelope as “damaged” or “intact.” Another experiment involved the use of a one-dimensional convolutional neural network (CNN) for the same task. However, neither of the methods yielded significantly better results than 50/50 guessing, probably because of the limited number of training instances versus the number of data points.

During the preliminary analysis of the acoustic data, it was also observed that there were systematic differences in the EMI noise levels between acoustic measurements performed



on different occasions. While the exact reason for this remained unknown, slight changes to the geometry of the measurement setup and electrical machinery in a laboratory nearby were identified as the most likely causes. Although minor, these differences were carried over to the acoustic envelopes, with the potential of biasing classification results based on raw envelope data. For the same reason, deep learning techniques, such as CNNs and autoencoders, were ruled out as the feature extraction approach, since such models would be likely to learn to model such systematic differences between sets of measurements.

Given the relatively small sample size of MLCCs and the possible biasing effect from external factors such as EMI, a more simplistic approach was taken by employing manual feature extraction. By constructing and selecting the feature variables manually, the effect of external biasing factors could be eliminated, while simultaneously allowing for evaluating the effectiveness of various physical quantities, such as amplitude and phase, for the classification task.

## 4.1 Amplitude and frequency

Based on the initial observations of the acoustic measurement data, it was assumed that any mechanical damage within an MLCC body would manifest itself as changes in the amplitude (resonances) or phase characteristics within acoustic data. Thus, a few hand-selected feature variables representing these characteristics of an acoustic signal could be used in the classification task. This approach was successfully demonstrated in **Publication II**, where a simple machine learning classifier was trained to distinguish undamaged MLCCs from damaged ones on a bent PCB. Each MLCC sample was represented by two feature variables,  $A_1$  and  $A_2$ , which were defined as the amplitude of the highest resonance peaks above and below 700 kHz. These peaks were chosen because the 2220-sized MLCCs, which the experiments were performed on, exhibited strong resonance at approximately 500 kHz. Moreover, damaged component samples were observed to exhibit new resonances in frequencies typically above 1 MHz.

For **Publication III**, the feature set was expanded from the two resonance amplitudes. The objective was to construct a set of features that would provide useful information about the structural condition of the component, while being robust to external influences, such as EMI and variations within the contact between the piezoelectric sensor and the capacitor being measured. As the maximum resonance peak amplitudes (denoted  $A_1$  and  $A_2$ ) below and above 700 kHz were proven to be useful features in **Publication II**, they were also used as part of the new feature set. In addition to the amplitude values, the resonance frequencies of these peaks, denoted as  $f_1$  and  $f_2$ , were introduced as feature variables, as another study by Johnson et al. (2017) had associated shifts in the resonant frequencies of a capacitor body with mechanical damage. Moreover, **Publications I** and **II** showed that cracks and delaminations often result in the emergence of new resonance peaks at various different frequencies. To take such peaks into account, the median am-

plitude  $m_A$  and frequency  $m_f$  of ten of the highest resonance peaks within the envelope were used as feature variables.

## 4.2 Phase

In addition to the resonance-based features, the mechanical phase response (3.3) of the capacitors was considered. Two features were drawn from the phase estimate: the total phase change  $\Delta\phi$  over the duration  $t$  of the signal sweep

$$\Delta\phi = \int_t \left| \frac{d\phi(t)}{dt} \right| dt \quad (4.1)$$

and the mean Group Delay Ripple value (*GDR*). The group delay ripple values were calculated from the phase response estimates by spanning a line between each adjacent minimum and maximum within the phase curve and calculating the maximum distance between the phase and the line. The final value for the *GDR* variable was calculated as the mean of the group delay ripple values associated with ten of the highest maxima within the phase graph, as described in Algorithm 1. A visual depiction of the filtering and feature extraction process is shown in Fig. 4.1, and a summary of the extracted feature variables is given in Table 4.1.

## 4.3 Feature exploration

To verify that the chosen feature variables actually conveyed information about the structural condition of the MLCC samples, the features were assessed by examining the marginal distribution of each feature for different groups of MLCC samples. Because the feature variables were selected heuristically based on what effects were thought to manifest in the acoustic responses of the capacitors after suffering mechanical damage, the distributions for these features were expected to be dissimilar. On the other hand, the distribution of the features extracted from two sets of pristine MLCCs acoustically characterized on different occasions should be similar, as the physical parameters of the components should follow the same distribution. Fig. 4.2 shows that in general, the distributions for samples labeled as “damaged” differ from those of the undamaged ones, although dissimilarities between the intact PCBs 1 and 2 can also be seen. Some of these differences, such as those observable in the amplitude-related features, probably originate from the acoustic measurement event, whereas differences in the frequency-related distributions are presumably related to the feature extraction process.

Another view into the effectiveness of the extracted feature variables was taken by performing a permutation importance analysis on the acoustic data set using a binary classification algorithm known as the random forest (Ho, 1995). The method essentially trains

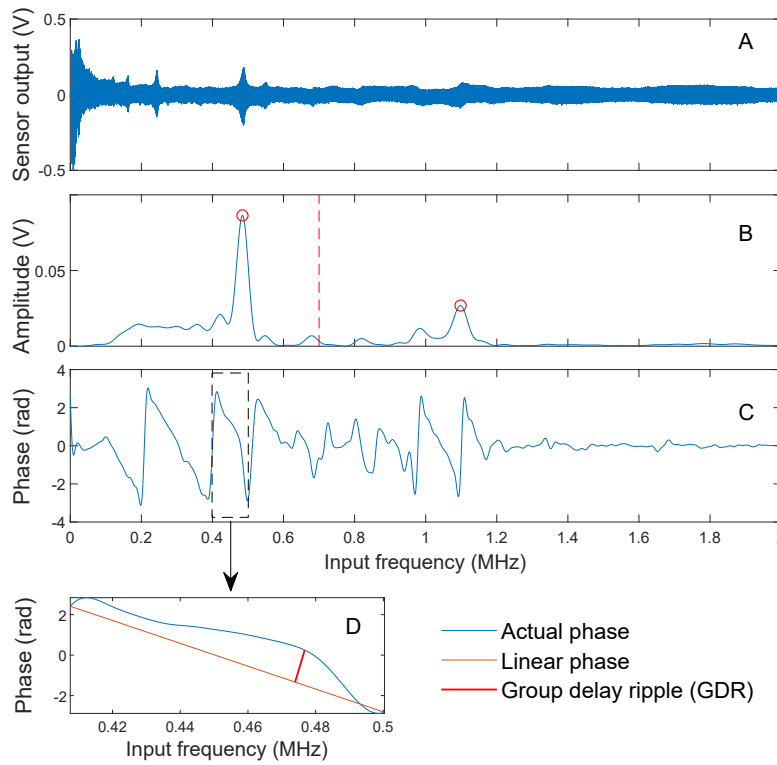


Figure 4.1. Preprocessing steps for acoustic data, based on which the feature variables in Table 4.1 were extracted. An example of raw acoustic data is shown in A. The raw signal was filtered, and the amplitude envelope of the signal was calculated (B), which was used for extracting the amplitude and phase of the resonance peaks, indicated by red circles. The raw signal was also used for calculating the phase response (C), from which the total phase shift was measured. Finally, the phase response was analyzed for the group delay ripple (D).

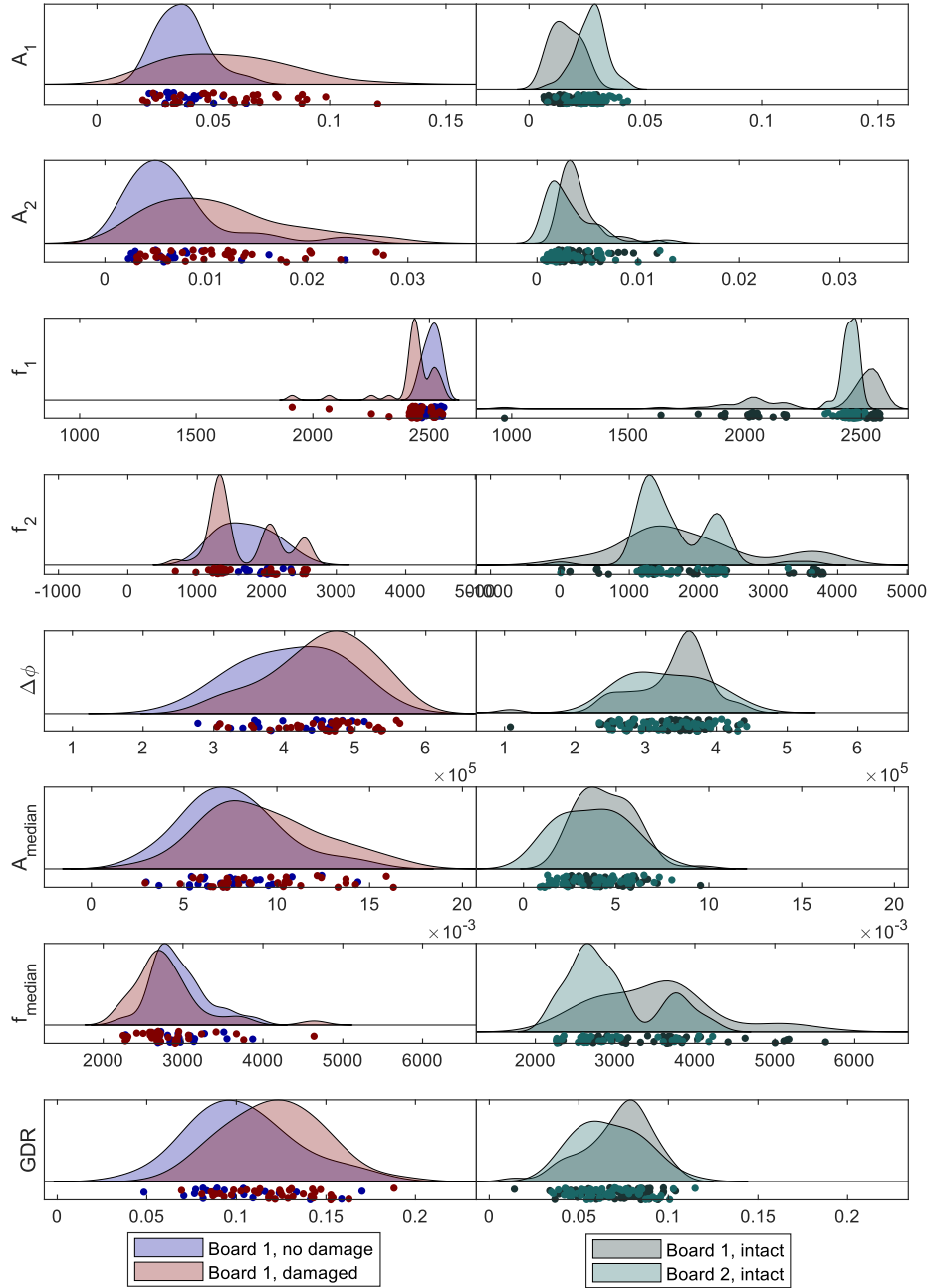


Figure 4.2. Raincloud plots showing the marginal distribution of each feature in the dataset. The distributions in the left column contain the measurements from both damaged and undamaged capacitors on the bent test board 1. The right column contains the measurements from test board 1 before bending, and the measurements from the nonbent reference board 2. Good features should show a difference in the distribution between damaged and undamaged capacitors, whereas capacitors on two intact boards should show no systematic difference.

**Algorithm 1** Group delay ripple

---

**Require:** Phase vector  $\phi \in \mathbf{R}^{10^4}$   
*#Calculate the first derivative of  $\phi$*   
Set  $d\phi \leftarrow \frac{d\phi(t)}{dt}$   
*#Omit the discontinuities within the phase graph where the change in  $\phi$  exceeds  $2\pi$*   
Set  $\phi_- \leftarrow \phi (d\phi < 0)$   
*#Locate 10 of the highest maxima in  $\phi_-$*   
**for**  $i = 1$  to 10 **do**  
  Set  $\text{idx}_i \leftarrow$  index of maximum  $i$  in  $\phi_-$   
**end for**  
*#Calculate the group delay ripple value for each descending block of  $\phi$*   
**for**  $i = 1$  to 9 **do**  
  *#Consider a section of  $\phi$  between two adjacent maxima*  
  Set  $\phi_{\text{block}} \leftarrow \phi_- (\text{idx}_i : \text{idx}_{i+1} - 1)$   
  *#Create a linearly-spaced line segment  $y$  between the endpoints of  $\phi_{\text{block}}$*   
  Set  $y \leftarrow \text{linspace}(\phi_{\text{block}}(1), \phi_{\text{block}}(\text{end}))$   
  *#Calculate GDR value for the current block*  
  Set  $\text{GDR}_i \leftarrow \max |\phi_{\text{block}} - y|$   
**end for**  
Set  $\text{GDR} \leftarrow \frac{1}{9} \sum_{i=1}^9 \text{GDR}_i$   
**return**  $\text{GDR}$

---

the model and evaluates the baseline accuracy on a set of test data. After this, the test data are corrupted one feature at a time by randomly permuting the data corresponding to the feature and reevaluating the model with the one column of data shuffled. The decrease in the classification performance with respect to the baseline value can be interpreted as the relative importance of the permuted feature (Breiman, 2001). The random forest algorithm is discussed in greater detail in Chapter 5. The results of the permutation importance analysis in Fig. 4.3 show that features related to phase and amplitude dominate over those related to frequency. The importance of median frequency is negative, meaning that randomly permuting this feature resulted in a slightly better classification performance.

In order to avoid false alarms on intact capacitors, the features extracted should be invariant with respect to any variations between different PCB assemblies and measurement occasions. To this end, the distribution of the eight-dimensional feature vectors was visualized using the t-SNE, a nonlinear dimensionality reduction algorithm (van der Maaten and Hinton, 2008). Fig. 4.4a shows that while the subset of damaged MLCC samples is clearly separate from the intact samples, the data from intact test PCBs 1 and 2 are homogeneously distributed, i.e., there are no clear differences between the two sets of measurements from different PCB assemblies.

Finally, the extracted features were inspected for bias towards a particular termination type. Because half of the 2220-sized MLCC samples had flexible terminations, their res-

Table 4.1. Features extracted from the acoustic responses

$A_1$	Amplitude of the highest peak below 700 kHz, typically found at approx. 500 kHz
$A_2$	Amplitude of the highest peak above 700 kHz
$f_1$	Frequency of $A_1$
$f_2$	Frequency of $A_2$
$\Delta\phi$	Total phase shift calculated according to (4.1)
$m_A$	Median amplitude of all resonance peaks in the acoustic spectrum
$m_f$	Median frequency of all resonance peaks in the acoustic spectrum
$GDR$	Mean group delay ripple. For each descending slope in the instantaneous phase curve, group delay ripple was calculated as the maximum deviation from the corresponding linear slope (see Fig. 4.1, bottom graph). The feature $GDR$ was composed as the mean of all calculated group delay ripple values.

onance characteristics could differ from those with nonflexible terminations. However, the t-SNE visualization of the eight-dimensional data in Fig. 4.4b revealed no clusters with bias toward a particular termination type. Thus, even though the termination may affect the acoustic response of the component, the feature extraction process appears invariant to the termination type.

## 4.4 Acoustic data set

In order to evaluate the performance of different machine learning classifiers on the acoustic data, an acoustic data set was composed by extracting the features in Table 4.1 from 180 acoustic characterization signals. Because the study focused on 2220-sized MLCCs, capacitors of no other case sizes were included. The data set was composed of MLCC samples from two different test boards (denoted PCB 1 and 2). The acoustic data from PCB 1 both before and after bending the PCB were included to facilitate analysis on the same exact components with and without mechanical damage. Measurements from another, intact board (PCB 2) were included to provide more data for training the classification algorithms. Within the data set, the acoustic response of each MLCC was represented as a vector

$$x_i = (A_1, A_2, f_1, f_2, \Delta\phi, m_A, m_f, GDR), \quad (4.2)$$

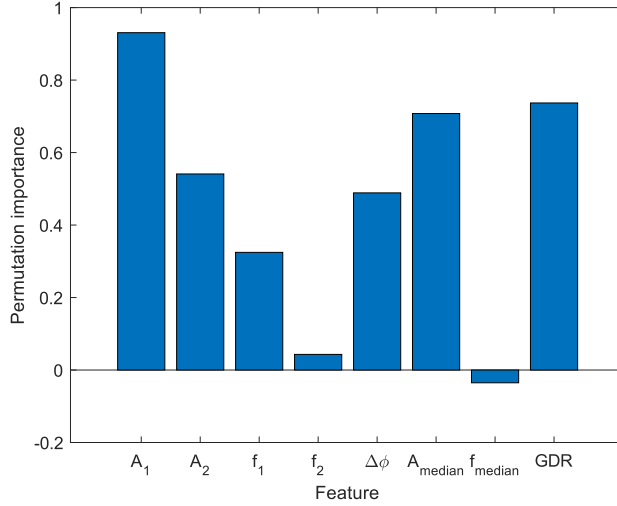


Figure 4.3. Permutation importance of the features extracted from the MLCC acoustic responses. The importance of each feature was calculated by training a classifier on the feature set, then randomly permuting the feature and comparing the classification accuracy with the nonpermuted data. A Random Forest classifier with 1000 trees was used for the importance estimation.

and the data set  $X$  consists of pairs of the feature vector  $x_i$  and the class label  $y_i$

$$X = \{(x_i, y_i) | x_i \in \mathbb{R}^8, y_i \in \{0, 1\}\}, \quad (4.3)$$

where  $i = 1 \dots 180$ ,  $y = 0$  denotes nondamaged and  $y = 1$  damaged MLCC. While the components on the intact PCBs 1 and 2 were assumed to be pristine, the labels for the components on PCB 1 after bending could not be guaranteed to be fully accurate, because the labeling was performed by visually inspecting the X-ray and cross-section images as described in section 3.3. A summary of the data set is given in Table 4.2, and an overview of the workflow of constructing the data set is shown in Fig. 4.5. The machine learning classifiers applied to the data set are discussed in Chapter 5.

Table 4.2. Summary of the MLCC acoustic data set

	Total samples	No damage ( $y=0$ )	Damage ( $y=1$ )
PCB 1 (before bending)	60	60	0
PCB 1 (after bending)	60	23	37
PCB 2 (no bending)	60	60	0
Total	180	143	37

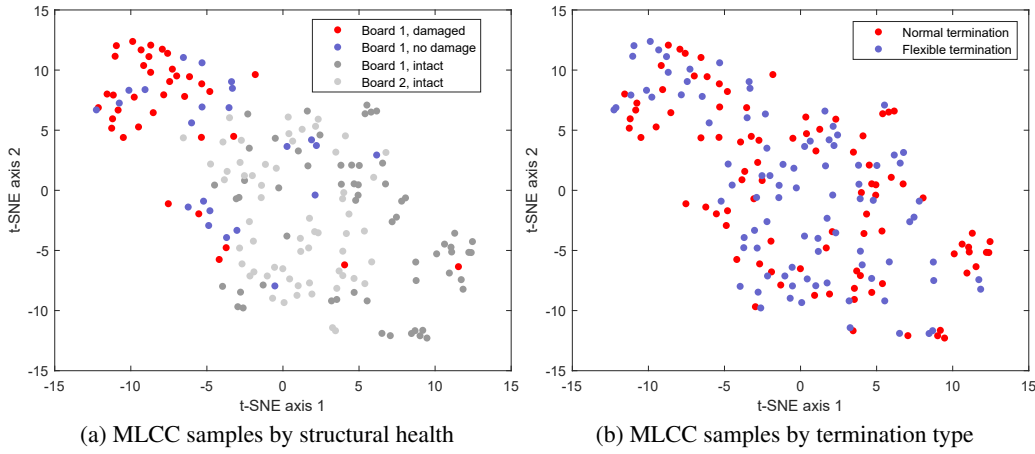


Figure 4.4. t-SNE visualization of the eight-dimensional acoustic data (4.2) in two dimensions. In (a), the red and blue marks correspond to measurements from a bent PCB, whereas the marks in gray indicate measurements from intact PCBs. Damaged MLCC samples clearly constitute a cluster, which is separate from the other data points. In (b), the termination type of the aforementioned data points is shown. Neither of the termination types forms a distinct cluster.



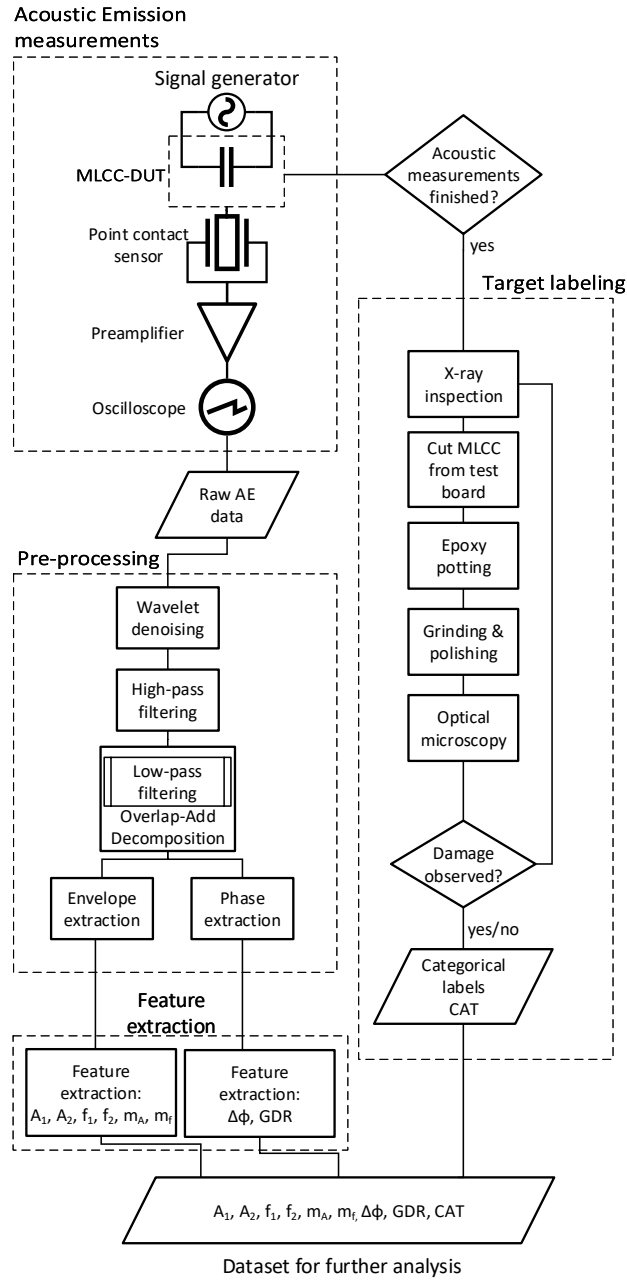


Figure 4.5. Flowchart of the procedure for composing the acoustic data set (from top to bottom). The data set was composed by processing the raw acoustic data and inspecting the cross-sectional and X-ray images of a total of 180 MLCC samples from two test boards. The data set included 60 intact capacitors from PCBs 1 and 2 each and 60 capacitors from PCB 1 after a controlled bending procedure. The extracted features and categorical labels were used as input and output variables for the OSVM model.

## 5 Analysis and classification methods

With the acoustic measurements completed, the research focused on developing algorithmic methods for discriminating between intact and damaged component samples. First, a population-level study was conducted in order to verify that MLCC acoustic responses between bent and intact PCBs were actually dissimilar. To facilitate the study, a metric for comparing the dissimilarity of multiple MLCC acoustic responses was developed. After obtaining positive results from the study, the focus of the research shifted to developing a machine-learning based classifier that could identify damaged MLCC samples based on acoustic data. Finally, one-class learning methods were developed to facilitate an NDT method that could be scaled to a production line environment.

### 5.1 Distance-based comparison of acoustic signals

In **Publication I**, a preliminary study was conducted on acoustic data from bent and intact MLCCs at a population level, with the aim of confirming whether or not the two showed dissimilar acoustic responses. At the time of performing the analyses for the study, the MLCC samples had not been cross-sectioned yet. In the absence of ground truth labels on which ones of the component samples were damaged, the study was performed at a population level by comparing the acoustic responses from the test PCBs before and after subjecting the circuit boards to the bending procedure. The acoustic response of each of the MLCCs was compared with a set of measurements from known-intact capacitors with all the parameters, such as case size and manufacturer, equal to the component under test. By comparing a single acoustic response with a set of several responses, the impact of factors such as measurement noise, sensor-MLCC-contact, and mechanical variations between components could be mitigated. To facilitate such a comparison, a metric named  $L_{GLS}$  was introduced.

In the  $L_{GLS}$  metric, the acoustic response envelope  $e$  of a single capacitor was compared with a reference envelope  $e_{\text{ref}}$ . The reference envelope was calculated as the pointwise mean of intact MLCCs that shared the same electrical and mechanical parameters as the

capacitor from which the envelope  $e$  was extracted:

$$e_{ref} = \frac{\sum_{n=1}^{10} e_n}{10} \quad (5.1)$$

As the component samples were arranged on the test PCBs in columns according to their parameters, the set of reference capacitors comprised all ten components on a same column ( $a-l$ , referring to Tables 3.1 and 3.2) as the component under test. However, being a first observations study, the calculations were performed on envelopes calculated from raw acoustic data, without denoising or removing the harmonic resonances from the data. Thus, the acoustic data contained EMI noise, which resulted in a DC offset in the envelopes. Furthermore, the amplitude of the noise was observed to be dependent on several factors, such as the location of the component on the PCB and the date of the measurement event itself, as the measurement took place on different occasions. To overcome these variations, each envelope  $e$  was fitted to the corresponding reference envelope  $e_{ref}$  using the method of generalized least squares (GLS)

$$e = e_{ref}\theta + v, \quad (5.2)$$

where the parameters  $\theta$  were calculated as

$$\hat{\theta}_{GLS} = \left( e_{ref}^T W e_{ref} \right)^{-1} e_{ref}^T W e. \quad (5.3)$$

The weights on the diagonals of  $W$  in (5.3) were selected as the inverse variances  $\sigma_i^{-2}$  of the reference envelope to reduce the effect of changes in the resonance peak amplitudes between measurements:

$$W = \text{diag} \left( \frac{1}{\sigma_1^2}, \dots, \frac{1}{\sigma_N^2} \right). \quad (5.4)$$

After calculating the parameter  $\theta$ , the  $L_{GLS}$  metric was constructed by calculating the squared distances  $l_i$  between  $e_i$  and  $e_{ref,i}$ , scaled with pointwise variances of the reference envelope

$$l_i = \frac{1}{\sigma_{ref,i}^2} (e_i - \hat{e}_i)^2, \quad (5.5)$$

from which a sum over the  $N$  data points was calculated and scaled with the number of data points. To take into account the variability between individual reference envelopes, the result was also divided with the mean of fit difference sums  $\mu_{L_{GLS},ref}$  over the reference envelopes

$$L_{GLS} = \frac{\sum_{i=1}^N \frac{1}{\sigma_{ref}^2} (e_i - \hat{e}_i)^2}{N \mu_{L_{GLS},ref}}, \quad (5.6)$$

where  $\mu_{L_{GLS},ref}$  is

$$\mu_{L_{GLS},ref} = \frac{\sum_{k=1}^{n_{ref}} \left( \frac{\sum_{i=1}^N \frac{1}{\sigma_{ref,i}^2 (e_{ref,k,i} - \hat{e}_{ref,k,i})^2}}{N} \right)}{n_{ref}}. \quad (5.7)$$

In other words, the  $L_{GLS}$  essentially measures the sum of squared pointwise distances between  $e$  and  $e_{ref}$ , weighted by the inverses of the pointwise variance of  $e_{ref}$ . Thus, a value of  $L_{GLS} = 0$  corresponds to the reference envelope itself, and the higher the value, the more dissimilar  $e$  and  $e_{ref}$  are.

## 5.2 Machine learning classifiers

Although the  $L_{GLS}$  metric was successfully employed in **Publication I**, demonstrating differences between MLCC acoustic responses from bent and intact PCBs, two significant shortcomings were identified in it. First, determining whether a single component was damaged or not was challenging based on the  $L_{GLS}$  value alone, because the distributions of values from bent and intact PCBs overlapped. Secondly, the metric considered each data point in an envelope, which reduced the sensitivity to individual resonance peaks localized in a narrow frequency range.

To take into account these shortcomings, machine learning classifiers were taken into consideration. This decision was also supported by the need to create an NDT method that could be scaled to various types and sizes of MLCCs. Machine-learning-based classification for MLCCs was demonstrated in **Publication II**, in which a classifier known as the support vector machine was successfully trained to distinguish between damaged and bent-but-not-damaged MLCC samples. While the demonstration was performed with a small number of data using only two feature variables, the results showed that machine learning was a viable approach for the classification task. Thus, further research focused on developing machine-learning-based methods for MLCC acoustic data. For a broader assessment of the applicability of machine learning methods, several commonly used supervised classification algorithms were evaluated:

- Feedforward neural networks (FNN)
- Convolutional neural networks (CNN)
- Long-short term recurrent neural networks (LSTM)
- Support vector machines (SVM)
- Random forests (RF)
- $k$ -nearest neighbor classifiers ( $k$ -NN)

**k-NN** The  $k$ -nearest neighbors algorithm is one of the simplest ones in machine learning. The  $k$ -NN works by comparing a new point in the feature space with its  $k$  nearest neighbors, and it assigns the point to the same category as the majority of the neighbors. The only adjustable parameters are the number of neighbors,  $k$ ,

and the choice of the distance function (Russell and Norvig, 2009). The  $k$ -NN is a simple and intuitive method, but often does not work well with data that have a high dimensionality (Dougherty, 2013). In this work, the Euclidean distance metric with 12 nearest neighbors was found to result in accurate classification results while avoiding overfitting.

**SVM** The support vector machine works by fitting a hyperplane into the feature space so that it separates the data points in different categories by a largest possible margin (Cortes and Vapnik, 1995). However, the data are often not linearly separable, leaving the standard SVM algorithm unable to categorize the data correctly. This problem can be overcome by increasing the feature space dimensionality or by applying a kernel transformation to the input data. After this, a decision plane is fitted into the data in the modified feature space (Boser et al., 1992). As the hyperplane constructed by the SVM is a maximum margin separator, the method generalizes well to data outside the training set (Russell and Norvig, 2009). The application of machine learning classification to MLCC acoustic data was first demonstrated by using an SVM classifier in **Publication II**, and further work in **Publication III** was done by using a one-class support vector machine (OSVM), a variant of the SVM. The operational principles of both SVM and OSVM are discussed in greater detail in sections 5.2.1 and 5.2.2.

**Artificial neural networks** Artificial neural networks (ANN) are models that draw inspiration from biological neurons and can approximate any function given enough synapses and layers (Schmidhuber, 2015). They are also used as the basis of modern deep learning algorithms, e.g., in the form of convolutional (CNN), or recurrent neural networks, such as the LSTM. ANNs were chosen for this study as a reference algorithm because of their massive popularity in recent years. Neural networks are typically trained by backpropagation (Rumelhart et al., 1988), an algorithm that parallelizes very effectively. On the other hand, the complexity and training of an ANN has to be regulated to avoid overfitting (Goodfellow et al., 2016). In this work, a fully connected feedforward network (FNN) with a single hidden layer of 20 neurons was used, alongside various implementations of LSTM and CNN.

**Random Forest** The Random Forest algorithm is an ensemble method that combines the output of several decision tree classifiers. Each tree is trained using a randomly selected subset of the training data set, and each split in a tree is based on a randomly selected subset of input features (Breiman, 2001). This approach makes the algorithm more resilient to overfitting and imbalanced data, even though individual classification trees are prone to overfitting (Ho, 1995). The Random Forest has been shown to handle small, high-dimensional data sets well (Mellor et al., 2015). For this work, a Random Forest with 1000 decision trees was used.

Additionally, an algorithm known as the **t-SNE** (t-distributed stochastic neighbor embedding) was used for the analysis of MLCC acoustic data. While the t-SNE is not a

classification method, it is well-suited for clustering and visualizing data distributions (van der Maaten and Hinton, 2008). The t-SNE technique was applied to verify that the component samples tagged by the classifiers as "damaged" actually corresponded to a specific subset of samples in the 8-D representation. Furthermore, it was used to verify the X-ray and cross-section inspection results, as well as to examine potential differences between the acoustic responses of MLCCs of standard and flexible terminations. Other similar approaches, such as principal component analysis (PCA) (Pearson, 1901) and self-organizing maps (SOM) (Kohonen, 1982), were also evaluated, but t-SNE allowed for the best class separation in the 2-D representation of the data.

Each of the classifiers tested was trained and evaluated using a method known as the leave-one-out cross-validation (LOOCV) (Russell and Norvig, 2009). To make the classification task more tractable, preprocessing and feature extraction were performed on the data as described in Chapter 4. As the number of MLCC samples was limited, the aim of the classification task was also limited to identifying whether or not the component is damaged, instead of determining the type and degree of damage. The data from both damaged and undamaged capacitors were composed into one data set, and the models were trained on all but one sample, which was reserved for testing the classification performance of the model. This process was repeated for each sample in the data set, and the arithmetic mean of the test results was reported as the performance figure for each model.

Upon evaluating the classifiers, the use of deep learning models was experimented by testing CNN- and LSTM-based neural networks on raw acoustic data, downsampled to  $1 \cdot 10^3$  data points per signal. However, both of these models suffered from severe overfitting, as the dimensionality of the data was far greater than the number of MLCC samples available. Thus, the CNN- and LSTM-based models were dropped out of the comparison, and the study focused on the use of less complex classifiers ( $k$ -NN, SVM, ANN, and RF) trained on manually engineered structured data (as in Table 4.1) instead of downsampled time series data. The dataset, constructed as in (4.2) and (4.3), was then used to evaluate the performance of the classifiers in two configurations: using all eight features in Table 4.1, and in a reduced version, in which the variables  $f_1$ ,  $f_2$ , and  $f_{\text{median}}$  were dropped based on the importance analysis in Fig. 4.3. The classification results were also compared with the distribution of the MLCC data points. This was achieved by visualizing the eight-dimensional MLCC data in two dimensions using the t-distributed stochastic neighborhood embedding (t-SNE) algorithm.

The evaluation of the classifiers revealed no significant differences between the suitability of the models for the classification task (see Chapter 6). Although there were minor differences between the performances of the classifiers, the most limiting factors to the accuracy of the classification results were the small number of data points used for training the models and the inaccuracy of the labels within the training data, especially in the case of the component samples on the bent test PCB. As a solution, the research focused on the use of one-class learning models, which could be trained on only one class of data, i.e., the intact component samples. This approach would ensure that the labels for the

training data were correct, although the accuracy metrics would still contain uncertainty as the models were tested on data from samples that were visually inspected and labeled using X-ray and cross-sectioning. Methods such as the isolation forest (Liu et al., 2008) and one-class support vector machine were tested, out of which the one-class support vector machine was chosen because the ordinary SVM had proven a viable classifier in **Publication II**.

### 5.2.1 Support vector machine

In **Publication II**, automated discrimination between damaged and bent-but-not-damaged MLCCs was demonstrated using a support vector machine (SVM). The SVM is a binary classifier, i.e., a machine learning algorithm that works by fitting a hyperplane between  $N$  points of  $D$  dimensions  $x \in \mathbb{R}^{N \times D}$  from two different classes  $y \in \{-1, 1\}$  so that the margin between the points and the hyperplane is maximized (Cortes and Vapnik, 1995). In case there exists  $\mathbf{w}$ ,  $b$  such that

$$\mathbf{w} \cdot \mathbf{x} - b = 0, \quad (5.8)$$

the data set  $\mathbf{x} = \{(x_1, y_1), \dots, (x_N, y_N)\}$  is called *linearly separable*, i.e., the points from different classes can be perfectly separated by a hyperplane described by the normal vector  $\mathbf{w}$ . The hyperplane, also known as the decision plane, is defined based on the training data  $x \in \mathbb{R}^{N \times D}$ . However, not all instances of  $X$  are needed for constructing the hyperplane; instead, the optimal hyperplane  $w_0$  can be described as a linear combination of points closest to the plane, i.e., support vectors  $x_i \in \text{SV}$  (Cortes and Vapnik, 1995) as

$$w_0 = \sum_{i \in \text{SV}} \alpha_i x_i, \quad (5.9)$$

where  $\alpha_i$  and  $b$  are the weights and the bias term that are computationally optimized, i.e., the SVM model is trained on the examples  $\mathbf{x}$ . A trained SVM model can be used to classify new instances  $x$  of an unknown class by evaluation of the linear decision function (Cortes and Vapnik, 1995)

$$I(x) = \text{sgn} \left( \sum_{i \in \text{SV}} \langle \alpha_i x_i, x \rangle + b_0 \right). \quad (5.10)$$

However, the points from different classes are often not linearly separable, i.e., the classes cannot be separated by a plane. While this problem can be alleviated by assigning a penalty term to each point falling within the wrong side of the decision place (a *soft-margin SVM*), a more common solution is to employ a technique known as the kernel method (Boser et al., 1992). This approach facilitates the formulation of a nonlinear classifier by transforming each pair of data points  $(x_i, x_j) \in \mathbf{x}$  into a higher-dimensional space, where the problem often becomes linearly separable. The transformation is achieved by using a mapping  $\Phi$  defined by a kernel function  $\kappa(x_i, x_j)$

$$\kappa(x_i, x_j) = \langle \Phi(x_i), \Phi(x_j) \rangle. \quad (5.11)$$

In the transformed feature space, the decision function corresponding to (5.10) becomes

$$I(x) = \text{sgn} \left( \sum_{i \in \text{SV}} y_i \alpha_i \kappa(x_i, x) + b \right), \quad (5.12)$$

i.e., the point  $x$  is evaluated with each support vector  $x_i$  by using the kernel function  $\kappa$  (Boser et al., 1992). A common choice for  $\kappa$  is the Gaussian radial basis function (RBF) (Bounsiar and Madden, 2014)

$$(x_i, x_j) = e^{-\frac{\|x_i - x_j\|^2}{\gamma}}, \quad (5.13)$$

where  $\gamma$  controls the bandwidth of the kernel function. Decreasing  $\gamma$  can be interpreted as increasing the range of influence of the kernel function  $\kappa$  in the transformed feature space, and in turn, reducing the complexity of the decision surface.

### 5.2.2 One-class support vector machine

The OSVM (Schölkopf et al., 2001) is a variant of the normal support vector machine (SVM), which is used for modeling the distribution of data points from a single class. In contrast to the normal SVM, which separates the two classes by a decision boundary, the OSVM, instead, separates the data points from the origin, typically in a feature space created by using a kernel transformation (5.11). The formulation of the OSVM is similar to the regular SVM. Instead of constructing a hyperplane separating two classes as in (5.9), the hyperplane  $w$  separates the points  $\mathbf{x}$  from the origin. The hyperplane  $w$  is found by solving a quadratic problem

$$\min \frac{1}{2} \|w\|^2 + \frac{1}{vN} \sum_i \xi_i - b \quad (5.14)$$

subject to

$$(w \cdot \Phi(x_i)) \geq b - \xi_i, \quad \xi_i \geq 0, \quad (5.15)$$

where  $b$  is a bias term, and  $\xi_i$  are slack variables for each support vector (Schölkopf et al., 2001). The first term in (5.14) is a regularizer that minimizes the complexity of the decision plane by minimizing the squared norm  $\|w\|^2$ . The second term seeks to minimize the number of misclassifications within the training data, i.e., the points that fall on the wrong side of the decision plane. This trade-off between the complexity of the model and the number of misclassifications allowed for the training data  $\mathbf{x}$  is controlled by the term  $v \in (0, 1]$  in (5.14). Akin to the ordinary SVM, the resulting decision function can be expressed as (5.10). Applying the kernel transformation (5.11), the decision function  $I$  for the OSVM becomes (Schölkopf et al., 2001)

$$I(x) = \text{sgn} \left( \sum_i \alpha_i \kappa(x_i, x) - b \right). \quad (5.16)$$



Although the expression (5.16) can be evaluated by using any function  $\kappa$  qualifying as a kernel, it has been shown that the radial basis functions, such as the Gaussian kernel (5.13), are typically the best-performing kernels and even the only viable choice for one-class classification tasks (Bounsiar and Madden, 2014). Thus, OSVM-based anomaly detection and classification applications typically use the Gaussian kernel (Anaissi et al., 2018; Das et al., 2007; Mun et al., 2020; Yan et al., 2017).

### 5.2.3 OSVM hyperparameter optimization

The classification performance of any machine learning model is controlled by adjusting the hyperparameters of the model, i.e., the parameters that are fixed before the process of fitting the model into a set of data. Careful selection of the hyperparameters is crucial for ensuring that the model can correctly classify previously unseen instances while avoiding overfitting to the training data.

For one-class SVM, the classification performance is typically controlled by two hyperparameters. The parameter  $\nu \in (0, 1]$  adjusts the trade-off between the regularizer term  $\|w\|$  and the number of training points allowed on the wrong side of the decision plane in (5.14). As such, the value of  $\nu$  is equal to the fraction of outliers within the training data (i.e., data points which fall outside the decision boundary), as well as the fraction of support vectors within the training data (Schölkopf et al., 2001). Therefore, increasing the value of  $\nu$  results in a higher fraction of data points being assigned as support vectors, which, in turn, leads to a more complex decision function (5.16).

On the other hand, the selection of the kernel  $\kappa$  can have a high impact on the performance of the model. For the Gaussian RBF, the most widely used kernel for OSVMs, the shape (or bandwidth) of the kernel is directly controlled by the term  $\gamma$ : increasing the value of  $\gamma$  decreases the value of the kernel (5.13) at a given distance  $\|x_i - x_j\|$ , effectively decreasing “the range of influence” for individual support vectors. This, in turn, results in a tighter, more complex decision surface.

Selecting the hyperparameters for one-class SVM is not a trivial task. Owing to the nature of the one-class classification problem, data are often available only from a single class, or the number of samples representing other classes is limited. If a sufficient number of counterexamples are available, the hyperparameter selection can be performed by validating the performance of the model on both the target and outlier data by using conventional methods such as grid search (Goodfellow et al., 2016). However, in the absence of outlier examples, tuning the hyperparameters becomes more challenging because the sensitivity of the model to outliers cannot be evaluated directly (Wang et al., 2018; Xiao et al., 2015).

Several approaches have been proposed for solving the hyperparameter selection problem by using data only from the target class. These techniques are typically based on either heuristics or synthetically generating outlier examples (Wang et al., 2018). However,

many of the proposed approaches only optimize for the kernel parameter  $\gamma$ , requiring prior knowledge for setting the parameter  $\nu$  (Anaissi et al., 2018; Unnthorsson et al., 2003; Xiao et al., 2015). For the case of detecting damaged MLCCs, such approaches were deemed not viable because there was no *a priori* knowledge on how to set the value for  $\nu$ .

A recent, outlier-generation-based method known as the SDS has been shown to rival or outperform many other techniques (Wang et al., 2018). The algorithm is based on detecting the “edge patterns” within the training data, i.e., the samples that lie at the edge of the training data. For each edge pattern, the algorithm generates a pair of synthetic outlier and target points, which are then used for evaluating the performance of the OSVM classifier by using the grid search technique. For **Publication III**, this algorithm was implemented in MATLAB for detecting damaged MLCCs. However, the algorithm did not yield unambiguous values for  $\nu$  and  $\gamma$ ; instead, the OSVM reached 100% accuracy on multiple  $(\nu, \gamma)$  values. When testing the model on actual MLCC data, the classification performance varied widely depending on the choice of  $\nu$  and  $\gamma$ . This behavior was traced back to the combination of a low number of MLCC data points and the high dimensionality of the data, which resulted in nearly all data points being identified as edge patterns.

#### 5.2.4 Cliffhanger algorithm

As a solution to the problem of choosing the hyperparameters for the OSVM, a novel optimization algorithm was introduced in **Publication III**. The algorithm employs a simple heuristic approach for finding suitable values for  $\nu$  and  $\gamma$  by performing a grid search over a  $(\nu, \gamma)$  plane. As there are no outlier data available for the optimization process, the algorithm only evaluates the target class accuracy for the OSVM at each grid point.

Certain  $(\nu, \gamma)$  values will result in a decision boundary that encloses the training data with a wide margin. Such hyperparameters yield a high target class accuracy; however, the model is insensitive to outliers. On the other hand, some  $(\nu, \gamma)$  values will yield an overly complex decision boundary that encloses the training data with a very narrow margin. Such a model is sensitive to outliers but also prone to false alarms.

Because the OSVM attempts to enclose all the training data points by the decision boundary, the evaluation of the accuracy on the target class must be performed on samples not included in the training data. To this end, the evaluation is performed using a method known as the leave-one-out cross-validation (LOOCV): the model is trained on all but one sample of data, and the performance is then tested on the left-out sample, repeating the process for all samples in the training set. The key idea is to observe the performance of the OSVM model with respect to the target class accuracy  $A$  by applying the LOOCV process over a grid of  $(\nu, \gamma)$  values (see Fig. 5.2).

The intuition behind the algorithm is to select the values for  $\nu$  and  $\gamma$  from the  $(\nu, \gamma)$  plane

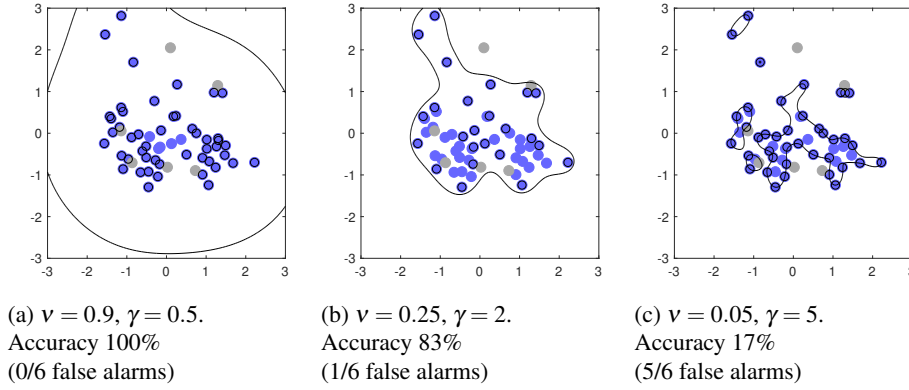


Figure 5.1. Effect of hyperparameters  $\nu$  and  $\gamma$  on the decision boundary of an OSVM trained on target data (blue points). The gray dots represent the test data, belonging to the same class as the blue dots. The black line indicates the decision boundary, with support vectors being marked with black circles. In (a), increasing  $\nu$  and decreasing  $\gamma$  results in a crude decision boundary, which is not efficient for detecting anomalies. On the other hand, decreasing  $\nu$  and increasing  $\gamma$  too much (c) will result in an overly complex model that will yield many false alarms. Optimal values for  $\nu$  and  $\gamma$  (b) can be determined by repeatedly leaving out a single point of training data, and using them to evaluate the performance of the model. These figures were plotted using two-dimensional data (features  $A_1$  and  $A_2$  on intact PCB 1) to illustrate the operation of the hyperparameter selection algorithm and were not used for further analysis.

satisfying the following heuristic conditions:

1. The target class accuracy of the model should be high, i.e., the model correctly classifies target class data most of the time.
2. The decision boundary should wrap tightly around the set of training points so that even a small increase in the complexity of the decision surface results in a significant decrease in target class accuracy.

To satisfy the aforementioned conditions, the algorithm seeks to locate a “critical point”  $(\nu_c, \gamma_c)$  within the  $(\nu, \gamma)$  plane where the Laplacian of the accuracy reaches its highest negative value

$$(\nu_c, \gamma_c) = \arg \min_{\nu, \gamma} (\nabla^2 \mathbf{A}), \quad (5.17)$$

where  $\nabla^2$  is the discrete version of the Laplace operator,

$$\nabla^2 \mathbf{A} = \nabla \cdot \nabla \mathbf{A} = \frac{\partial^2 \mathbf{A}}{\partial \nu^2} + \frac{\partial^2 \mathbf{A}}{\partial \gamma^2}. \quad (5.18)$$

In other words, (5.17) locates the sharpest point within the accuracy surface  $\mathbf{A}$  where  $\mathbf{A}$  reaches its highest downward curvature (see Fig. 5.2). The experiments in **Publication**

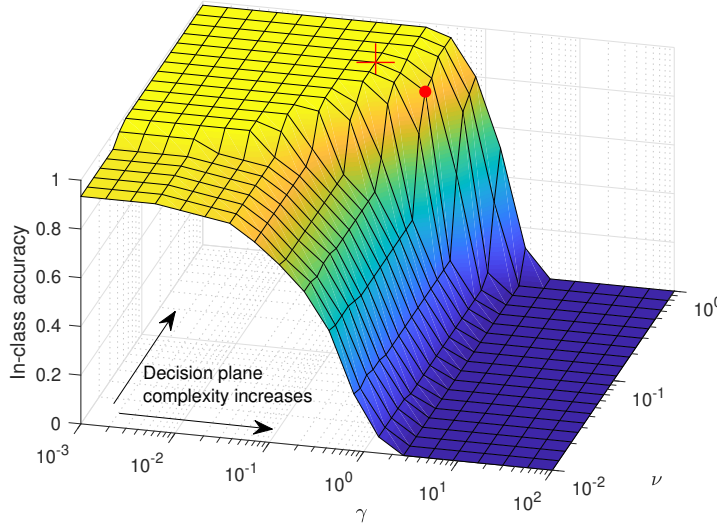


Figure 5.2. In-class accuracy of an OSVM for different combinations of  $\nu$  and  $\gamma$ , evaluated using the leave-one-out cross-validation technique. Choosing the hyperparameters so that  $\nu$  is close to 1 and  $\gamma$  is very small results in a high in-class accuracy, but the model will be insensitive to outliers. The Cliffhanger algorithm locates the critical point  $(\nu_c, \gamma_c)$  (the red dot), i.e., the global minimum of the Laplacian of the in-class accuracy surface  $\mathbf{A}$ . When the threshold condition (5.19) is applied, the point closest to  $(\nu_c, \gamma_c)$  in terms of grid coordinates, with the in-class accuracy exceeding the threshold condition, is returned as the optimal combination of hyperparameters  $(\nu_{\text{opt}}, \gamma_{\text{opt}})$ .

**III** show that selecting the hyperparameters according to the critical point (5.17) typically yields classification results comparable with other proposed OSVM hyperparameter optimization techniques.

The Cliffhanger algorithm was implemented in MATLAB for **Publication III**, and was then used for detecting anomalous MLCC acoustic signatures. The first part of the algorithm, Algorithm 2, performs a search over an  $n_{\text{grid}}$ -by- $n_{\text{grid}}$  grid of  $(\nu, \gamma)$  values, evaluating the target class accuracy  $A$  of the OSVM at each grid point by using the LOOCV method. The second part of the Cliffhanger algorithm, Algorithm 3, locates the critical point within  $\mathbf{A}$  according to (5.17).

Because the target class accuracy may not reach 100% at  $(\nu_c, \gamma_c)$ , an additional condition for selecting the hyperparameters was implemented in Algorithm 3. For classification tasks where a high target class accuracy should be prioritized over sensitivity to outliers, the hyperparameters can be chosen as a point in the  $(\nu, \gamma)$  grid closest to  $(\nu_c, \gamma_c)$  that satisfies a predetermined condition for target class accuracy. In **Publication III**, such a condition  $T$  was chosen as

$$T = \max(\mathbf{A}) \quad (5.19)$$

to maximize the resulting target class accuracy, at the cost of sensitivity to outliers.

The Cliffhanger algorithm was tested on eight benchmark data sets from the UCI machine learning repository (Dua and Graff, 2017), which also had previously been used for testing other OSVM hyperparameter optimization algorithms (Anaissi et al., 2018; Xiao et al., 2015). The results in **Publication III** show that applying the condition in (5.19) yields a lower number of false alarms on MLCC data, even though omitting the threshold results in a better overall performance across the benchmark data sets. The full list of the benchmark test results can be found in the appendix of **Publication III**.

---

**Algorithm 2** ( $v, \gamma$ ) –performance surface mapping

---

**Require:** Input data matrix  $\mathbf{X} = (\mathbf{x}_1 \dots \mathbf{x}_n)^T \in \mathbb{R}^{N \times D}$  (intact MLCCs)  
*#Set parameters for grid mapping*  
Set  $n_{\text{grid}} \leftarrow 20$   
Set log-spaced range of  $n_{\text{grid}}$  points  $v \leftarrow \{10^{-2} \dots 10^0\}$   
Set log-spaced range of  $n_{\text{grid}}$  points  $\gamma \leftarrow \{10^{-3} \dots 10^2\}$   
Preallocate accuracy matrix  $\mathbf{A} = (a_{i,j}) \in \mathbb{R}^{n_{\text{grid}} \times n_{\text{grid}}}$   
*#Partition data for leave-one-out cross-validation*  
**for**  $n = 1$  to  $N$  **do**  
*#Perform grid mapping over hyperparameter space using partitioned data*  
Set  $(\mathbf{X}_{\text{train}}, \mathbf{Y}_{\text{train}}) = (\mathbf{X} \setminus \{\mathbf{x}_n\}, \mathbf{0}^{(N-1) \times 1})$   
Set  $(\mathbf{X}_{\text{test}}, \mathbf{Y}_{\text{test}}) = (\mathbf{x}_n, 0)$   
**for**  $i = 1$  to  $n_{\text{grid}}$  **do**  
**for**  $j = 1$  to  $n_{\text{grid}}$  **do**  
Train one-class SVM( $v_i, \gamma_j$ ) on  $(\mathbf{X}_{\text{train}}, \mathbf{Y}_{\text{train}})$   
Evaluate the SVM on  $(\mathbf{X}_{\text{test}}, \mathbf{Y}_{\text{test}})$   
Calculate evaluation accuracy  $acc_{v,\gamma}$   
Update  $a_{i,j} \leftarrow a_{i,j} + acc_{v,\gamma}$   
**end for**  
**end for**  
**end for**  
**return**  $(1/N) \cdot \mathbf{A}$

---

---

**Algorithm 3** Hyperparameter selection

---

**Require:** Accuracy matrix  $\mathbf{A} = (a_{i,j})$   
**Require:** Hyperparameter grid  $(\mathbf{v}, \gamma)$   
**Require:** Threshold switch  $s \in \{True, False\}$   
**Require:** Threshold value  $T$   
 Calculate discrete Laplacian  $\nabla^2 \mathbf{A}$   
 Find grid coordinates  $(i_c, j_c) \leftarrow \arg \min_{i,j} (\nabla^2 \mathbf{A})$   
 Set critical point  $(\mathbf{v}_c, \gamma_c) = (\mathbf{v}(i_c), \gamma(j_c))$   
**if**  $s = False$  **or**  $\mathbf{A}(i_c, j_c) \geq T$  **then**  
     Set  $(\mathbf{v}_{opt}, \gamma_{opt}) \leftarrow (\mathbf{v}_c, \gamma_c)$   
**else**  
     Set  $(\mathbf{v}_{opt}, \gamma_{opt}) \leftarrow \arg \min_{(i,j) \in \arg \max \mathbf{A}} \|(i, j) - (i_c, j_c)\|_2$   
**end if**  
**return**  $((1 - 1/N)\mathbf{v}_{opt}, \gamma_{opt})$

---

### 5.3 Evaluation methods

Various classification techniques were applied to identify damaged MLCCs throughout this dissertation. The task was approached as a binary classification problem: for a given MLCC sample, the possible outcome is either negative (N) ("0", or no damage), or positive ("1", the component is damaged). During evaluation, the classifiers were presented with feature vectors  $x$  derived from acoustic measurement data. For each MLCC sample the models were tested for, the classification task had four possible outcomes  $y$ : **True Negative** (TN, correctly classified as undamaged); **False Negative** (FN, classified as undamaged but actually damaged); **True Positive** (TP, correctly classified as damaged); and **False Positive** (FP, classified as damaged although undamaged).

When tested on a set of  $N_{\text{test}}$  samples  $X$

$$X = \{(x_i, y_i) \mid i = 1 \dots N_{\text{test}}\}, \quad (5.20)$$

the classification outcomes can be represented as a confusion matrix

$$\begin{array}{c} \text{Outputs} \\ \begin{array}{cc} 0 & 1 \end{array} \begin{pmatrix} \text{TP} & \text{FP} \\ \text{FN} & \text{TN} \end{pmatrix} \\ \begin{array}{cc} 1 & 0 \end{array} \\ \text{Targets} \end{array} \quad (5.21)$$

The accuracy of the model is defined as the ratio between correct classifications and all instances within the testing set:

$$\text{Accuracy} = \frac{\text{TP} + \text{TN}}{\text{TP} + \text{FP} + \text{FN} + \text{TN}}. \quad (5.22)$$

However, if the set is heavily imbalanced, i.e., one class of  $y$  outnumbers the other, high accuracy values can be obtained even if the model is incapable of correctly classifying any of the samples in the minority class. For such an imbalanced data set, a more informative indicator of the model performance is the Matthews correlation coefficient (MCC)  $\in [-1, 1]$ , defined as

$$\text{MCC} \in [-1, 1] = \frac{\text{TP} \cdot \text{TN} - \text{FP} \cdot \text{FN}}{\sqrt{(\text{TP} + \text{FP})(\text{TP} + \text{FN})(\text{TN} + \text{FP})(\text{TN} + \text{FN})}}. \quad (5.23)$$

Unlike accuracy, the Matthews correlation coefficient takes into account the imbalance between classes, and is also invariant to swapping the classes (Chicco and Jurman, 2020). Thus, MCC can be considered a more reliable indicator of performance for use cases where a significant class imbalance can be expected.

While the confusion matrix, and its derived metrics, such as accuracy and MCC, can be used to assess the classification performance of a model, they only represent the classification results at a single classification threshold. For example, the decision function for

the SVM (5.10) and the OSVM (5.16) place the classification threshold at zero: if the value output by the classifier is greater than zero, the output is designated in one class, and vice versa. A similar convention is used for other common classification models, such as neural networks and random forests (Russell and Norvig, 2009). However, the output values of such classifiers are typically continuous instead of discrete, and using a single metric, such as accuracy or MCC, does not reveal by how great a margin the threshold value is exceeded or not, nor can they be used for fine-tuning the output of the classifier.

The most common way of visualizing the output from a binary classifier without a classification threshold applied is the receiver operating characteristic (ROC) curve. In the ROC, the outputs of the model are plotted in 2D coordinates, defined by the **true positive rate** (TPR, also known as *sensitivity* or *recall*) and **false positive rate** (FPR) of the classifier:

$$\text{TPR} = \frac{\text{TP}}{\text{TP} + \text{FN}} \quad (5.24)$$

$$\text{FPR} = \frac{\text{FP}}{\text{FP} + \text{TN}} \quad (5.25)$$

Each of  $N_{\text{test}}$  samples is plotted in the TPR–FPR plane by setting the output value corresponding to the sample as the threshold value and calculating the corresponding TPR and FPR values. On a balanced data set, an ideal classifier would attain a TPR of 1 without false positives, whereas random guessing would result in an equal ratio between the TPR and the FPR. The area under the ROC curve (AUC-ROC) is also commonly used to describe the overall performance of a classifier, with the AUC-ROC of 1 corresponding to an ideal classifier and the AUC-ROC of 0.5 being equivalent to random guessing (Fawcett, 2004).

However, the ROC curve is not invariant to class imbalance. Specifically, if the negative instances significantly outnumber the positive ones, a classifier incapable of correctly detecting the majority of positive samples can still yield AUC-ROC values far greater than 0.5. Another visualization technique similar to the ROC curve is the precision-recall (PR) curve. In the PR curve, recall (TPR) values are plotted against precision, defined as

$$\text{Precision} = \frac{\text{TP}}{\text{TP} + \text{FP}}, \quad (5.26)$$

which essentially describes how many of the positive classifications are relevant. As with the ROC curve, the area under the PR curve (AUC-PR) can be used as a measure of the performance of a classifier (Manning et al., 2012).

### 5.3.1 Confusion river graph

While the ROC and PR curves are widely employed for the evaluation of binary classification algorithms, they fail to visualize all four possible outcomes within the confusion matrix (5.21). However, they can be used to interpret the classification performance



across multiple classification thresholds, which the confusion matrix is incapable of. To combine the classification threshold information in the ROC and PR curves with the completeness of the confusion matrix, a new visualization technique called the *confusion river* is proposed.

Essentially, the confusion river visualizes the information contained in a 2-by-2 confusion matrix as two vertically stacked area plots. Both areas correspond to the subsets of samples within the two target classes. Akin to the ROC curve, the effect of varying the discrimination threshold of the classifier is visualized along the horizontal axis as the ratio of correct and incorrect classification outcomes. This approach facilitates the visualization of the classifier output across the full range of the output values of the model, and can be used to interpret the classification performance at various threshold levels. Moreover, the surface area of the “river,” on a scale between 0 and 1, can be interpreted as an overall measure for the performance of the classifier. The total area of the river (AUC-CR) can be calculated by integrating over the range of threshold values  $T$

$$\begin{aligned} \text{AUC-CR} &= \frac{1}{2} \left( \int_{\min T}^{\max T} \text{TPR}(T) dT + \int_{\min T}^{\max T} \text{TNR}(T) dT \right) \\ &= \frac{1}{2} \left( \int_{\min T}^{\max T} \frac{\text{TP}(T)}{N_P} dT + \int_{\min T}^{\max T} \frac{\text{TN}(T)}{N_N} dT \right), \end{aligned} \quad (5.27)$$

using the trapezoidal method. In (5.27), the range of threshold values  $T$  is scaled between 0 and 1, and  $N_P$  and  $N_N$  indicate the total number of positive and negative instances, respectively. Thus, both integral terms range between 0 and 1, and the end result is multiplied by 1/2 to scale the AUC-CR value between 0 and 1.

## 6 Results and discussion

Although various classification methods were evaluated for the task of identifying damaged MLCCs, the research eventually settled on the application of the one-class support vector machine (OSVM). The main motivation for choosing the one-class classifier was that in a production line environment, data collection would have to be performed for each specific kind of MLCCs that would be screened for faults. Collecting data from intact component samples only is a process far easier than adding various examples of damaged capacitors, because the components would have to be deliberately damaged, and then, the presence of damage would have to be verified by other screening methods.

The performance of the OSVM was evaluated on the acoustic measurement data collected as described in Chapter 2. Training, optimization, and testing of the model were performed on the acoustic data set, which was constructed as discussed in Chapter 4.

### 6.1 OSVM test protocol

The evaluation of the OSVM was conducted in two stages. First, the model was optimized on data from PCB 2, which was not subjected to the controlled bending procedure. The Cliffhanger algorithm (see section 5.2.4) was used for finding the optimal hyperparameters for the OSVM by using only data from intact MLCCs. After optimizing the parameters, the model was trained on the same data.

With the model optimized and trained, the performance of the model was tested on two sets of data. First, the ability of the OSVM to discriminate between damaged and undamaged component samples was tested on data collected from PCB 1 after the board had been subjected to the bending procedure (see Table 4.2). By using data from the capacitor samples from a PCB another than the model was trained on, the generalizability of the OSVM could be tested for possible intrinsic variations between the two sets of MLCCs.

After evaluating the OSVM on the MLCC samples from the bent PCB 1, the model was tested on the data from the same test board before the bending procedure. The pristine component samples thus served as a control population, with the purpose of ensuring that the model would correctly generalize to data from another population without yielding

false alarms.

The use of nonbent MLCCs from PCB 1 as a control population also served another purpose. Because the samples on PCB 1 were labeled by visually inspecting the X-ray and cross-section images after the bending procedure (see section 1.2), the accuracy of the labels could not be guaranteed. In other words, samples labeled as "0" (undamaged) could actually have been damaged, and vice versa. Thus, the test results on the known-intact MLCC data were considered more reliable than the ones on the data collected after the bending, as the accuracy of the ground truth labels did not depend on the visual inspection process.

## 6.2 OSVM test results

The performance of the OSVM, as with any machine learning classifier, depends on the feature variables supplied to the model. In **Publication III**, the model was tested on various combinations of input features. The features were grouped according to the physical phenomenon they represented (amplitude, frequency, or phase), and the classifier was evaluated on the following combinations of feature variables: amplitude; frequency; phase; amplitude and frequency; amplitude and phase; frequency and phase; and finally, using all eight feature variables.

### 6.2.1 Overview

The evaluation results in Table 6.1 show that for the component samples on the bent PCB 1, the best classification results in terms of MCC and Recall scores were obtained using all the eight feature variables. In other words, using all the feature variables led to the model discovering the highest percentage of the damaged samples. However, when tested on samples from PCB 1 before bending, using all the feature variables resulted in an accuracy just over 51 %, i.e., half of the intact samples triggered a false alarm. However, testing the model on a data set combined from the same MLCC samples from before and after bending showed that the best classification results were obtained with the amplitude-based features alone (MCC), or by combining the amplitude-based features with those extracted from the phase responses (AUC-ROC). The reason for the higher performance scores on the combined data set can be found in the classification results on the intact MLCCs. Both amplitude and the combination of amplitude and phase yielded an accuracy score of over 96 % on the intact PCB 1, a figure significantly higher than by using all the eight feature variables. Moreover, using only the phase-related features yielded an even higher score of over 98 %, with fairly good performance figures on the bent capacitor samples. The classification results were also visualized by using the Receiver Operating Characteristic (ROC) curve (Fig. 6.1), which reveals that the features based on amplitude

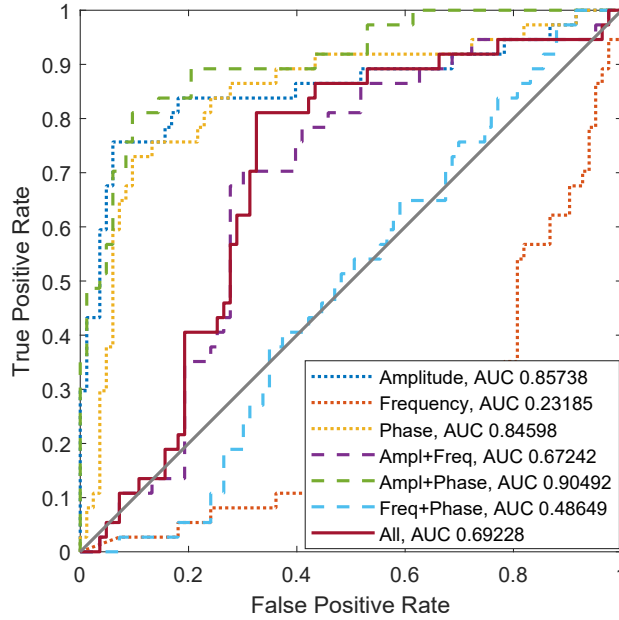


Figure 6.1. ROC graphs depicting the performance of the OSVM using different sets of input features. The performance of the OSVM is highly dependent on the choice of features, with the best AUC score obtained on the combination of amplitude- and frequency-based features. The performance of the classifier was evaluated on data collected from PCB 1 both before and after bending, with the model trained on a separate set of intact MLCCs from PCB 2.

and/or phase result in a significantly better overall performance than any combination of features with frequency-based variables included.

## 6.2.2 Further analysis

Continuing from the results published in **Publication III**, the effects of different feature combinations on the OSVM performance were further studied by visualizing the raw output values from the OSVM, i.e., without applying the signum function in (5.16). This was achieved by using the confusion river visualization technique presented in section 5.3.1.

Figs. 6.3a–6.3g show confusion river visualizations for the OSVM classification results on the combined data set constructed by merging acoustic data from PCB 1 before and after subjecting the test PCB to bending. Fig. 6.3c shows that the phase-related features are particularly resilient to false positives across a wide range of threshold values, suggesting that the use of phase-based features results in a classifier with a lower parameter sensitivity regarding the choice of the threshold value, at the cost of a higher number of false negatives. On the other hand, features based on the amplitude result in a classifier are

Table 6.1. Results from the evaluation of the OSVM classifier using various performance metrics. The model was tested on data from the test PCB 2, collected both before and after subjecting the circuit board to controlled bending. Hyperparameter optimization and model training were performed on a separate set of acoustic data from another, intact test board (PCB 2). The process of hyperparameter optimization, training, and testing was repeated separately using several combinations of input features, which were grouped according to the physical quantity (amplitude, frequency, phase) they represent.

Input features	(feat.#)	PCB 1, before bending			
		Accuracy (%)			
Amplitude	(1,2,6)	96.67			
Frequency	(3,4,7)	30.00			
Phase	(5,8)	<b>98.33</b>			
Amplitude + Freq	(1,2,3,4,6,7)	43.33			
Amplitude + Phase	(1,2,5,6,8)	96.67			
Freq + Phase	(3,4,5,7,8)	23.33			
All	(1-8)	51.67			

Input features	(feat.#)	PCB 1, after bending			
		Accuracy (%)	Precision	Recall	MCC
Amplitude	(1,2,6)	75.00	0.8235	0.7567	0.4865
Frequency	(3,4,7)	43.33	0.8000	0.1081	0.1137
Phase	(5,8)	68.33	0.7364	0.7568	0.3248
Amplitude + Freq	(1,2,3,4,6,7)	78.33	<b>0.8333</b>	0.8108	0.5458
Amplitude + Phase	(1,2,5,6,8)	73.33	0.7692	0.8108	0.4276
Freq + Phase	(3,4,5,7,8)	61.67	0.7059	0.6487	0.2098
All	(1-8)	<b>80.00</b>	0.8205	<b>0.8649</b>	<b>0.5714</b>

Input features	(feat.#)	PCB 1, before & after combined			
		Accuracy (%)	Precision	Recall	MCC
Amplitude	(1,2,6)	<b>85.83</b>	<b>0.7778</b>	0.7568	<b>0.6655</b>
Frequency	(3,4,7)	36.67	0.0851	0.1081	-0.3879
Phase	(5,8)	83.33	0.7180	0.7568	0.6155
Amplitude + Freq	(1,2,3,4,6,7)	60.83	0.4286	0.8108	0.3081
Amplitude + Phase	(1,2,5,6,8)	85.00	0.7317	0.8108	0.6605
Freq + Phase	(3,4,5,7,8)	42.50	0.3000	0.6487	-0.0255
All	(1-8)	65.83	0.4706	<b>0.8649</b>	0.4018

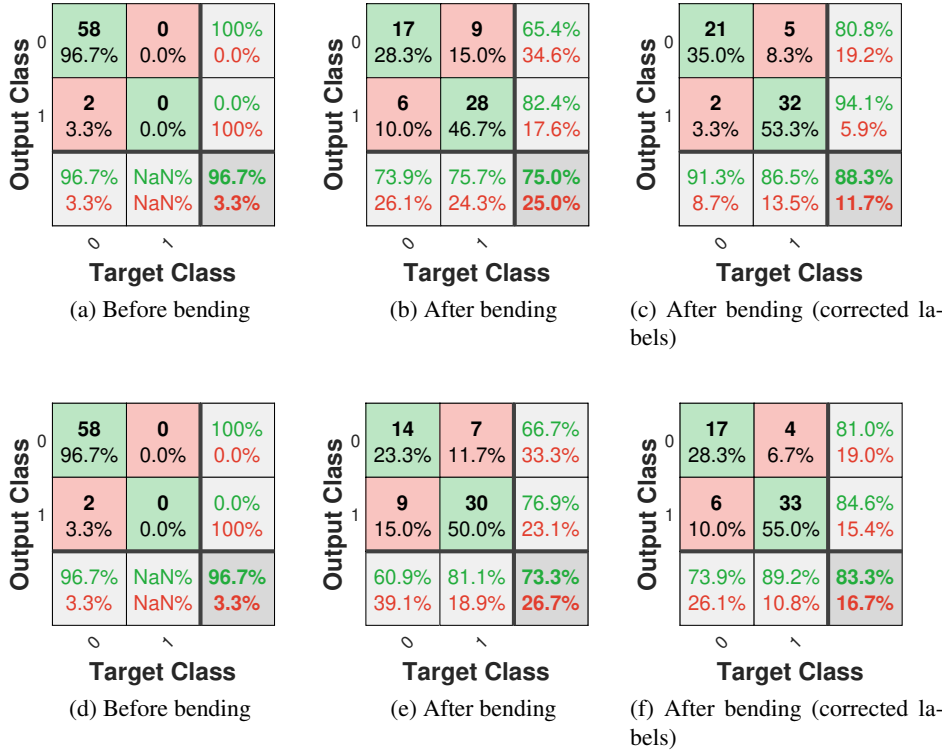


Figure 6.2. Confusion matrices for OSVM test results. Top row: amplitude-based features only; bottom row: amplitude- and phase-based features. The effect of the reinspection of the target labels is also shown, although the non-reinspected results are reported as the final performance values.

more effective in discovering true positives (see Fig. 6.3a) than those based on frequency or phase.

Unlike with the ROC graph in Fig. 6.1, the best performance in terms of area-under-confusion-river (AUC-CR) is obtained using phase-based features only, slightly exceeding the AUC-CR yielded by the combination of features based on amplitude and phase. While both the AUC-ROC and the AUC-CR consider the overall performance of the classifier across a range of threshold values rather than a single operating point, the AUC-CR places an even weight on both positive and negative output classes, whereas the AUC-ROC only considers positive classifier output values. Nevertheless, setting the threshold value at 0, the results in Table 6.1 suggest that the use of amplitude-based features alone yields a slightly better performance in terms of MCC than amplitude, phase, or the combination of the two.

The majority of the results (Figs. 6.3a, 6.3c, 6.3d, 6.3e, and 6.3g) show a distinct plateau

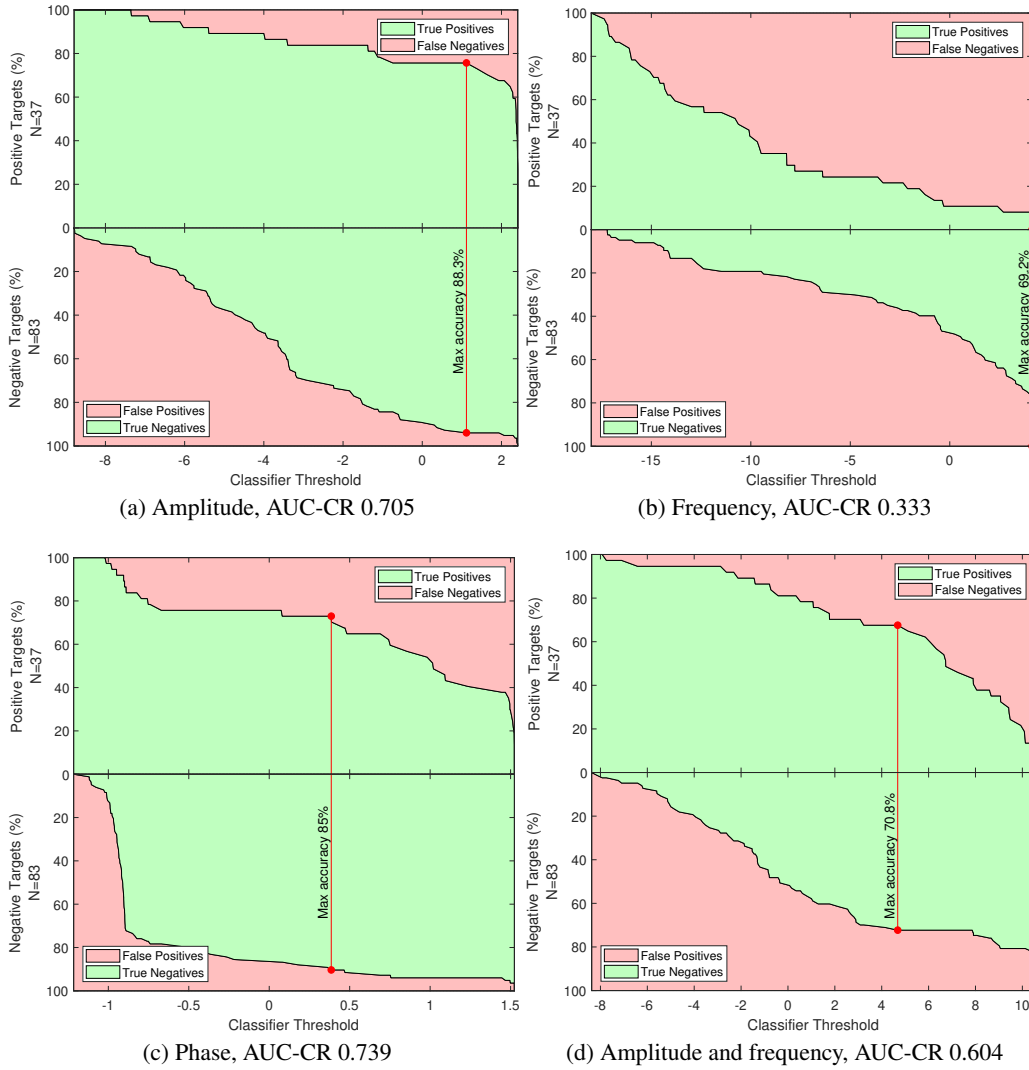
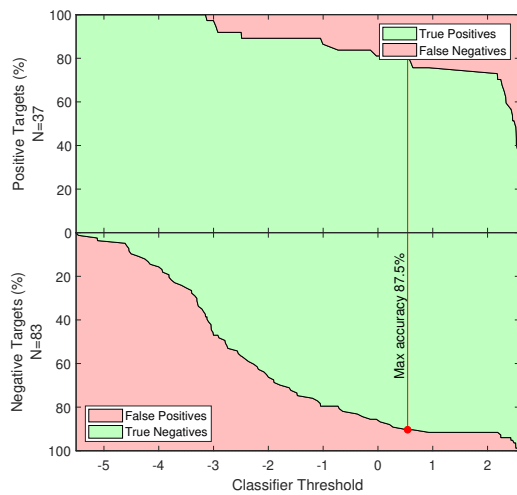
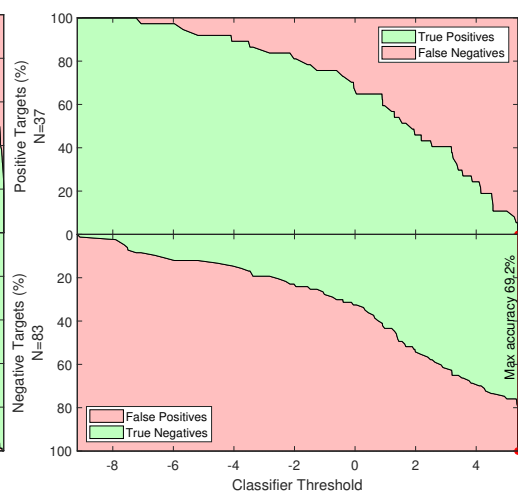


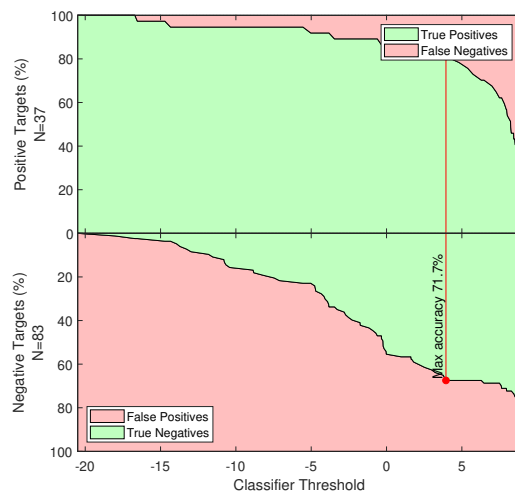
Figure 6.3. Confusion river visualizations depicting the performance of the OSVM using different sets of input features. Although the highest scores in terms of MCC and AUC-ROC are obtained using features based on amplitude, or amplitude and phase, using the phase-based features only yields the highest AUC-CR score.



(e) Amplitude and phase, AUC-CR 0.735



(f) Frequency and phase, AUC-CR 0.508



(g) All features, AUC-CR 0.599

Figure 6.3. (continued).



for the true negative rate at threshold values above the maximum accuracy, whereas the true positive rate decreases. In other words, raising the classification threshold causes the model to miss increasing amounts of damaged component samples, without decreasing the number of false alarms. A possible explanation is that there is a discrepancy between the target labels and the distribution of data points, further suggesting that some of the damaged component samples were misidentified as undamaged. Similar plateaus are also observable in the true positive rates, suggesting that some undamaged MLCC samples were erroneously labeled as damaged. As a result, it was decided that the X-ray and cross-section images were to be reinspected for samples misclassified by the OSVM. Two out of six samples labeled as negative showed small cracks, whereas only two out of seven samples labeled as positive could be reliably confirmed. However, because the sample reinspection was conducted based on the output of the OSVM, the reinspection results are not taken into account when reporting the final performance metrics for the OSVM. Fig. 6.2 shows the confusion matrices for the OSVM test results.

### 6.2.3 Comparison with binary classifiers

While some of the misclassifications by the OSVM were suspected to be due to mislabeled component samples, there was no method to reliably confirm which labels were false positives or false negatives. Instead, the OSVM was compared with four conventional binary classifiers: artificial neural network, binary support vector machine, random forest, and  $k$  nearest neighbor classifier (see section 5.2). The binary classifiers were trained using acoustic data from PCB before and after bending, i.e., the training data comprised damaged and undamaged examples. Although the same erroneously labeled samples would also corrupt the training set for the binary classifiers, the performance of the commonly used models could be used as a baseline for the OSVM. Because the binary classifiers could not be trained on a separate set of intact-only MLCCs, the evaluation was conducted using the leave-one-out cross-validation process.

As the one-class support vector machine was trained without any examples of acoustic signatures from damaged MLCCs, it would be reasonable to expect that the classification performance of the model would not match that of a binary classifier trained on both damaged and undamaged component samples. However, the ROC graphs in Fig. 6.4 show that the OSVM achieves a comparable performance in terms of AUC scores when using amplitude- and phase-based features. The binary classifiers were also trained using the same features, although this resulted in only a marginally better performance than using the full feature set.

The evaluation of the OSVM highlighted the importance of feature extraction and selection for obtaining the best possible performance. The results in Table 6.1 and Fig. 6.1 show that the role of feature selection is more pronounced than for the conventional binary classifiers, as discussed in section 5.2. Even though the sample size was limited, the results clearly show that the best classification results are obtained by omitting frequency-

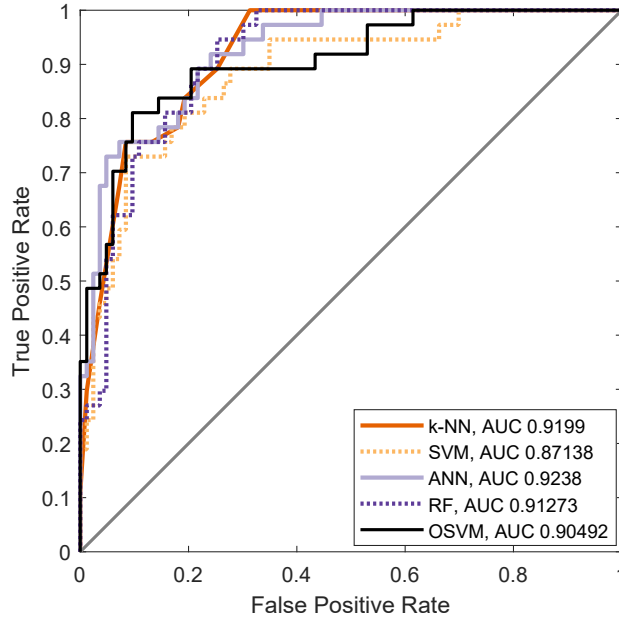


Figure 6.4. ROC graphs depicting the performance of four binary classifiers versus the one-class support vector machine. The classifiers were evaluated on data collected from PCB 1 both before and after the controlled bending procedure. The binary classifiers were evaluated using the leave-one-out cross-validation technique, whereas the OSVM was trained on a separate set of intact MLCCs and tested on the evaluation data.

based features. There is a possibility that the frequency of the resonance peaks does not carry significant amounts of information about small cracks or delaminations within the body of an MLCC, or that the changes to the resonance frequencies are overshadowed by intrinsic variations in resonance characteristics between components. Another explanation is that the feature extraction method used for calculating  $f_1$ ,  $f_2$ , and  $m_f$  loses much of the usable information contained within the frequency location of the resonance peaks, e.g., as a result of inaccuracies in determining the exact resonance frequency of the capacitor under test.



## 7 Conclusions and future research

Latent mechanical damage in MLCCs remains an open problem, especially if the electrical operation of the component is initially unaffected. While there are imaging methods such as ultrasound and X-ray capable of revealing cracks and delamination within the ceramic body of an MLCC, none can be considered suitable for a full assembly line environment because of their slow speed or other limitations.

This dissertation demonstrated a new nondestructive testing method for multilayer ceramic capacitors. Based on the measurement of acoustic emissions from MLCCs under electrical excitation, the method can be applied on soldered capacitors, making it a potential tool for quality assurance applications on an assembly line.

The main components, i.e., acoustic measurement technique, signal processing, and classification techniques were presented in **Publications I–III**, showing that the proposed method can be used for discovering different types of latent mechanical damage in soldered MLCCs. One-class-based classification of MLCC acoustic data was also presented, making the NDT technique significantly more suitable for the assembly line usage.

The main advantages of the proposed NDT method are speed and capability of detecting various types of mechanical damage. Conventional X-ray imaging can be used for rapid screening of numerous components, but the images have to be interpreted, and the ability of detecting cracks within the dielectric material depends heavily on the imaging angle. Three-dimensional X-ray tomography can alleviate the latter challenge, but the imaging can take dozens of minutes per component sample (Andersson et al., 2016), and delamination between internal electrodes can be difficult to observe when the component is not experiencing mechanical strain. On the other hand, ultrasound techniques such as CSAM can fail in detecting cracks underneath the end terminations of an MLCC and require submerging the component in water, making the method unsuitable for assembly line testing. The measurement hardware is also significantly less complex than, e.g., 3D X-ray imaging equipment, and the piezoelectric transducer could probably be integrated into an automatically actuated system, such as a pick-and-place machine.

Electrical testing methods similar to the proposed NDT method have been proposed, such as the radio frequency testing technique by Bechou et al. (1996). However, if other reactive components are placed on the same current path as the MLCC-DUT, identifying

damage within the capacitor may be difficult as the impedance behavior is altered. Measuring multiple MLCCs placed in parallel would also be challenging, as each component would return a signal response. On the other hand, the proposed NDT method could be applied to MLCCs with other reactive components in series or parallel, given that the excitation signal source can provide enough current throughout the frequency range during the measurement. The feature extraction and machine learning related techniques developed for the proposed NDT method could also be applicable to the electromechanical testing method proposed by Bechou et al. (1996).

The electrical excitation signal required to generate the acoustic signal is likely to limit the proposed method to MLCCs with a voltage rating of 10 V or higher. Another evident limiting factor is the voltage handling ability of other components parallel to the MLCC-DUT, which may exclude the use of the method to, e.g., power filter capacitors for microcontrollers or other integrated circuits. Thus, in order to apply the proposed method in assembly line testing, the PCB assembly being tested should be designed in a way that allows to apply the excitation signal to the MLCCs. As an alternative, the use of mechanical impedance analysis probes could be investigated.

The physical size of the component can also limit the applicability of the method, because the fundamental resonant frequency of the ceramic body is inversely proportional to the size of the component. However, past research suggests that flex cracking affects mainly components with larger case sizes, such as 1812 and up (Keimasi et al., 2008). Damage from uneven thermal expansion, caused by manual soldering, is also likely to affect case sizes that are physically large enough to be soldered manually. All things considered, the proposed method is probably best applied on power electronics devices containing relatively large MLCCs, which are also more prone to mechanical damage.

## 7.1 Future work

Although the proposed NDT method was shown to be able to discover latent mechanical damage within MLCCs, many aspects of the method can be improved. Starting from the measurement hardware, the shielding of the piezoelectric transducer and data acquisition equipment could be improved. The amount of EMI from the excitation signal source could also be reduced by optimizing the shielding and wiring geometry. However, some of the noise from the signal source is probably unavoidable, because the excitation signal propagates via the PCB traces, which may not be designed for megahertz frequencies.

The point contact sensor used in this work was a common-purpose broadband transducer, equipped with M14 threads for mounting. As such, the physical footprint of the sensor was relatively large compared with the PCB layout. An assembly line environment would require a sensor with slimmer housing, which would facilitate measurements on PCBs with a tight component layout. As an alternative, the use of an acoustic waveguide

mounted onto the transducer has been studied by Tarula (2017), which, however, was observed to significantly distort the acoustic signal.

With better shielding, windowed lowpass filtering could suffice for denoising the acoustic signals, making wavelet-based filtering redundant. However, the acoustic responses from individual components will still very likely differ from each other because of slight variations within the structure of the components and the solder joints. Therefore, the feature extraction techniques should be improved to better facilitate discrimination between damaged and undamaged samples. For example, the full width at the half maximum of each resonance peak could provide additional information about the condition of the component, and the use of phase information could also be further investigated. With a larger set of data, the use of deep learning approaches, such as convolutional neural networks, could have an advantage over manual feature extraction, as they have been successfully applied to similar problems (Fawaz et al., 2019). For example, convolutional autoencoders could allow for constructing an improved feature set while remaining in the single-class classification domain.

While the use of the OSVM classifier was successfully demonstrated in conjunction with the Cliffhanger algorithm, other methods such as binary classifiers yield an equally good performance. The results indeed suggested that the classification performance was ultimately limited by the accuracy of the labeling process. While the use of a one-class classifier circumvents this issue in terms of training data, testing and evaluation of any classifier will require labeled examples of damaged MLCCs. However, by using a one-class classifier such as the OSVM, the process of data collection becomes less laborious, as damaged component samples are required only for evaluating the performance of the classifier.

In addition to the aforementioned technical improvements, the proposed NDT method needs more extensive testing before it can be applied to the assembly line use. While there is no fundamental reason to believe that the method would not work on other case sizes than the 2220 investigated in this dissertation, the method should still be evaluated on other commonly used case sizes that are large enough to be vulnerable to, e.g., flex cracking. Initial tests showed that the magnitude of the acoustic response varied significantly between the four case sizes inspected, which might result in either better or worse performance figures. Finally, the method should be field tested with actual production line PCB assemblies, taking into account factors such as parallel components and restrictions to the excitation signal placed by other components.



## References

- Adams, T. (2009), "Preventing MLCC failures," *Circuits Assembly*, URL <https://www.circuitsassembly.com/ca/editorial/menu-features/296-current-articles/17452-preventing-mlcc-failures.html>.
- Ahmar, J.A. and Wiese, S. (2015), "A finite element modelling and fracture mechanical approach of multilayer ceramic capacitors," in *16th International Conference on Thermal, Mechanical and Multi-Physics Simulation and Experiments in Microelectronics and Microsystems*, URL <https://doi.org/10.1109/EuroSimE.2015.7103147>.
- Anaissi, A., Khoa, N.L.D., and Wang, Y. (2018), "Automated parameter tuning in one-class support vector machine: an application for damage detection," *International Journal of Data Science and Analytics*, vol. 6, p. 311–325, URL <https://doi.org/10.1007/s41060-018-0151-9>.
- Andersson, C., Ingman, J., Varescon, E., and Kiviniemi, M. (2016), "Detection of cracks in multilayer ceramic capacitors by x-ray imaging," *Microelectronics Reliability*, vol. 64, pp. 352–356, URL <https://doi.org/10.1016/j.microrel.2016.07.110>.
- Bechou, L., Mejdí, S., Ousten, Y., and Danto, Y. (1996), "Non-destructive detection and localization of defects in multilayer ceramic chip capacitors using electromechanical resonances," *Quality and reliability engineering international*, vol. 12, no. 1, pp. 43–53, URL [doi.org/10.1002/\(SICI\)1099-1638\(199601\)12:1<43::AID-QRE981>3.0.CO;2-O](https://doi.org/10.1002/(SICI)1099-1638(199601)12:1<43::AID-QRE981>3.0.CO;2-O).
- Bescup, J. (2016), "High-voltage capacitor failure on a downhole oilfield pcb," *Electronic Device Failure Analysis*, vol. 18, no. 3, pp. 4–8, URL <https://www.asminternational.org/documents/10192/26738819/EDFA1803p04.pdf/cfba9ac7-3907-4897-8541-27874777d92c/26775889>.
- Boser, B.E., Guyon, I.M., and Vapnik, V.N. (1992), "A training algorithm for optimal margin classifiers," in *Proceedings of the Fifth Annual Workshop on Computational Learning Theory, COLT '92*, pp. 144–152, ACM, New York, NY, USA, URL <http://doi.acm.org/10.1145/130385.130401>.
- Bounsiar, A. and Madden, M.G. (2014), "Kernels for one-class support vector machines," in *2014 International Conference on Information Science Applications (ICISA)*, pp. 1–4, URL <https://doi.org/10.1109/ICISA.2014.6847419>.



- Breiman, L. (2001), “Random forests,” *Machine Learning*, vol. 45, no. 1, pp. 5–32, URL <https://doi.org/10.1023/A:1010933404324>.
- Brown, D. (2018), “Oxygen vacancy migration in mlccs,” in *2018 Pan Pacific Microelectronics Symposium (Pan Pacific)*, pp. 1–6, URL <https://doi.org/10.23919/PanPacific.2018.8319004>.
- Carbone, J. (2018), “Expect Near-Term MLCC Shortages, Higher Prices,” techreport, Informa USA, Inc., URL <https://www.sourcetoday.com/supply-chain/expect-near-term-mlcc-shortages-higher-prices>, accessed: 2019-02-22.
- Chan, Y.C., Yeung, F., Jin, G., Bao, N., and Chung, P.S. (1995), “Nondestructive detection of defects in miniaturized multilayer ceramic capacitors using digital speckle correlation techniques,” *IEEE Transactions on Components, Packaging, and Manufacturing Technology Part A*, vol. 18, no. 3, pp. 677–684, URL <https://doi.org/10.1109/95.465169>.
- Chan, Y., Hung, K.C., and Dai, X. (2000), “Nondestructive defect detection method in multilayer ceramic capacitors using an improved digital speckle correlation method with wavelet packet noise reduction processing,” *IEEE Transactions on Advanced Packaging*, vol. 23, no. 1, pp. 80–87, URL <https://doi.org/10.1109/6040.826765>.
- Chen, J. and Feng, Z. (2014), “X7R dielectric multilayer ceramic capacitors show good micro-actuating properties with little hysteresis,” *Electronics Letter*, vol. 50, no. 7, pp. 538–540, URL <https://doi.org/10.1049/el.2013.3815>.
- Chicco, D. and Jurman, G. (2020), “The advantages of the matthews correlation coefficient (mcc) over f1 score and accuracy in binary classification evaluation,” *BMC Genomics*, vol. 21, no. 6, URL <https://doi.org/10.1186/s12864-019-6413-7>.
- Consumer Reports (2006), “Product reliability survey,” research report, Consumer Reports National Research Center.
- Consumer Reports (2011), “Repair or replace it?” *Consumer Reports*, pp. 1–7, URL <http://www.diy.repairclinic.com/wp-content/uploads/2011/09/8-1-11-Consumer-Reports.pdf>.
- Cortes, C. and Vapnik, V. (1995), “Support-vector networks,” *Machine Learning*, vol. 20, no. 3, pp. 273–297, URL <https://doi.org/10.1007/BF00994018>.
- Das, S., Srivastava, A.N., and Chattopadhyay, A. (2007), “Classification of damage signatures in composite plates using one-class svms,” in *2007 IEEE Aerospace Conference*, pp. 1–19, URL <https://doi.org/10.1109/AERO.2007.352912>.
- Dougherty, G. (2013), *Pattern Recognition and Classification: An Introduction*, Springer, 1st edn.

- Dua, D. and Graff, C. (2017), “UCI machine learning repository,” URL <http://archive.ics.uci.edu/ml>.
- Erdahl, D.S. and Ume, I.C. (2004), “Online-offline laser ultrasonic quality inspection tool for multilayer ceramic capacitors-part i,” *IEEE Transactions on Advanced Packaging*, vol. 27, no. 4, pp. 647–653, URL <https://doi.org/10.1109/TADVP.2004.831823>.
- Erdahl, D.S. and Ume, I.C. (2005), “Online-offline laser ultrasonic quality inspection tool for multilayer ceramic capacitors-part ii,” *IEEE Transactions on Advanced Packaging*, vol. 28, no. 2, pp. 264–272, URL <https://doi.org/10.1109/TADVP.2005.846934>.
- Fawaz, H.I., Forestier, G., Weber, J., Idoumghar, L., and Muller, P.A. (2019), “Deep learning for time series classification: a review,” *Data Mining and Knowledge Discovery*, vol. 33, pp. 917–963, URL <https://doi.org/10.1007/s10618-019-00619-1>.
- Fawcett, T. (2004), “Roc graphs: Notes and practical considerations for researchers,” Tech. rep., HP Laboratories, URL <https://www.hpl.hp.com/techreports/2003/HPL-2003-4.pdf>.
- Goodfellow, I., Bengio, Y., and Courville, A. (2016), *Deep Learning*, MIT Press, <http://www.deeplearningbook.org>.
- Hahn, R., Randall, M., and Paulsen, J. (2007), “The battle for maximum volumetric efficiency - part 1: When technologies compete, customers win,” in *CARTS Europe 2007 Symposium*, pp. 53–73, URL <https://sh.kemet.com/Lists/TechnicalArticles/Attachments/58/2007%20CARTS-Europe%20The%20Battle%20for%20Max%20CV%20-%20Part%201.pdf>.
- Ho, J., Jow, T.R., and Boggs, S. (2010), “Historical introduction to capacitor technology,” *IEEE Electrical Insulation Magazine*, vol. 26, no. 1, pp. 20–25, URL <https://doi.org/10.1109/MEI.2010.5383924>.
- Ho, T.K. (1995), “Random decision forests,” in *Proceedings of 3rd International Conference on Document Analysis and Recognition*, vol. 1, pp. 278–282 vol.1, URL <https://doi.org/10.1109/ICDAR.1995.598994>.
- IEC 60384-1:2016 (2016), “Fixed capacitors for use in electronic equipment – Part 1: Generic specification,” Standard, International Electrotechnical Commission.
- Ingman, J., Jormanainen, J., Vulli, A., Ingman, J., Maula, K., Kärkkäinen, T.J., and Silventoinen, P. (2019), “Localization of dielectric breakdown defects in multilayer ceramic capacitors using 3d x-ray imaging,” *Journal of the European Ceramic Society*, vol. 39, no. 4, pp. 1178 – 1185, URL <https://doi.org/https://doi.org/10.1016/j.jeurceramsoc.2018.10.030>.
- IRENA (2021), *World Energy Transition Outlook: 1.5 °C pathway*, International Renewable Energy Agency, Abu Dhabi, URL <https://irena.org/>

/media/Files/IRENA/Agency/Publication/2021/Jun/IRENA\_World\_Energy\_Transitions\_Outlook\_2021.pdf.

- Jacob, P. (2016), “Early life field failures in modern automotive electronics – an overview; root causes and precautions,” *Microelectronics Reliability*, vol. 64, pp. 79–83, URL <https://www.sciencedirect.com/science/article/pii/S0026271416301573>, proceedings of the 27th European Symposium on Reliability of Electron Devices, Failure Physics and Analysis.
- James, S.B. (2018), “Shortage of tiny capacitors creates big worries for tech, cable industries,” *SNL Kagan Media & Communications Report*, URL <https://www.spglobal.com/marketintelligence/en/news-insights/trending/voksabc0yixvacbsquyyww2>, accessed: 2019-02-22.
- Johnson, W.I., Herzberger, J.L., Kim, S.A., Peterson, K.L., Heyliger, P.R., and White, G.S. (2017), “Resonant acoustic frequency shifts associated with cracks in multilayer ceramic capacitors,” *IEEE Transactions on Device and Materials Reliability*, vol. 17, no. 2, pp. 316–323, URL <https://doi.org/10.1109/TDMR.2017.2682818>.
- Johnson, W.L., Kim, S.A., White, G.S., and Herzberger, J. (2014), “Nonlinear resonant acoustic detection of cracks in multilayer ceramic capacitors,” in *2014 IEEE International Ultrasonics Symposium*, pp. 244–247, URL <https://doi.org/10.1109/ULTSYM.2014.0062>.
- Kahn, S.R. and Checkaneck, R.W. (1983), “Acoustic emission testing of multilayer ceramic capacitors,” *IEEE Transactions on Components, Hybrids and Manufacturing Technology*, vol. 6, no. 4, pp. 517–526, URL <https://doi.org/10.1109/TCHMT.1983.1136222>.
- Keimasi, M., Azarian, M.H., and Pecht, M.G. (2008), “Flex cracking of multilayer ceramic capacitors assembled with pb-free and tin-lead solders,” *IEEE Transactions on Device and Materials Reliability*, vol. 8, no. 1, pp. 182–192, URL <https://doi.org/10.1109/TDMR.2007.912256>.
- Kemet Electronics Corporation (2020), “Here’s what makes mlcc dielectrics different,” Online, URL <https://ec.kemet.com/blog/mlcc-dielectric-differences/>.
- Kieran, G.F. (1981), “A comparison of screening techniques for ceramic capacitors,” in *Symposium on Capacitor Technologies, Applications and Reliability*, pp. 111–119, URL <https://ntrs.nasa.gov/api/citations/19810017835/downloads/19810017835.pdf>.
- Ko, B.H., Jeong, S.G., Ahn, Y.G., Park, K.S., Park, N.C., and Park, Y.P. (2014), “Analysis of the correlation between acoustic noise and vibration generated by a multi-layer ceramic capacitor,” *Microsystem Technologies*, vol. 20, no. 8, pp. 1671–1677, URL <https://doi.org/10.1007/s00542-014-2209-5>.

- Kohonen, T. (1982), “Self-organized formation of topologically correct feature maps,” *Biological Cybernetics*, vol. 43, pp. 59–69, URL <https://doi.org/10.1007/BF00337288>.
- KRN Services (2014), *AMP-1BB-J Broadband Preamplifier Datasheet*, URL <http://www.krnservices.com/documents/amp-1bb-j-5-20-14.pdf>.
- KRN Services (2015), *KRNBB-Pc Point Contact Sensor Datasheet*, URL [http://www.krnservices.com/documents/bbpc\\_flyer\\_4-13-15.pdf](http://www.krnservices.com/documents/bbpc_flyer_4-13-15.pdf).
- Kumar, V., Behera, R.K., Joshi, D., and Bansal, R. (2020), *Power Electronics, Drives and Advanced Applications*, Taylor & Francis Group.
- Lambert, L. (2014), “Damage prevention when soldering ceramic chip capacitors,” Tech. rep., URL [https://www.eptac.com/wp-content/uploads/2014/09/eptac\\_09\\_17\\_14.pdf](https://www.eptac.com/wp-content/uploads/2014/09/eptac_09_17_14.pdf), online.
- Lawrence, A. and Ascierio, R. (2018), “Is 99.99 an industry myth? uptime institute shows outages are common and costly,” Tech. rep., 451 Research, LLC, URL [https://info.sunbirdcim.com/hubfs/451\\_Reprint\\_Is99AnIndustryMyth\\_6AUG2018.pdf](https://info.sunbirdcim.com/hubfs/451_Reprint_Is99AnIndustryMyth_6AUG2018.pdf).
- Lee, T. and Aksay, I.A. (2001), “Hierarchical structure - ferroelectricity relationships of barium titanate particles,” *Crystal Growth & Design*, vol. 1, no. 5, pp. 401–419, URL <https://doi.org/10.1021/cg010012b>.
- Levikari, S., Kärkkäinen, T.J., Andersson, C., Tamminen, J., and Silventoinen, P. (2018), “Acoustic Phenomena in Damaged Ceramic Capacitors,” *IEEE Transactions on Industrial Electronics*, vol. 65, no. 1, pp. 570–577, URL <https://doi.org/10.1109/TIE.2017.2714123>.
- Liu, F.T., Ting, K.M., and Zhou, Z. (2008), “Isolation forest,” in *2008 Eighth IEEE International Conference on Data Mining*, pp. 413–422, URL <https://doi.org/10.1109/ICDM.2008.17>.
- van der Maaten, L. and Hinton, G. (2008), “Visualizing data using t-sne,” *Journal of Machine Learning Research*, vol. 9, URL <http://jmlr.org/papers/volume9/vandermaaten08a/vandermaaten08a.pdf>.
- Manning, C.D., Raghavan, P., and Schütze, H. (2012), *Introduction to Information Retrieval*, Cambridge University Press, URL <https://nlp.stanford.edu/IR-book/>.
- Medtronic (2019), “Potential for no output/no telemetry condition in subset of ipg and crt-p products due to ceramic capacitor leakage pathway,” Tech. rep., Medtronic, Inc.
- Mehta, P., Bukov, M., Wang, C.H., Day, A.G., Richardson, C., Fisher, C.K., and Schwab, D.J. (2019), “A high-bias, low-variance introduction to machine learning for physicists,” *Physics Reports*, vol. 810, pp. 1–124, URL <https://www.sciencedirect.com/science/article/pii/S0370157319300766>.

- Mellor, A., Boukir, S., Haywood, A., and Jones, S. (2015), “Exploring issues of training data imbalance and mislabelling on random forest performance for large area land cover classification using the ensemble margin,” *ISPRS Journal of Photogrammetry and Remote Sensing*, vol. 105, pp. 155 – 168, URL <https://doi.org/10.1016/j.isprsjprs.2015.03.014>.
- Mohan, N., Underland, T.M., and Robbins, W.P. (2003), *Power Electronics — Converters, Applications, and Design*, John Wiley & Sons, 3 edn.
- Mun, B., Lim, M., and Bae, S. (2020), “Condition monitoring scheme via one-class support vector machine and multivariate control charts,” *Journal of Mechanical Science and Technology*, vol. 43, pp. 3937–3944, URL <https://doi.org/10.1007/s12206-020-2203-z>.
- Ousten, Y., Mejdí, S., Bechou, L., Tregon, B., and Danto, Y. (1998), “Comparison between piezoelectric method and ultrasonic signal analysis for crack detection in type II multilayer ceramic capacitors,” *Quality and reliability engineering international*, vol. 14, no. 2, URL [https://doi.org/10.1002/\(SICI\)1099-1638\(199803/04\)14:2<91::AID-QRE167>3.0.CO;2-7](https://doi.org/10.1002/(SICI)1099-1638(199803/04)14:2<91::AID-QRE167>3.0.CO;2-7).
- Pearson, K. (1901), “On lines and planes of closest fit to systems of points in space,” *The London, Edinburgh, and Dublin Philosophical Magazine and Journal of Science*, vol. 2, no. 11, pp. 559–572, URL <https://doi.org/10.1080/14786440109462720>.
- Ponemon Institute (2016), “Cost of data center outages,” Tech. rep., Ponemon institute, LLC, URL [https://www.vertiv.com/globalassets/documents/reports/2016-cost-of-data-center-outages-11-11\\_51190\\_1.pdf](https://www.vertiv.com/globalassets/documents/reports/2016-cost-of-data-center-outages-11-11_51190_1.pdf).
- Randoll, R., Wondrak, W., and Schletz, A. (2016), “Lifetime and manufacturability of integrated power electronics,” *Microelectronics Reliability*, vol. 64, pp. 513 – 518, URL <https://doi.org/10.1016/j.microrel.2016.07.032>, proceedings of the 27th European Symposium on Reliability of Electron Devices, Failure Physics and Analysis.
- Rumelhart, D.E., Hinton, G.E., and Williams, R.J. (1988), “Learning representations by back-propagating errors,” in J.A. Anderson and E. Rosenfeld (eds.), *Neurocomputing: Foundations of Research*, pp. 696–699, MIT Press, Cambridge, MA, USA, URL <http://dl.acm.org/citation.cfm?id=65669.104451>.
- Russell, S. and Norvig, P. (2009), *Artificial Intelligence: A Modern Approach*, Prentice Hall Press, Upper Saddle River, NJ, USA, 3rd edn.
- Schmidhuber, J. (2015), “Deep learning in neural networks: An overview,” *Neural Networks*, vol. 61, pp. 85 – 117, URL <https://doi.org/10.1016/j.neunet.2014.09.003>.

- Schölkopf, B., Platt, J.C., Shawe-Taylor, J., Smola, A.J., and Williamson, R.C. (2001), “Estimating the support of a high-dimensional distribution,” *Neural Computation*, vol. 13, no. 7, pp. 1443–1471, URL <https://doi.org/10.1162/089976601750264965>.
- Skelly, A. and Waugh, M.D. (2009), “Understanding dc bias characteristics in high-capacitance mlccs,” *Ceramic Industry Magazine*, vol. 159, no. 8, pp. 16 – 18, URL <https://www.ceramicindustry.com/articles/90304-understanding-dc-bias-characteristics-in-high-capacitance-mlccs/>.
- Sood, B. (2013), “Root cause failure analysis of electronics,” URL [https://www.academia.edu/24067725/Root\\_Cause\\_Failure\\_Analysis\\_of\\_Electronics\\_SMTA\\_Philadelphia\\_March\\_14\\_2013](https://www.academia.edu/24067725/Root_Cause_Failure_Analysis_of_Electronics_SMTA_Philadelphia_March_14_2013), online.
- Tarula, J. (2017), “An acoustic screening system for multilayer ceramic capacitors – a prototype,” URL <http://urn.fi/URN:NBN:fi-fe2017121155588>.
- Teverovsky, A. (2012), “Guidelines for selection, screening and qualification of low-voltage commercial multilayer ceramic capacitors for space programs,” techreport, NASA, URL <https://nepp.nasa.gov/files/23923/Guidelines%20for%20selection%20of%20MLCCs%20rev.A.pdf>.
- Teverovsky, A. (2018), “Cracking problems in low-voltage chip ceramic capacitors,” techreport GSFC-E-DAA-TN65668, NASA, URL <https://ntrs.nasa.gov/archive/nasa/casi.ntrs.nasa.gov/20190001592.pdf>.
- Unnthorsson, R., Runarsson, R.T., and Johnson, T.M. (2003), “Model selection in one class nu-svm using rbf kernels,” in *16th conference on Condition Monitoring and Diagnostic Engineering Management*, URL <https://web.archive.org/web/20070207080622/http://www.hi.is/~runson/svm/paper.pdf>.
- U.S. Department of Defense (1988), *Electronic Reliability Design Handbook*.
- Wallosek, I. (2020), “The possible reason for crashes and instabilities of the nvidia geforce rtx 3080 and rtx 3090 | investigative,” Tech. rep., URL <https://www.igorslab.de/en/what-real-what-can-be-investigative-within-the-crashes-and-instabilities-of-the-force-rtx-3080-andrtx-3090/>.
- Wang, S., Liu, Q., Zhu, E., Porikli, F., and Yin, J. (2018), “Hyperparameter selection of one-class support vector machine by self-adaptive data shifting,” *Pattern Recognition*, vol. 74, pp. 198 – 211, URL <https://doi.org/10.1016/j.patcog.2017.09.012>.
- Wang, X., Cheng, W., Chan, H., and Choy, C. (2003), “H<sub>2</sub>O-induced degradation in TiO<sub>2</sub>-based ceramic capacitors,” *Materials Letters*, vol. 57, no. 28, pp. 4351–4355, URL [https://doi.org/10.1016/S0167-577X\(03\)00275-1](https://doi.org/10.1016/S0167-577X(03)00275-1).

- Xiao, Y., Wang, H., and Xu, W. (2015), “Parameter selection of gaussian kernel for one-class svm,” *IEEE Transactions on Cybernetics*, vol. 45, no. 5, pp. 941–953, URL <https://doi.org/10.1109/TCYB.2014.2340433>.
- Yan, K., Ji, Z., and Shen, W. (2017), “Online fault detection methods for chillers combining extended kalman filter and recursive one-class svm,” *Neurocomputing*, vol. 228, pp. 205–212, URL <https://doi.org/10.1016/j.neucom.2016.09.076>.
- Yang, J. (2005), *An Introduction to the Theory of Piezoelectricity*, Springer.
- Zogbi, D.M. (2018), “MLCC Shortages by Case Size: 2018,” techreport, tti Inc., URL <https://www.ttiinc.com/content/ttiinc/en/resources/marketeye/categories/passives/me-zogbi-20180930.html>, accessed: 2019-02-22.

## **Publication I**

Levikari S., Kärkkäinen T., Andersson C., Tamminen J., and Silventoinen P.  
**Acoustic Phenomena in Damaged Ceramic Capacitors**

Reprinted with permission from  
*IEEE Transactions on Industrial Electronics*  
Vol. 65, Iss. 1, January 2018, pp. 570–577  
© 2017, IEEE





# Acoustic Phenomena in Damaged Ceramic Capacitors

Saku Levikari, Tommi J. Kärkkäinen, *Member, IEEE*, Caroline Andersson, *Member, IEEE*,  
Juha Tamminen, and Pertti Silventoinen, *Member, IEEE*

**Abstract**—Multilayer Ceramic Capacitors are prone to mechanical defects and damage because of the fragility of the ceramic dielectric. Because these faults are often not recognized by visual or electrical inspection, a non-destructive, fast way of detecting these defects would be very useful. Ceramic capacitors are known to generate acoustic emissions, caused by mechanical vibration of the capacitor body. Physical defects alter the mechanical properties of the capacitor, which, in turn, affect the acoustic signature of the capacitor. In this paper, acoustic information is acquired directly from both pristine and damaged capacitors. An experiment was conducted where capacitors were driven with a voltage chirp over a wide range of frequencies, and subsequent acoustic emissions were measured with a piezoelectric point contact sensor. Test boards were bent to cause flex cracks to the soldered capacitors, which were measured acoustically before and after bending. A comparison of these measurements showed that PCB bending causes characteristic changes to the capacitor acoustic response, which can be correlated with the resulted damage.

**Index Terms**—Acoustic emission, Ceramic capacitors, Nondestructive testing

## I. INTRODUCTION

MULTILAYER Ceramic Capacitors (MLCCs) are widely used in the electronics industry because of their high capacitance per volume and favorable electrical characteristics [1]. The ceramic dielectric yields high permittivity, but also makes the MLCCs prone to cracks.

Typical defects in MLCCs are voids and delaminations, often related to thermal stresses during manufacturing [2], [3]. Flex cracks [4] (see Fig. 1) are another typical defect, often resulting from mechanical force exerted on the capacitor during circuit board handling or assembly [5], [6]. A cracked capacitor is often not recognized during the production or assembly, as it may operate normally, and defects cannot be detected by visual inspection. In the field, however, the crack may shorten the lifespan of the capacitor, reduce the capacitance, or cause a total failure of the component (an

open or short contact) [7]. Hence, there is a need for detecting these defects before the product is delivered to the customer. Mechanical microsectioning [8] and chemical etching [9] are destructive methods for accurate defect detection in MLCCs, the former being the more usual method. Acoustic microscopy [6] is a commonly used nondestructive method; other studied techniques include acoustic emission stimulation using a mechanical ram [7], impedance analysis under DC bias (measurement of electromechanical resonances) [10], phase analysis using tone-burst excitation [11], leakage current monitoring [12], laser speckle pattern analysis [13], opto-acoustic microscopy [14], and neutron radiography [15]. Recently, an X-ray imaging method with sufficient accuracy for reliable detection of flex cracks was demonstrated [16]. Krieger *et al.* used an audio range microphone to detect acoustic emissions caused by an MLCC on a PCB, and observed differences between the signatures of intact and cracked capacitors [12]. Ko *et al.* showed that the fundamental resonant frequencies of a typical MLCC are in the order of 1 MHz [1], and hence, cannot be observed directly using an audio-range microphone. Erdahl and Ume used laser interferometry to detect changes in the vibrations of an MLCC, observing an amplitude increase in damaged capacitors [17], [18].

Later on, amplitude increases [19] and frequency shifts [20] in MLCC acoustic resonances have been observed using Resonant Ultrasound Spectroscopy. The interest in acoustic methods is explained by the fact that they are quick to apply and nondestructive for the capacitors. Therefore, they could potentially be further refined into a production line screening method. Other known methods, such as capacitance or leakage current monitoring, are based on detecting anomalies in the electrical operation of the capacitor; the acoustic method does not need leakage current, as mechanical defects can be detected even if the electrical operation of the capacitor is normal. The earlier work on acoustic phenomena of other electronic components, especially for the condition monitoring of power semiconductor modules [21]–[24], has also yielded important results on acoustic inspection and analysis methods.

Krieger *et al.* did their work on MLCCs that were soldered on a printed circuit board [12]. The vibrations were induced in the capacitors by an electrical frequency sweep signal applied to them. The vibration measurements were not carried out directly on the capacitors. Johnson *et al.* [19], [20] conducted their measurements directly on the capacitors, but the capacitors were not assembled on a circuit board. It can be argued that the experimental setup of Krieger *et al.*

Manuscript received December 20, 2016; revised April 21, 2017; accepted May 12, 2017.

Saku Levikari, Tommi J. Kärkkäinen and Pertti Silventoinen are with LUT School of Energy Systems, Lappeenranta University of Technology (LUT), Lappeenranta, Finland. Corresponding author: Saku Levikari, tel. +358 294 462 111, e-mail: saku.levikari@lut.fi.

Caroline Andersson is with ABB Corporate Research Center, Baden-Dättwil, Switzerland.

Juha Tamminen is with ABB Drives, Helsinki, Finland.

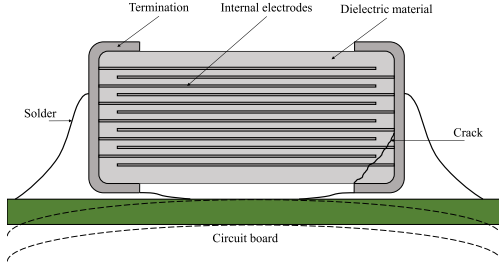


Fig. 1. Structure of a typical Multilayer Ceramic Capacitor with a crack in the dielectric material cutting a part of the inner electrodes. The capacitor is depicted at a  $0^\circ$  orientation, relative to the circuit board bending (dashed line).

has more resemblance to a production testing environment, but the measurements performed by Johnson *et al.* provide a better acoustic representation of the capacitor itself. In this study, vibrations are measured directly from capacitors that are soldered onto a PCB, and the vibrations are induced by an electrical signal applied to the capacitor.

In the present study, MLCCs were driven with pulse wave frequency sweeps to excite acoustic emissions, which were measured directly from the component using a piezoelectric point contact sensor. First, reference measurements were made for intact capacitors, after which the PCBs were bent once to induce flex cracks to the capacitors. The same capacitors were then remeasured, and the acoustic signatures were compared with the prebending data. The capacitors were also X-ray imaged after bending to verify the presence or absence of cracks. A portion of the capacitors was also cross-sectioned and inspected with an optical microscope in order to detect small cracks and delaminations.

The results show that bending the PCB and the subsequent damage to the MLCC alters the acoustic response of the capacitors. The changes in the acoustic behavior are more significant in capacitors that are damaged than in those that remain intact. The paper also presents conclusions on how the acoustic research of MLCCs could be done in the future. New experiments and research questions are proposed.

## II. ACOUSTIC EMISSION GENERATION IN MLCCs

Acoustic emission generation in MLCCs is a well-known phenomenon [1]. It is caused by piezoelectric behavior of barium titanate ( $\text{BaTiO}_3$ ), which is a typical dielectric material in type II MLCCs [25], [26]. When subjected to AC voltage, an MLCC starts to vibrate, and the vibration amplitude is greater near the resonance frequencies of the MLCC body. Ko *et al.* performed a modal analysis for a typical MLCC, for which the first four modes were found at 1.46, 1.47, 1.48, and 2.27 MHz corresponding to out-of-plane, in-plane, torsional, and compressional vibration. As the MLCC is small and lacks audio range resonances, the capacitor itself cannot produce significant audible noise, which is caused as the circuit board starts to vibrate [1]. Therefore, acoustic emissions should be

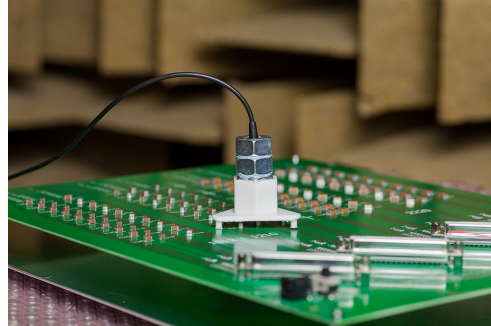


Fig. 2. KRN point contact sensor inside a 3D-printed fixture placed on top of an MLCC, with four hex nuts for additional weight.

measured directly from the component to bypass any effect of PCB resonances and sound damping caused by air. PCB-bending-related cracks, i.e. flex cracks, in the ceramic material of an MLCC decrease the stiffness of the component body. Thus, an amplitude increase in the resonance peaks can be considered a sign of damage or defect in the capacitor [17], [18].

## III. THE EXPERIMENT

The goal of the measurements was to observe mechanical vibrations and resonances of MLCCs directly from the components themselves with a point contact sensor. The capacitors were assembled on test boards, which were bent once to a selected strain level to induce flex cracks in the capacitors. The MLCCs were measured acoustically before and after bending, and the measurement data were processed in order to find bending-related differences.

### A. MLCCs and test board setup

MLCCs from three different manufacturers were used for the experiments. A total of 240 capacitors were tested, including both normal (or standard) and flexible (or soft) termination MLCCs, with case sizes 1206, 1210, 1812, and 2220. The capacitors were assembled on two test boards with specifications shown in Table I. The capacitors were assembled in 12 columns per board. Each column comprised 10 MLCCs with equivalent specifications as shown in Table II. The capacitor orientation is defined in Fig. 1.

### B. Measurement equipment

Acoustic emissions were measured from the top surface of the MLCCs using a KRN Services KRNBB-PC piezoelectric point contact sensor, which has a frequency range of up to 2.5 MHz. The sensor was attached to a 3D-printed fixture shown in Fig. 2, and the contact point was covered with Kapton tape to prevent shorting out of the capacitor. The sensor was connected to a Keysight InfiniiVision MSO-X 4104A oscilloscope through a KRN AMP-1BB-J preamplifier. The measurement setup was assembled in an anechoic room to minimize any external acoustic interference.

TABLE I  
TEST BOARD SPECIFICATIONS

Material	FR-4
Dimensions	39.0 cm by 30.4 cm
Thickness	1.55 mm
Copper layers	2
Coatings	None
Solder	SAC: 96.5Sn-3.0Ag-0.5Cu

### C. Experimental procedure

The MLCCs on the test boards were acoustically characterized by driving the capacitors with pulse wave frequency sweeps from 100 Hz to 2 MHz while measuring acoustic emissions. A pulse wave with an amplitude of  $\pm 10 V_{\text{peak}}$  and a duty cycle of 80% was used, as it yielded a higher acoustic response than a sine or square wave. A high duty cycle causes DC offset to the waveform, polarizing the ceramic dielectric and facilitating acoustic emission generation in MLCCs [12]. The duration of the sweep was set to 100 ms for a sufficiently high oscilloscope sampling rate.

The test boards were bent using a Zwick/Roell Z010 four-point bending setup, described in detail in [16]. The PCBs were subjected to an 18 mm bending displacement, corresponding to an average strain level of  $6000 \mu\text{Str}$ , with values ranging from 5800 to  $8000 \mu\text{Str}$ . The bending strain was measured at four positions at the centerline of the board, and it was higher at the edges of the board. After a single bending, the test boards were removed from the bending setup, and all the capacitors were examined by X-ray imaging to reveal cracks. Both end terminations of each MLCC were imaged at a  $70^\circ$  tilt angle using a Phoenix Nanomex X-ray machine. The X-ray imaging procedure is described in [16]. The same capacitors were then recharacterized acoustically without *a priori* information about the X-ray inspection results. Later, all the 120 capacitors on Test board 2 were cross-sectioned and polished, and then imaged using an optical microscope. For some of the MLCCs, the cross-sectioning was done to multiple depths. Because cross-sectioning is very laborious and therefore expensive, only one board was chosen for the procedure.

### D. Numerical comparison of acoustic signal envelopes

An algorithm for numerical comparison of MLCC acoustic responses was developed. The algorithm was based on obtaining an envelope curve of the measured acoustic signal. This method provides a smooth curve, which neglects phase differences between measurements while maintaining the amplitude information.

First, frequencies up to 40 kHz were cut off from the measured signal, because a high-amplitude burst occurred in this frequency range. The burst was caused by vibration of the PCB, and showed large variation in amplitude between measurements. The envelope  $e(t)$  was then calculated for each measured signal  $u(t)$  as

$$e(t) = \text{Downsample}_{N_{\text{DS}}} \left\{ \text{lpf} \left[ \sqrt{(u(t))^2 + \text{Re} \{ \mathcal{H}(u(t)) \}^2} \right] \right\} \quad (1)$$

TABLE II  
DETAILS OF MLCCs ON TEST BOARDS

	Column	Case (Normal/Flex)	$C$ ( $\mu\text{F}$ )	Orientation
Test board 1	<i>a</i>	1206 N	4.7	$0^\circ$
	<i>b</i>	1206 F	4.7	$0^\circ$
	<i>c</i>	1206 N	4.7	$45^\circ$
	<i>d</i>	1206 F	4.7	$45^\circ$
	<i>e</i>	1206 N	4.7	$90^\circ$
	<i>f</i>	1206 F	4.7	$90^\circ$
	<i>g</i>	1210 N	10	$0^\circ$
	<i>h</i>	1210 F	10	$0^\circ$
	<i>i</i>	1210 N	10	$45^\circ$
	<i>j</i>	1210 F	10	$45^\circ$
	<i>k</i>	1210 N	10	$90^\circ$
	<i>l</i>	1210 F	10	$90^\circ$
Test board 2	<i>a</i>	1812 N	22	$0^\circ$
	<i>b</i>	1210 F	10	$0^\circ$
	<i>c</i>	1812 N	22	$45^\circ$
	<i>d</i>	1210 F	10	$45^\circ$
	<i>e</i>	1812 N	22	$90^\circ$
	<i>f</i>	1210 F	10	$90^\circ$
	<i>g</i>	2220 N	22	$0^\circ$
	<i>h</i>	2220 F	22	$0^\circ$
	<i>i</i>	2220 N	22	$45^\circ$
	<i>j</i>	2220 F	22	$45^\circ$
	<i>k</i>	2220 N	22	$90^\circ$
	<i>l</i>	2220 F	22	$90^\circ$

All capacitors rated at 25 V.

where  $\mathcal{H}(u(t))$  is the Hilbert transform of the signal, lpf is a 2nd-order Butterworth-type lowpass filter with a cutoff frequency of 8 kHz, and  $N_{\text{DS}}$  is a downsampling factor of 80. Here,  $e$  and  $u$  are treated as vectors containing the discrete data points of the signals.

It was assumed that all the intact capacitors with equivalent specifications have a similar acoustic response, because the resonant frequencies of a capacitor depend on its physical dimensions and mechanical properties. Krieger *et al.* also observed that the acoustic spectra of defect-free capacitors are similar to each other [12], which supports our assumption. Therefore, a reference envelope for each capacitor column (Table II) was formed by calculating the mean and standard deviation of the prebending envelopes  $e$  in the column. Such a statistical approach was chosen because it minimizes the effect of outliers and provides information on the variation within the reference data.

It was observed that the amplitude of the envelope is dependent on the contact and downward force of the sensor. This dependence was modeled as

$$e = e_{\text{ref}}\theta + v, \quad (2)$$

where  $\theta \in \mathbb{R}_+$  depends on the mechanical contact between the sensor and the MLCC, and  $v$  is a zero-mean error vector. To reduce the variation caused by the mechanical contact, the mean reference envelope was fitted into each envelope of the examined MLCCs using the method of Generalized Least Squares (GLS):

$$\hat{\theta}_{\text{GLS}} = \left( e_{\text{ref}}^T W e_{\text{ref}} \right)^{-1} e_{\text{ref}}^T W e \quad (3)$$

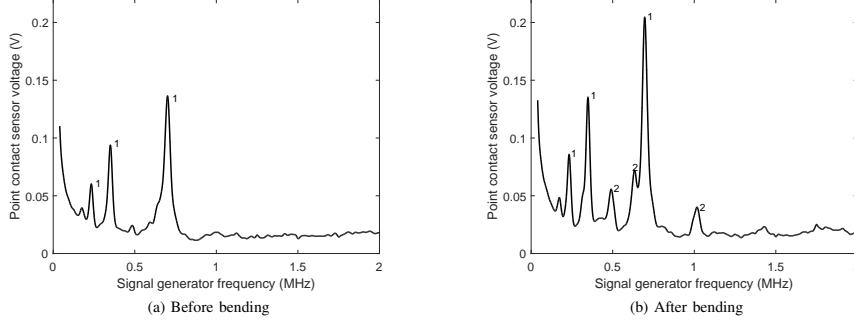


Fig. 3. Typical acoustic response of a 1812-size MLCC before (a) and after (b) a single PCB bending. The amplitude of the highest resonant peaks increases from 136 to 204 mV (+50%), and the peak shifts from 700.9 kHz to 696.4 kHz (-6.5%). The difference between 3a and 3b indicates that the mechanical properties of the capacitor body have been affected by test board bending.

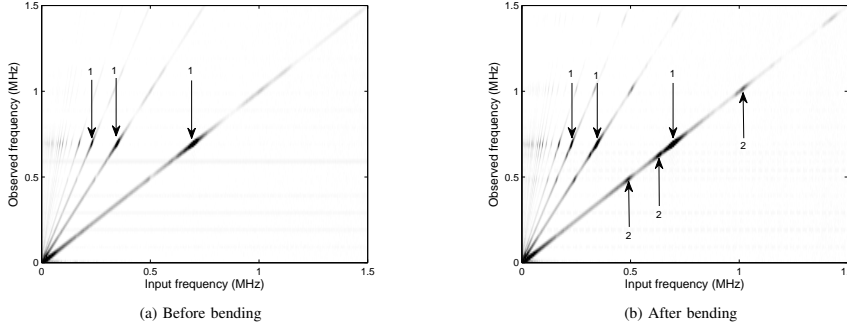


Fig. 4. Spectrograms of the acoustic responses in Fig. 3 before and after a single PCB bending. It is seen that the peaks indicated by "1" in Fig. 3 are different harmonics of one resonant mode, whereas peaks indicated by "2" are all individual resonant modes.

where the inverse variances  $\sigma_i^{-2}$  of the reference envelope were used as weights:

$$W = \text{diag} \left( \frac{1}{\sigma_1^2}, \dots, \frac{1}{\sigma_N^2} \right). \quad (4)$$

The difference value between the envelope  $e$  of the examined MLCC and the LS-fitted reference envelope  $\hat{e}_{\text{ref}} = e_{\text{ref}}\hat{\theta}$  was calculated as

$$L_{\text{GLS}} = \frac{\sum_{i=1}^N \frac{1}{\sigma_{\text{ref},i}^2} (e_i - \hat{e}_{\text{ref},i})^2}{N\mu_{L_{\text{GLS}},\text{ref}}}. \quad (5)$$

The equation above has been scaled with the number of data points  $N$  and the mean of  $L_{\text{GLS}}$  values of the intact capacitors in the column,  $\mu_{L_{\text{GLS}},\text{ref}}$ .

Thus, the value of  $L_{\text{GLS}} = 1$  corresponds to the reference envelope itself, and the  $L_{\text{GLS}}$  values for intact capacitors represent the difference between an individual reference MLCC and the mean of reference capacitors. Bending-related changes, such as new resonant peaks, cause an increase in the  $L_{\text{GLS}}$  values.

## IV. RESULTS

### A. Effects of PCB bending on acoustic responses

A typical acoustic response of an intact capacitor is shown in Fig. 3a, which depicts several peaks caused by the mechanical resonance of the capacitor body. Compared with the response of the same MLCC after suffering flex cracks from bending (Fig. 3b), two main features can be associated with the induced cracks: an amplitude increase of resonant peaks (indicated by "1") and emergence of new resonant peaks (indicated by "2"). Such features were typically not observed in uncracked capacitors. Alongside the amplitude increase, slight shift in acoustic resonant frequencies was also observed in many capacitors (see Fig. 3). These findings are very similar to those made by Johnson *et al.* [19], [20].

The harmonic components of the input signal cause resonant peaks of the capacitor to appear several times during the sweep. A prebending spectrogram in Fig. 4a shows that peaks indicated by "1" in Fig. 3a are caused by a single vibration mode at 0.7 MHz. The peaks indicated by "2" in Fig. 3b,

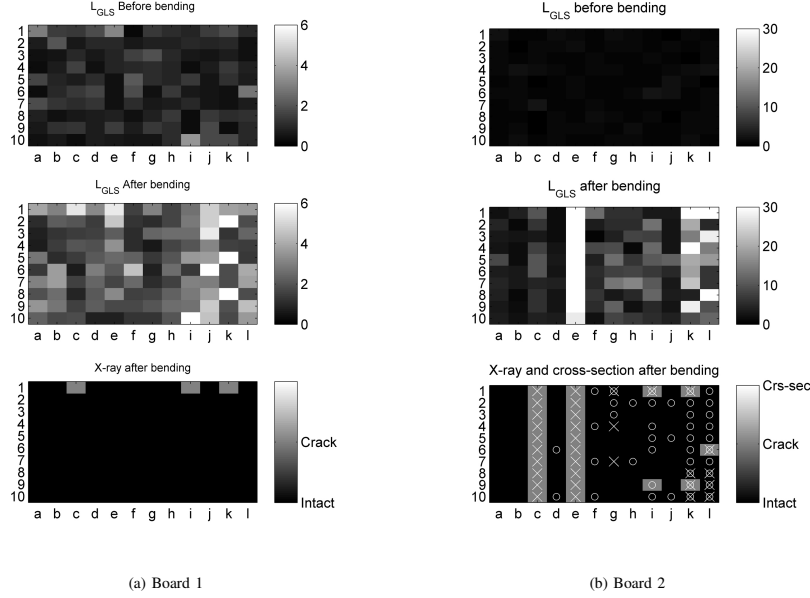


Fig. 5. From top to bottom: Calculated  $L_{GLS}$  values before and after 6000  $\mu$ Str bending, and X-ray-observed cracks (in gray) on Boards 1 and 2. The  $L_{GLS}$  values are proportional to the difference between the acoustic response of an individual capacitor and the average acoustic response of that capacitor type. The color scales are different for Boards 1 and 2, as Board 2 yielded a wider range of  $L_{GLS}$  values. Additionally, the bottom-right figure shows the results of a cross-section analysis performed on Board 2: cracks are indicated by "X" and delaminations by "O". The capacitors on Board 1 were not cross-sectioned.

instead, are all individual vibration modes, as seen from the corresponding spectrogram (Fig. 4b).

In the damaged capacitors, new resonant peaks typically emerged at specific frequencies, similarly among capacitors of the same case size. These vibration modes become observable because cracks in the ceramic body reduce the stiffness of the capacitor [17], [18].

### B. Population-level observations

In order to evaluate if the changes in the signals are statistically significant, acoustic data from 240 capacitors were analyzed and compared before and after a single bending. Changes in the acoustic response of an individual capacitor were characterized by comparing the postbending acoustic response with the prebending reference response using the  $L_{GLS}$  calculation in Eq. (5). The general increase in  $L_{GLS}$  values across both test boards (Fig. 5) indicates that bending the PCB changes the capacitor acoustic responses at the population level. Because this is an early-phase study, the capacitor population comprises various MLCCs with distinct acoustic responses. Therefore, no fixed  $L_{GLS}$  limits were set to categorize the capacitors either as damaged or intact.

To see how well the  $L_{GLS}$  values correlate with damage, the capacitors on both boards were inspected for cracks by

X-ray analysis. Significant acoustic changes were observed in the majority of cracked MLCCs. However, changes were also observed in a number of 2220-sized capacitors that showed no damage in the X-ray. Therefore, all the MLCCs on Board 2 were cross-sectioned, revealing several cracks that were not identified by the X-ray inspection. A number of delaminated capacitors were also observed, as delamination cannot be detected by the X-ray method. The experimental cumulative distribution in Fig. 6 shows that the  $L_{GLS}$  values for intact, damaged, and cracked groups differ in a statistically significant way. Thus, it can be concluded that the damage in the capacitors changes the acoustic behavior. The cracked capacitors appear to form two distinct groups, although this can probably be attributed to the relatively low number of samples.

Remarkably, the postbending  $L_{GLS}$  distribution for intact capacitors differs from the prebending. This is partly due to the fact that the reference envelope for a prebending measurement contains data from the measured capacitor itself. However, bending may actually change the acoustic behavior of a capacitor without actual damage. Another explanation is that some of the damages in the capacitors were left unidentified in both X-ray analysis and cross-sectioning. It is also possible that the bending of the PCB causes metal fatigue in the end terminations, solder, or the circuit board, which may alter the

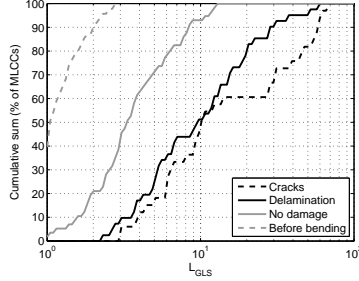


Fig. 6. Experimental cumulative distribution of  $L_{GLS}$  values for test board 2 before and after bending. Postbending distribution comprises capacitors that were delaminated and/or cracked, or remained intact. After bending, over 90% of the intact capacitors yielded  $L_{GLS}$  values below 10, whereas only 50% of damaged capacitors showed values below 10.

acoustic characteristics. Still, capacitors with actual observed damage show clearly higher  $L_{GLS}$  values than those where none are observed.

The 1206-sized capacitors showed little change in the  $L_{GLS}$  values after bending (Fig. 5a, columns a–f). In the X-ray analysis, cracks were found only in capacitor *c1*, which also showed significantly increased  $L_{GLS}$  values, meaning that the damage was observed acoustically.

The 1210-sized capacitors showed very nonuniform acoustic responses both before and after bending. The number and size of resonance peaks varied between the MLCCs, with typically either one or two large peaks found near 750 kHz (Fig. 7). This behavior makes the numerical comparison of envelopes fairly inaccurate, as the reference envelope  $\hat{e}_{ref}$  in Eq. (5) comprises dissimilar acoustic responses. As such, the few damaged capacitors in Fig. 5a (columns f–i) and Fig. 5b (columns d, b, and f) cannot be identified based on their  $L_{GLS}$  values. This nonuniform acoustic behavior should be taken into account in future studies.

The highest proportion of cracks was found in the 1812-sized capacitors, which also showed the best correspondence between  $L_{GLS}$  values and cracks (see Fig. 5b columns a, c, and e). The orientation of these capacitors correlated with the size of the cracks, and this correlation was also seen from the acoustic changes. No cracks were found in the 0°-oriented capacitors, which also yielded the lowest  $L_{GLS}$  values (column a). Small cracks, covering the width of the ceramic body only partially (see Fig. 8a), were found in column c (45°). Larger, full-width cracks (see Fig. 8b) were present in the 90°-oriented capacitors in column e; in some cases, the cracks also extended into the solder joint. However, there were not enough solder cracks to discuss them as a separate statistical population. The corresponding  $L_{GLS}$  values are higher for the capacitors with larger cracks, suggesting that it might be possible to evaluate the crack size acoustically.

Only five of the 2220-sized MLCCs showed cracks in the X-ray, which contradicted the elevated  $L_{GLS}$  values (Fig. 5b, columns g–i). Cross-sectioning revealed a number of

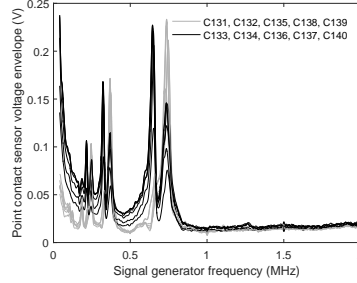


Fig. 7. Differing prebending acoustic responses of MLCCs from Board 2, column b (1210 case, flexible termination). Similar behavior was also observed in some 1210-sized MLCCs with normal terminations.

delaminated capacitors, plus additional cracks that were left undetected in the X-ray. Because cross-sectioning only provides information about a capacitor at one depth, it could not be used to quantify the damage. Furthermore, the inspection was done by eye, and thus, misidentifications are possible. However, the delaminations were largest and clearest in the 90°-oriented MLCCs in columns k and l, where also the highest  $L_{GLS}$  values were found. This further supports the finding that the degree of acoustic changes could correlate with the size of damage inflicted on a capacitor.

### C. Interference and uncertainty in acoustic measurements

Because the capacitors were simultaneously electrically excited and acoustically measured, the measurement data contained electromagnetic interference. Moreover, any external acoustic disturbances could cause artifacts in the acoustic data, thereby skewing the numerical comparison. The effect of external acoustic noise sources was minimized by performing the measurements in an anechoic room. However, the circuit board itself was observed to vibrate, causing a notable acoustic burst at the beginning of each sweep. The PCB vibrations were observable up to 40 kHz (see Fig. 9), and thus, frequencies below this were cut off from the measured acoustic signals. Above 40 kHz, the noise floor was dictated by the EMI from the measurement setup. The signal-to-noise ratio (SNR) of the acoustic signal was dependent on the capacitor size as the surface displacement of an MLCC is affected by its electrical and mechanical properties (see Table III). The 2220-sized MLCCs yielded the lowest acoustic resonance peaks, reducing the precision of the  $L_{GLS}$  comparison.

Furthermore, the general amplitude of the acoustic signals was affected by variations in the mechanical coupling between the sensor and the capacitor. Specifically, the least-squares fitting in Eq.(3) was chosen to counter this variation.

## V. DISCUSSION

The results show that MLCC acoustic behavior can be characterized by using a piezoelectric sensor, and this behavior

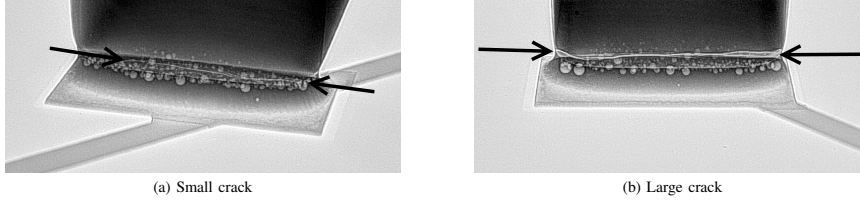


Fig. 8. X-ray images of MLCC end terminations, showing flex cracks (endpoints indicated by arrows). The capacitor in (a) was oriented at a  $45^\circ$  angle relative to the bending direction, resulting in a narrower crack than in (b), oriented at  $90^\circ$ . Capacitors with wider cracks also showed higher acoustic changes. The damage seen in (a) is typical for capacitors in column *c* in Fig. 5b, whereas cracks like in (b) were found in column *e* capacitors in Fig. 5b.

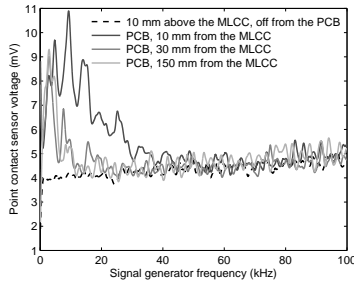


Fig. 9. Acoustic emissions measured from PCB surface and above an MLCC. The results show that vibration of the test board has very little effect on the measured acoustic emissions above 40 kHz.

TABLE III  
MEAN AND STANDARD DEVIATION OF ACOUSTIC EMISSION PEAK VOLTAGES FOR INTACT MLCCs

Case size	Mean ( $e_{\text{peak}}$ )(V)	Std ( $e_{\text{peak}}$ )(V)	Std (%)
1206	0.0874	0.0247	28
1210	0.1588	0.0447	28
1812	0.1230	0.0237	19
2220	0.0284	0.0052	18

is altered by circuit board bending. In individual capacitors, the changes are seen as an increased amplitude of mechanical resonance peaks, and introduction of new peaks. Furthermore, when the typical acoustic behavior of a capacitor is known, a single capacitor can be numerically compared with a reference waveform of that particular type of capacitor.

Both cracks and delaminations produced changes in the acoustic signatures of the capacitors. The magnitude of these changes was observed to somewhat correlate with the size of damage found in a capacitor, although quantifying the damage was not feasible. The population-level increase in the  $L_{\text{GLS}}$  values of damaged capacitors shows that cracks and delaminations can be identified acoustically. Machine learning and more advanced feature extraction tools could be implemented for more precise damage detection, although a more exhaustive sample of MLCCs is also needed. It can be assumed that cracks and delaminations affect the mechanical

properties in different ways. Thus, it might be possible to acoustically differentiate between a cracked and a delaminated capacitor; this is a subject for further research.

Because the EMI noise from the excitation signal occurs at the same frequency with the acoustic emissions, simple low-pass filtering is not feasible. A more advanced denoising method (e.g. wavelet-based) could be applied to improve the signal-to-noise ratio. Moreover, the measurement setup should be improved for better EMI shielding and more consistent sensor-capacitor contact. Because the frequency range of the sensor used in this study is limited to 2.5 MHz, a sensor with a higher frequency range should be used if capacitors of a smaller case size (e.g. 0603) were to be measured.

## VI. CONCLUSION

Direct measurements of acoustic emissions from Multilayer Ceramic Capacitors were demonstrated using a piezoelectric point contact sensor. MLCCs were measured both pristine and after damaging them by bending the test circuit boards once. The acoustic measurements were then compared with X-ray and cross-section images. The results show that mechanical damage, such as flex cracks and delaminations, changes the acoustic behavior of the MLCCs. The acoustic changes in capacitors were characterized with a numerical algorithm, showing that the circuit board bending affects the acoustic response of the MLCCs at the population level in a statistically significant way. Furthermore, it appears that the degree of acoustic changes correlates with the level of physical damage to the capacitor. In the light of these results, an acoustic emission-based defect detection method for MLCCs could be developed. Still, the precision and error sensitivity of the acoustic measurements leave room for improvement. Additionally, the relationship between the acoustic signatures and the quality of damage in capacitors is a subject for further work.

## REFERENCES

- [1] B.-H. Ko, S.-G. Jeong, Y.-G. Ahn, K.-S. Park, N.-C. Park, and Y.-P. Park, "Analysis of the correlation between acoustic noise and vibration generated by a multi-layer ceramic capacitor," *Microsyst Technol.*, 2014.
- [2] C.-W. Huang, B.-T. Chen, K.-Y. Chen, C.-H. Hsueh, W.-C. Wei, and C.-T. Lee, "Finite element analysis and design of thermal-mechanical stresses in multilayer ceramic capacitors," *International Journal of Applied Ceramic Technology*, vol. 12, no. 2, pp. 451–460, Mar. 2015.
- [3] T. Adams, "Preventing mlcc failures," *Circuits Assembly*, Aug. 2009.



- [4] J. Bergenthal and J. D. Prymak, "Capacitance monitoring while flex testing," in *1994 Proceedings. 44th Electronic Components and Technology Conference*, DOI 10.1109/ECTC.1994.367528, pp. 854–860, May. 1994.
- [5] J. A. Ahmar and S. Wiese, "A finite element modelling and fracture mechanical approach of multilayer ceramic capacitors," in *16th International Conference on Thermal, Mechanical and Multi-Physics Simulation and Experiments in Microelectronics and Microsystems*, 2015.
- [6] T. Adams, "High acoustic frequency imaging," *Ceramic Industry*, vol. 164, no. 2, pp. 14–16, 2014.
- [7] S. Kahn and R. Checkaneck, "Acoustic emission testing of multilayer ceramic capacitors," *IEEE Trans. Compon., Hybrids, Manuf. Technol.*, vol. 6, DOI 10.1109/TCHMT.1983.1136222, no. 4, pp. 517–526, Dec. 1983.
- [8] J. M. J. den Toonder, C. W. Rademaker, and C. . Hu, "Residual stresses in multilayer ceramic capacitors: Measurement and computation," *Journal of Electronic Packaging (Transactions of the ASME)*, vol. 125, no. 4, pp. 506–511.
- [9] G. Vogel, "Avoiding flex cracks in ceramic capacitors: Analytical tool for a reliable failure analysis and guideline for positioning cercaps on pcbs," *Microelectronics Reliability*, Jun. 2015.
- [10] L. Bechou, S. Mejdji, Y. Ousten, and Y. Danto, "Non-destructive detection and localization of defects in multilayer ceramic chip capacitors using electromechanical resonances," *Quality and reliability engineering international*, 1996.
- [11] W. L. Johnson, S. A. Kim, G. S. White, J. Herzberger, K. L. Peterson, and P. R. Heyliger, "Time-domain analysis of resonant acoustic nonlinearity arising from cracks in multilayer ceramic capacitors," *AIP Conference Proceedings*, vol. 1706, DOI <http://dx.doi.org/10.1063/1.4940511>, 2016.
- [12] V. Krieger, W. Wondrak, A. Dehbi, W. Bartel, Y. Ousten, and B. Levrier, "Defect detection in multilayer ceramic capacitors," *Microelectronics Reliability*, vol. 46, DOI <http://dx.doi.org/10.1016/j.microrel.2006.07.082>, no. 9, pp. 1926–1931, 2006.
- [13] Y. C. Chan, F. Yeung, G. Jin, N. Bao, and P. S. Chung, "Nondestructive detection of defects in miniaturized multilayer ceramic capacitors using digital speckle correlation techniques," *IEEE Transactions on Components, Packaging, and Manufacturing Technology Part A*, vol. 18, no. 3, pp. 677–684, 1995.
- [14] D. L. Commare, "Nondestructive evaluation of mlccs," *Ceramic Industry*, vol. 140, no. 6, pp. 38–41, 1993.
- [15] G. F. Kieran, "A comparison of screening techniques for ceramic capacitors," *Capacitor Technologies, Applications and Reliability; Marshall Space Flight Center*, pp. 111–117, Feb. 1981.
- [16] C. Andersson, J. Ingman, E. Varescon, and M. Kiviniemi, "Detection of cracks in multilayer ceramic capacitors by x-ray imaging," *Microelectronics Reliability*, vol. 64, DOI <http://doi.org/10.1016/j.microrel.2016.07.110>, pp. 352–356, 2016.
- [17] D. S. Erdahl and I. C. Ume, "Online-offline laser ultrasonic quality inspection tool for multilayer ceramic capacitors-part i," *IEEE Trans. Adv. Packag.*, 2004.
- [18] D. S. Erdahl and I. C. Ume, "Online-offline laser ultrasonic quality inspection tool for multilayer ceramic capacitors-part ii," *IEEE Trans. Adv. Packag.*, 2005.
- [19] W. L. Johnson, S. A. Kim, G. S. White, and J. Herzberger, "Nonlinear resonant acoustic detection of cracks in multilayer ceramic capacitors," in *2014 IEEE International Ultrasonics Symposium*, DOI 10.1109/ULT-SYM.2014.0062, pp. 244–247, Sep. 2014.
- [20] W. L. Johnson, J. L. Herzberger, S. A. Kim, K. L. Peterson, P. R. Heyliger, and G. S. White, "Resonant acoustic frequency shifts associated with cracks in multilayer ceramic capacitors," *IEEE Trans. Device Mater. Rel.*, vol. PP, DOI 10.1109/TDMR.2017.2682818, no. 99, pp. 1–1, 2017.
- [21] T. J. Kärkkäinen, J. P. Talvitie, M. Kuisma, J. Hannonen, J. P. Ström, E. Mengotti, and P. Silventoinen, "Acoustic emission in power semiconductor modules – first observations," *IEEE Trans. Power Electron.*, vol. 29, DOI 10.1109/TPEL.2013.2295460, no. 11, pp. 6081–6086, Nov. 2014.
- [22] T. J. Kärkkäinen, J. P. Talvitie, O. Ikonen, M. Kuisma, P. Silventoinen, and E. Mengotti, "Sounds from semiconductors – acoustic emission experiment with a power module," in *2014 16th European Conference on Power Electronics and Applications*, DOI 10.1109/EPE.2014.6910840, pp. 1–6, Aug. 2014.
- [23] S. Müller, C. Drechsler, U. Heinkel, and C. Herold, "Acoustic emission for state-of-health determination in power modules," in *2016 13th International Multi-Conference on Systems, Signals Devices (SSD)*, DOI 10.1109/SSD.2016.7473704, pp. 468–471, Mar. 2016.
- [24] J. D. Prymak, "Piezoelectric effects ceramic chip capacitors (singing capacitors)," *Arrow Asian Times*, 2006, KEMET Electronics Corp.
- [25] J. Chen and Z. Feng, "X7r dielectric multilayer ceramic capacitors show good micro-actuating properties with little hysteresis," *Electronics Letters*, vol. 50, DOI 10.1049/el.2013.3815, no. 7, pp. 538–540, 2014, cited By 2.



**Saku Levikari** was born in 1991 in Finland. He is currently working with Lappeenranta University of Technology (LUT) Laboratory of Applied Electronics, finishing his Master's thesis on acoustic evaluation of Multilayer Ceramic Capacitors.



**Tommi J. Kärkkäinen** (M'12) was born in 1987 in Finland. He received the B.Sc., M.Sc. and D.Sc. degrees from Lappeenranta University of Technology (LUT), Lappeenranta, Finland, in 2010, 2011 and 2015, respectively.

He is currently a Post-Doctoral Researcher with LUT School of Energy Systems. His main research topic is the utilisation of acoustic phenomena to the condition monitoring and health testing of electronics components, and related metrology and signal processing.



**Caroline Andersson** (M'10) was born 1983 in Sweden. She received the M.Sc. degree from the faculty of engineering at Lund University (LTH) in Sweden, and her PhD from the Swiss Federal Institute of Technology (ETH) in Zurich, Switzerland. She is currently working as a senior scientist at ABB Corporate Research Center in Switzerland on the topic of reliability of power electronics. The main focus of her research area is accelerated life testing, physics of failure and reliability of components and systems.



**Juha Tamminen** was born in 1980 in Finland. He received his B.Eng. in Electronics in 2006 from Espoo-Vantaa University of Applied Sciences. He is currently working as a design manager at ABB Drives in Finland in the field of production testing. His work concentrates on improving production testing concepts in pursue of better quality and productivity.



**Pertti Silventoinen** (M'09) was born in Simpele, Finland, in 1965. He received the D.Sc degree from Lappeenranta University of Technology (LUT), Lappeenranta, Finland, in 2001. He became a professor of applied electronics in 2004. His current research interests include power electronics systems in various applications.

## **Publication II**

Levikari S., Kärkkäinen T., Andersson C., Tamminen J., and Silventoinen P.  
**Acoustic Detection of Cracks and Delamination in Multilayer Ceramic Capacitors**

Reprinted with permission from  
*IEEE Transactions on Industry Applications*  
Vol. 55, Iss. 2, March–April 2019, pp. 1787–1794  
© 2018, IEEE



# Acoustic Detection of Cracks and Delamination in Multilayer Ceramic Capacitors

Saku Levikari , Member, IEEE, Tommi J. Kärkkäinen , Member, IEEE, Caroline Andersson , Member, IEEE, Juha Tammminen, and Pertti Silventoinen, Member, IEEE

**Abstract**—Multilayer ceramic capacitors (MLCC) are the most widely used capacitor type in the electronics industry. However, the brittle ceramic dielectric makes MLCCs prone to mechanical damage. Manufacturing defects or damage during board assembly may cause a capacitor to prematurely fail during its operational life. Here, we demonstrate the fast and non-destructive acoustic screening of MLCCs. Soldered 2220-sized MLCCs were subjected to ac voltage frequency sweeps, causing them to vibrate mechanically. Acoustic responses of the capacitors were measured before and after subjecting the test circuit board to severe bending. The results show that the cracks and delaminations caused by bending induce characteristic changes in the capacitors' acoustic response. A support vector machine classifier was trained to successfully detect damaged capacitors based on their acoustic response.

**Index Terms**—Acoustic emission, ceramic capacitors, nondestructive testing.

## I. INTRODUCTION

MULTILAYER ceramic capacitors (MLCCs) are commonly used in the electronics industry [1]. The ceramic dielectric gives MLCCs high capacitance per volume, but also makes them prone to mechanical damage.

Voids and delaminations are typical manufacturing defects in MLCCs, often related to thermal stresses [2], [3]. Mechanical stress, such as improper printed circuit board (PCB) handling during assembly, can lead to cracks or delamination in MLCCs [4], [5]. Mechanical damage in MLCCs is often left unrecognized during production or assembly, as the capacitor may operate normally electrically. However, in the field, a crack or delamination in an MLCC may grow in size, resulting in loss of

capacitance, shortened lifespan, or an open or short contact [6]. Larger case size capacitors, used in, e.g., power electronics, have shown to be more prone to damage from PCB bending than the more commonly used cases in the 0402 to 1206 range [7]. Testing the capacitors at the assembly line of the system would prevent unexpected damage in the field. At this moment, however, a suitable quality assurance, or production testing method does not exist.

Defects or damage in MLCCs can be detected by mechanical microsectioning [8] and chemical etching [9], but these methods are destructive for the capacitor and are therefore unsuitable for production testing. Recently, an X-ray imaging method with sufficient accuracy for reliable crack detection has been proposed [10]. Delamination defects, however, cannot be seen in X-ray images. Other proposed nondestructive methods include ultrasound imaging [5], acoustic emission counting using a mechanical ram [6], impedance analysis under dc bias [11], leakage current monitoring [12], laser speckle pattern analysis [13], opto-acoustic microscopy [14], and neutron radiography [15].

In this paper, the quality assurance testing goal is approached by measuring the acoustic phenomena of the MLCCs. When under ac voltage, MLCCs generate acoustic emissions. Acoustic emissions are physical vibrations caused by the piezoelectric properties of the dielectric ( $\text{BaTiO}_3$ ) [16], [17]. Recently, it was shown that a narrow-pulse frequency sweep signal can be used to produce vibration in MLCCs, and that bending the circuit board in order to produce cracks in the MLCCs changes the acoustic emission characteristics of the capacitors [18]. Similar findings have been made by Johnson *et al.* using resonant ultrasound spectroscopy [19]–[21]. The acoustic approach is particularly interesting, since there is a need in the industry for a method that could identify damaged capacitors from an assembled board. Acoustic monitoring has also been applied for other electronic components, such as power semiconductor modules [22]–[24].

The term *acoustic emission* does not necessarily refer to audible sounds in the human hearing range. Indeed in this context, the authors use the term as a synonym for vibration occurring in the capacitor, caused by the electromechanical phenomena within the capacitor itself.

In this study, acoustic signals produced using the method from [18] are measured using a point contact sensor. Acoustic measurements are conducted before and after bending the circuit board. The measured waveforms are then analyzed and correlated against bending-induced damage in the capacitors. In order to determine the suitability of acoustic measurements for

Manuscript received April 5, 2018; revised August 17, 2018; accepted August 29, 2018. Date of publication October 3, 2018; date of current version February 20, 2019. This work was supported in part by the TEKES under project Finnish Solar Revolution and in part by Academy of Finland under Grant 278496. Paper 2018-PEDCC-0324.R1, presented at the 2017 IEEE International Symposium on Diagnostics for Electrical Machines, Power Electronics and Drives, Tinos, Greece, Aug. 29–Sep. 1, and approved for publication in the IEEE TRANSACTIONS ON INDUSTRY APPLICATIONS by the Power Electronic Devices and Components Committee of the IEEE Industry Applications Society. (Corresponding author: Saku Levikari.)

S. Levikari, T. J. Kärkkäinen, and P. Silventoinen are with the LUT School of Energy Systems, Lappeenranta University of Technology, 53850 Lappeenranta, Finland (e-mail: saku.levikari@lut.fi; tommi.karkkainen@lut.fi; pertti.silventoinen@lut.fi).

C. Andersson is with ABB Corporate Research Center, 5405 Baden-Dättwil, Switzerland (e-mail: caroline.andersson@ch.abb.com).

J. Tammminen is with ABB Drives, FI-00381 Helsinki, Finland (e-mail: juha.tammminen@fi.abb.com).

Color versions of one or more of the figures in this paper are available online at <http://ieeexplore.ieee.org>.

Digital Object Identifier 10.1109/TIA.2018.2873989

TABLE I  
EXCITATION SWEEP SIGNAL FOR MLCCS

Type	Pulse wave
Duration	100 ms
Frequency range	100 Hz ... 2 MHz
Voltage	-10 V ... +10 V
Duty cycle	80%
Frequency slope	linear

detection of physical damage, a support vector machine (SVM) [25] is trained on the acoustic data to classify the MLCCs as either damaged or undamaged. The key observation from the data is that the changes in the acoustic emission correlate quite well to delamination of the end termination in the capacitors, better than to the existence of cracks. This suggests that it may be possible to develop a delamination detection method based on acoustic emission. Such a method would be very welcome, because at the moment a non-destructive test method for finding delamination in MLCCs does not exist. The acoustic measurement may be useful in identifying cracked capacitors as well, even though the correlation in the analyzed signals is not as good as it is for delamination.

This paper has been improved from its original form, published in the SDEMPED 2017 conference [26].

## II. EXPERIMENT

The experiment was conducted on 60 2220-sized MLCC capacitors of 22  $\mu$ F, assembled on a purpose-built PCB. Half of the capacitors were flexible end termination capacitors, while the others had "normal" end terminations.

The experimental procedure was as follows: first, the capacitors were characterized individually by driving them with frequency-swept voltage while measuring their acoustic emissions using a point contact sensor. The test board was then subjected to a controlled bending to damage the MLCCs. After bending, the capacitors were re-characterized acoustically. X-ray imaging and cross-sectioning were used to obtain accurate information on the actual condition of each capacitor.

After obtaining all the data described above, changes observed in the acoustic data were compared to the damage observed in each capacitor. In addition to 2220-sized MLCCs, the effect of circuit board bending has also been acoustically observed in case of sizes 1206, 1210, and 1812, all of which yield stronger acoustic response than 2220 [27]. Because PCB bending-caused flex cracks have been an issue especially with larger case sizes, this study was performed on 2220-size capacitors. The acoustic data, alongside X-ray and cross-sectioning results, are publicly available [28].

### A. Acoustic Characterization

To obtain an acoustic response, the MLCCs were driven with a pulse frequency sweep signal specified in Table I. A KRN Services KRNBB-PC broadband point contact sensor was attached to the capacitor being characterized (see Fig. 1). The signal was amplified using a KRN AMP-1BB-J measurement amplifier and then recorded using a Keysight MSO-X 4104A

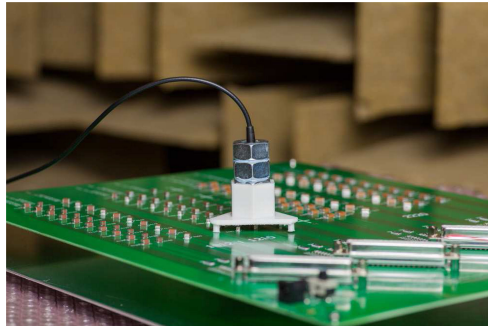


Fig. 1. Point contact sensor placed on top of a capacitor. The sensor is within a 3-D printed fixture on the test PCB, allowing the sensor to be in place without holding it manually.

oscilloscope. The test was conducted in an anechoic room in order to minimize any external acoustic disturbances.

The signal from the point contact sensor contains a significant amount of electromagnetic interference (EMI). The harmonics of the pulsed input signal also excite the resonant frequencies of an MLCC to appear several times during a sweep [18]. Moreover, at frequencies below 50 kHz, a high-amplitude burst likely related to PCB vibration occurred in most of the measurements.

To remove the harmonics and EMI, the signals were processed using wavelet decomposition and low-pass filtering. After these stages, the envelope curve of the signal was calculated. The envelope curve is treated as the acoustic response of the capacitor because it is more convenient to compare envelopes than raw acoustic responses.

The acoustic characterization process was conducted in an identical manner before and after bending.

### B. Inflicting Damage to the Capacitors

The test board was bent with a Zwick-Roell Z010 four-point bending setup. Under 18-mm bending displacement, the PCB was subjected to strain levels between 5800 and 8000  $\mu$ Str measured at the board centerline, with an average of 6000  $\mu$ Str.

In reality, a PCB does not experience uniform bending in one direction, especially directly aligned with the orientation of the capacitor. To take this into account, capacitors were assembled in three different angles relative to the direction of the bending. This affects the type and location of damage within the capacitor.

### C. X-Ray Imaging and Cross-Sectioning

After the test board bending, the capacitors were inspected for cracks by X-ray imaging using a Phoenix Nanomex machine. The capacitors were also cross-sectioned to reveal any delamination, which cannot be seen by X-ray. This was done by casting the MLCCs in two-phase epoxy, grinding them with a Struers Rotopol-11 to a desired depth, and then polishing the surface for inspection with a Leica M205C optical microscope.

Cross-sectioning gives accurate information of the condition in the depth that the capacitor has been ground to. If a crack or delamination can be seen in this depth, the capacitor is classified as being damaged. If no damage is seen, however, the existence of damage cannot be ruled out, since a crack or delamination can reside deeper in the capacitor. For this reason, capacitors that showed no damage but exhibited slight changes in their acoustic characteristics were imaged at three different depths to get better understanding of the condition.

The authors would like to point out that cross-sectioning is a very labor-intensive process. It is not feasible to do a complete cross-sectioning of every capacitor at multiple depths. For this reason, full-depth cross-sectioning was not performed for every capacitor.

#### D. SVM Classification

Intuitive discrimination between damaged and undamaged capacitors by inspecting the acoustic responses is difficult and infeasible. Instead, the classification must be based directly on features of the acoustic data. Because each capacitor will yield different numeric features, reliable classification based on strict conditional expressions would be impracticable. Therefore, the machine learning approach is more suitable for the classification task. SVM are machine learning based binary classifiers that have been successfully utilized in signal classification tasks [25], [29], [30]. In the basic SVM approach, the data consist of samples (in this case, the MLCCs) belonging in either positive (1) or negative (0) category. From each sample,  $n$  numerical features are extracted. The samples are then mapped onto an  $n$ -dimensional feature space, where each dimension corresponds to a certain feature. The SVM classifier is then trained by fitting a *decision plane* into the sample points such that it separates the points in the positive and negative categories by the largest possible margin. Often in real-world scenarios, the data are not linearly separable, i.e., points in different categories overlap. In such a situation, the data points may be mapped into a transformed feature space using a nonlinear kernel function. Furthermore, a cost function is often employed: data points on the wrong side of the decision surface correspond to a total cost, which is minimized as a part of the decision plane fitting [25].

For the task of classifying capacitors, the SVM was trained by extracting only two features from the raw data. This approach kept the classifier model simple and helped in preventing overfitting. Additionally, two-dimensional feature data were convenient to visualize and use in conjunction with the statistical analysis and visual inspection of acoustic responses.

### III. RESULTS

All the acoustic emission envelopes contained a strong resonance peak at circa 500 kHz, related to the fundamental resonance modes of the capacitor body. The authors refer to this peak as the *main peak* of the capacitor. As can be seen in Fig. 2, the value of this peak is almost doubled between the measurements for a capacitor with no damage. This change seems very significant at first, but further results suggest that the doubled value is still not very large. The increase in the peak value

may be explained by better sensor-to-capacitor contact during the second measurement. Another probable explanation is that the 6000  $\mu$ Str bending actually caused some degree of physical changes that were missed during the X-ray inspection and microsectioning, since cracks and delaminations can be difficult to detect from the images. Some changes can be seen at frequencies lower than that of the main peak, but they are not as significant.

In a capacitor which showed significant delamination in the cross-sectioning (see Fig. 3), the changes are much more pronounced. The main peak value is increased to over four times that of a typical value for a pre-bending measurement. Even though not all delaminated capacitors exhibited values this high, notably increased main peak values were observed in the majority of them. On the other hand, most of the capacitors did not show delamination as significant as in Fig. 3(b), where a clear gap can be seen extending horizontally across the end termination.

At lower frequencies, the changes are comparable to those of an undamaged capacitor. New resonance peaks appear at frequencies higher than that of the main peak, but compared to the main peak, their value is very low.

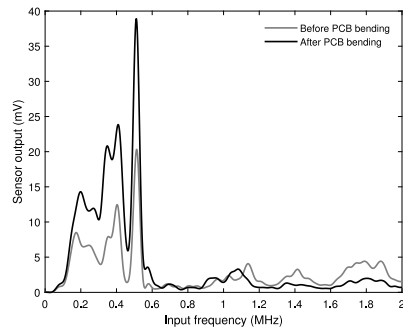
The main peak of a capacitor with cracks (see Fig. 4) exhibits changes even smaller than the intact capacitor. The cracked capacitor does, however, exhibit a new resonance peak at ca. 800 kHz. The emergence of such a peak was observed in multiple cracked capacitors. The frequency of this peak varies from capacitor to capacitor, and is likely to be affected by the size and location of the crack. Nevertheless, the overall emergence of this peak, referred to as the *secondary peak*, was observed to correlate with the presence of damage. The crack shown in Fig. 4(b) is approximately 500  $\mu$ m in length and 5 mm in width, extending across the capacitor end termination. Since this crack causes noticeable changes in the capacitors acoustic response [see Fig. 4(a)], it is very likely that also smaller cracks and delaminations cause acoustically observable changes.

To study these peaks and the related damage statistically, the main and secondary peak values were obtained programmatically for every acoustic measurement. For this purpose, the main peak value was defined as the highest peak value at frequencies lower than 700 kHz. The secondary peak value, respectively, was defined as the highest peak value at frequencies higher than 700 kHz. The cross section and X-ray images of every capacitor were examined, and each capacitor was deemed to either have or not have a crack, and to either have or not have delamination.

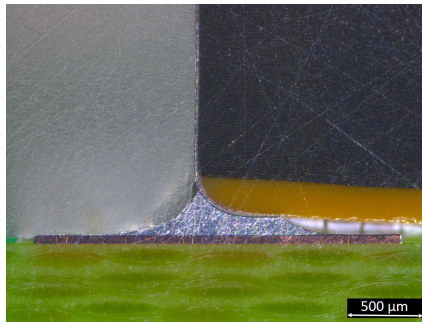
These results were then used to determine which peak indicates which type of damage (see Fig. 5). It is evident that the higher the main peak value, the more likely a capacitor is to have delamination damage. The secondary peak value, on the other hand, does not exhibit such a direct relation to the emergence of delamination.

The main peak value seems to be a poor tool for identifying cracked capacitors. Fig. 5 does not suggest a clear trend between the main peak value and the likelihood of a crack. On the other hand, a weak trend can be observed between the secondary peak value and the emergence of cracks. However, high secondary peak values are not unambiguously an indication of cracks.



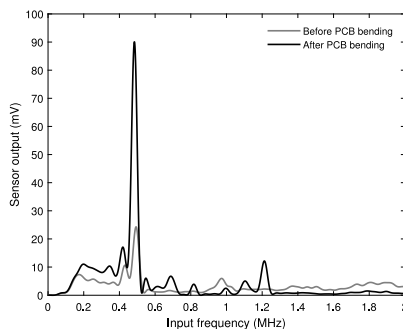


(a) Acoustic response of C198 before and after bending

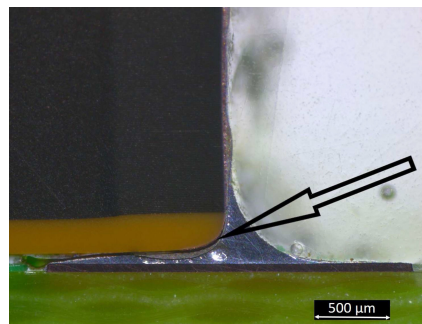


(b) Cross-section of C198 after bending. No cracks or delamination can be seen.

Fig. 2. Typical example of an MLCC with no observed damage after the bending of the PCB. Slight main peak amplitude increase is seen in (a) at around 500 kHz, but no new resonant peaks are introduced.

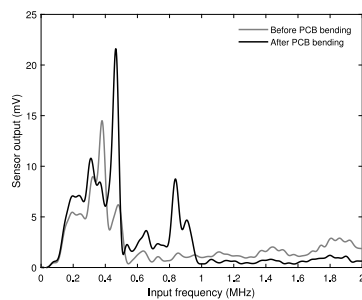


(a) Acoustic response of C224 before and after bending

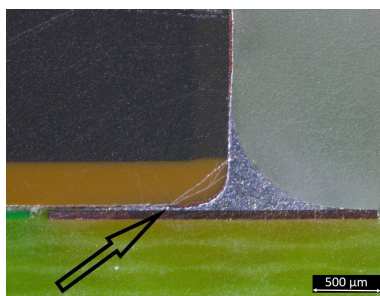


(b) Cross-section of C224 after bending, showing delamination under the right-hand-side termination.

Fig. 3. Typical example of a capacitor with delamination. The acoustic response in (a) shows significant increase in the main peak value, and several new peaks at different frequencies are introduced above 0.6 MHz.



(a) Acoustic response of C201 before and after bending



(b) Cross-section of C201 after bending, showing cracks in the passive area near the right-hand-side termination.

Fig. 4. Typical example of an MLCC with multiple cracks near the termination. Main peak amplitude increase and new resonant peaks around 800 kHz are seen in (a).

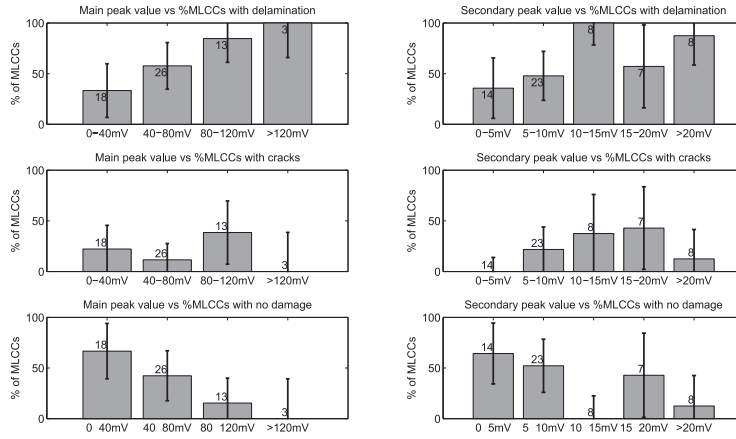


Fig. 5. Histograms describing the relationships amongst cracks, delamination, and acoustic emission peak values of 60 MLCCs. The bins are based on the peak values, and the numbers indicate the total amount of MLCCs in each bin. The error bars depict the combined uncertainty of measurement and sampling errors (see Appendix). Significant correlation between delamination and increased main peak value can be seen, whereas secondary peak values weakly correlate with the occurrence of cracks. Both peak values are generally lower for undamaged capacitors.

Undamaged MLCCs appear to exhibit lower values than damaged capacitors, both in terms of main and secondary peaks. This suggests that an increase in either of the peak values is a possible sign of damage.

#### A. Detecting Damaged Capacitors Using SVM Classifiers

In order to discriminate between damaged and undamaged MLCCs, an SVM classifier was trained on data extracted from the acoustic measurements. Each MLCC was mapped onto a two-dimensional feature space, with the features being the main and secondary peak values after the PCB bending. Each MLCC was labeled either damaged or undamaged, depending whether or not cracks and/or delamination were observed in the cross-sectioning. The SVM classifier was then trained by fitting a decision surface into the data set as shown in Fig. 6. A Gaussian kernel function was chosen for the SVM model, since it performed better than polynomial kernels. A linear SVM was unable to separate the datapoints properly, whereas using polynomial kernel functions caused the SVM model to overfit into the data.

Because the data set consisted of only 60 MLCCs, dividing it into separate training and validation sets would have had significant negative effect on the performance of the classifier. Instead, *leave-one-out cross validation* [31] was used to evaluate the performance of the classifier: the SVM was trained on data from all but one MLCC, and the performance of the classifier was tested with the left-out MLCC. This procedure was repeated for all 60 MLCCs, simulating the performance of the SVM on data outside the training set.

In classifying undamaged capacitors, the SVM model performed equally well for both in-sample (training) and cross-validated data [see Fig. 7(a) and (b)]. In cross valida-

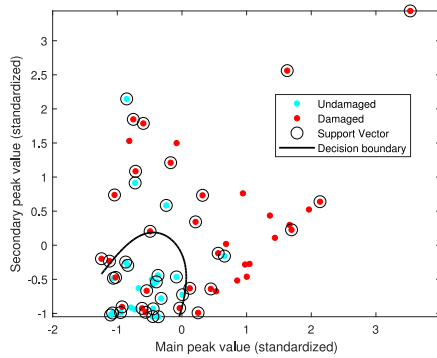


Fig. 6. SVM classifier fitted into observed MLCC features. The peak height data were obtained from the acoustic measurements after bending the PCB. In order to improve the classifier performance, the data were standardized to zero mean and unit variance. Capacitors which showed either delamination and/or cracks in the cross-sectioning are labeled as damaged.

tion, damaged MLCCs were missed by the classifier slightly more often, while the SVM was still able to detect three out of four damaged capacitors. The overall cross-validated accuracy of the classifier was 78.3%, whereas the recall (how many of the damaged capacitors were found) was 75.7%.

The operation of the classifier at different threshold values is visualized by the receiver operating characteristic (ROC) [32] curve in Fig. 8. With out-of-sample data, the SVM classifier performs similarly as with data within the training set. The area under ROC curve (AUROC) with out-of-sample data is approximately 0.78, indicating a fairly good classifier despite the small amount of training data. A perfect classifier would



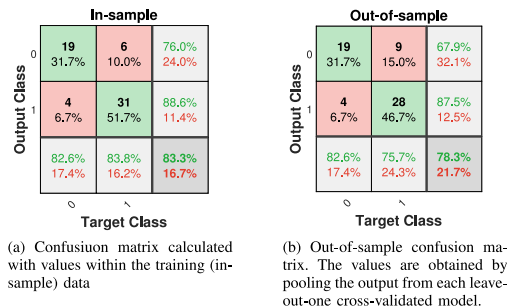


Fig. 7. SVM classifier confusion matrices for MLCCs in the training data set and combined cross-validation results.

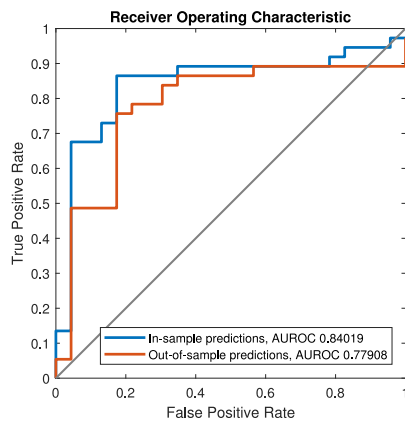


Fig. 8. ROC of the trained SVM classifier at different output threshold values. AUROC measures the overall performance of the classifier: a perfect classifier has an AUROC of 1.0, whereas pure guessing produces an AUROC of 0.5.

have an AUROC value of 1.0, whereas purely random guessing would produce an AUROC of 0.5. The performance of the classifier could be improved by including more of the features in the acoustic response, provided that the features actually carry information about the condition of a capacitor.

The classification results presented here are for an SVM trained to detect whether or not the capacitor had suffered any kind of damage. Classifiers were also trained to detect specifically either delamination or cracks. Delamination was detected with only slightly lower performance than the combined classifier. For cracks, however, the classifier output was negative for every single capacitor. Unlike in Fig. 6, the cracked capacitors mapped onto the feature space formed no clear cluster for the decision plane to separate from the rest of the data. This suggests that while the main and secondary peak values are enough to determine whether or not an MLCC is delaminated, other features should be extracted if cracks were to be detected.

#### IV. DISCUSSION

The data obtained in this study suggest that main peak value may turn out to be a valuable metric in identifying delaminated capacitors, especially when used together with secondary peak value information. However, neither of these peak values seem to explicitly indicate the presence of cracks.

In the analysis presented in this paper, only two peak values are taken into account. As it is mentioned in Section III, the secondary peak frequency is not fixed, and varies from capacitor to capacitor. Considering how simple the extracted features are and how small a portion of the frequency response is used, the SVM classifier performs remarkably well. However, capacitors containing only cracks were left undetected.

The determination of delamination and cracks presented in Figs. 5 and 6 is not guaranteed to be error free. The data were obtained by looking at cross section images of the capacitors, and in such a process misidentification is a possibility. Training the SVM model with misidentified capacitors would decrease its accuracy. Nevertheless, the performance of the SVM classifier surpassed the initial expectations of the authors based on visual and statistical observations.

It is likely that by extracting proper features, such as more resonant peaks and their frequency information, the classifier performance would improve both for crack and delamination detection. More flexible classifiers, such as neural networks or random forests could also yield better results; this is a matter for further study. Moreover, the acoustic approach could be used as a complementary method to X-ray analysis, which can identify cracks accurately, but not delaminations.

The cracks and delaminations in this study were relatively small, the vast majority of them residing in the passive region of the capacitors. Nevertheless, even a small fault in a capacitor can grow over time, and water can get inside the component with harmful results. Even though the dimensions of a damaged region cannot be accurately defined by cross section images, damage at the capacitor termination less than 500  $\mu\text{m}$  long can cause changes in the acoustic signature.

Remarkably, the results were identical for flex and “normal” termination capacitors. The authors expected that some difference would be seen between these capacitor types, but this turned out not to be the case. From the production testing point of view, this is a welcome result, as the test method would not have to be redesigned for different termination types.

Even though the capacitors used in this study are physically larger than those found in, e.g., consumer electronics, acoustic screening is applicable for case sizes of 1206 and below [27]. It must also be noted that smaller capacitors are not as prone to damage from bending [7]. Therefore, the most potential applications of acoustic screening are in, e.g., power electronics, where large case sizes and heavy circuit board assemblies increase the risk of flex cracks and delamination.

The physical phenomena causing the changes in the acoustic response has not been discussed yet. It seems likely that delamination near the end terminations of an MLCC allows the capacitor to vibrate more freely in a direction perpendicular to the PCB surface. Because vibration in this direction creates the

largest displacement for the point contact sensor, increase in main peak values is observed. Resonance peaks observed in the secondary peak region have lower amplitude, and thus are likely related to other resonance modes of the capacitor body. A possible explanation for this is that cracks in the ceramic body allow the MLCC to vibrate more freely along these modes, causing secondary peaks to appear.

## V. CONCLUSION

A set of MLCCs was investigated acoustically before and after inflicting damage. The changes in the acoustic characteristics were analyzed and compared against the damage observed in each capacitor. The acoustic data were also used to train an SVM classifier to detect damaged capacitors.

The main finding was that delamination of the capacitor causes quite consistent changes in the acoustic response of a capacitor. Cracks in the capacitor cause changes as well, but are not as easy to detect as those caused by delamination.

The SVM classifier showed promising performance. Nevertheless, further study on feature extraction and classifier algorithms is required to develop a reliable capacitor screening method based on acoustic emission.

## APPENDIX

In order to calculate the error bars for Fig. 5, two major sources of measurement uncertainty were identified: 1) the misidentification of cracks and delaminations in the cross section images, and 2) the sampling error caused by the relatively low number of capacitors in many of the bins in Fig. 5.

Other sources of uncertainty, such as the uncertainty present in the measurement instruments, do exist in this case. It was estimated that their contribution to the total uncertainty of the measurement was insignificant when compared to the uncertainty of the identification of damage and the sampling error.

For the identification of cracks, it was estimated that the likelihood of a false positive, i.e., an intact capacitor being incorrectly determined as having a crack, was 1%. The likelihood of a false negative, i.e., a cracked capacitor being incorrectly determined as being intact, was estimated to be 5%. Similarly, for the identification of delamination, the false positive rate was estimated as 5%, and the true positive rate as 10%.

Using these false identification rates, the maximum and minimum bounds of the error  $a_+$  and  $a_-$  were calculated. This yields an asymmetrical distribution of error, which is difficult to handle in the uncertainty estimation process. For this reason, these bounds were converted into a single standard uncertainty value  $u_1$  based on [33, Sec. 4.3.8] as

$$u_1^2 = \frac{a_+ - a_-}{12}. \quad (1)$$

To estimate the effect of sampling error, upper and lower bounds were taken from the chart in [34, p. 494]. In this case, the distribution is heavily skewed, especially in the bins where the number of capacitors is low. The obtained upper and lower bounds were again used to obtain a single

standard uncertainty value

$$u_2^2 = \frac{a_+ - a_-}{12}. \quad (2)$$

The two standard uncertainty values were then merged into a combined uncertainty

$$u_c = \sqrt{u_1^2 + u_2^2} \quad (3)$$

which was then multiplied with a coverage factor  $k = 1.960$  to expand the uncertainty to a confidence level of 95%. The bar height in Fig. 5 is the observed percentage of capacitors  $p$  in each bin, and the error bars cover the range  $p \pm ku_c$ . The error bars are cut at 100% and 0% because values outside these values are not meaningful.

The authors would like to note that this analysis is heavily simplified. The resulting uncertainty estimates are taken to be good enough for an understanding of how well the results can be generalized to another, similar capacitor population.

## ACKNOWLEDGMENT

The authors would like to thank J.-Y. Loisy and S. T. Yildiz at ABB Corporate Research for cross-section sample preparation and imaging by optical microscopy.

## REFERENCES

- [1] B.-H. Ko, S.-G. Jeong, Y.-G. Ahn, K.-S. Park, N.-C. Park, and Y.-P. Park, "Analysis of the correlation between acoustic noise and vibration generated by a multi-layer ceramic capacitor," *Microsyst. Technol.*, vol. 20, nos. 8/9, pp. 1671–1677, 2014.
- [2] C.-W. Huang, B.-T. Chen, K.-Y. Chen, C.-H. Hsueh, W.-C. Wei, and C.-T. Lee, "Finite element analysis and design of thermal-mechanical stresses in multilayer ceramic capacitors," *Int. J. Appl. Ceramic Technol.*, vol. 12, no. 2, pp. 451–460, Mar. 2015. [Online]. Available: <http://search.proquest.com/docview/1660318462?accountid=136582>.
- [3] T. Adams, "Preventing MLCC failures," *Circuits Assembly*, pp. 17–19, Aug. 20, 2009. [Online]. Available: <https://www.circuitsassembly.com/ca/editorial/menu-features/296-current-articles/17452-preventing-mlcc-failures.html>
- [4] J. A. Ahmar and S. Wiese, "A finite element modelling and fracture mechanical approach of multilayer ceramic capacitors," in *Proc. 16th Int. Conf. Thermal, Mech. Multi-Physics Simul. Experiments Microelectronics Microsystems*, Apr. 2015, pp. 1–5.
- [5] T. Adams, "High acoustic frequency imaging," *Ceramic Ind.*, vol. 164, no. 2, pp. 14–16, 2014. [Online]. Available: <http://search.ebscohost.com/login.aspx?direct=true&db=bth&AN=94147595&site=ehost-live>
- [6] S. R. Kahn and R. W. Checkaneck, "Acoustic emission testing of multilayer ceramic capacitors," *IEEE Trans. Compon., Hybrids, Manuf. Technol.*, vol. CHMT-6, no. 4, pp. 517–526, Dec. 1983.
- [7] M. Keimasi, M. H. Azarian, and M. G. Pecht, "Flex cracking of multilayer ceramic capacitors assembled with pb-free and tinlead solders," *IEEE Trans. Dev. Mater. Rel.*, vol. 8, no. 1, pp. 182–192, Mar. 2008.
- [8] J. M. J. den Toonder, C. W. Rademaker, and C.-L. Hu, "Residual stresses in multilayer ceramic capacitors: Measurement and computation," *J. Elect. Packag.*, vol. 125, no. 4, pp. 506–511, Dec. 2003.
- [9] G. Vogel, "Avoiding flex cracks in ceramic capacitors: Analytical tool for a reliable failure analysis and guideline for positioning cercaps on PCBs," *Microelectron. Rel.*, vol. 55, no. 9, pp. 2159–2164, 2015.
- [10] C. Andersson, J. Ingman, E. Varescon, and M. Kiviniemi, "Detection of cracks in multilayer ceramic capacitors by x-ray imaging," *Microelectron. Rel.*, vol. 64, pp. 352–356, 2016. [Online]. Available: <http://www.sciencedirect.com/science/article/pii/S0026271416302542>
- [11] L. Bechou, S. Mejdji, Y. Ousten, and Y. Danto, "Non-destructive detection and localization of defects in multilayer ceramic chip capacitors using electromechanical resonances," *Quality Rel. Eng. Int.*, vol. 12, pp. 43–53, 1996.

- [12] V. Krieger, W. Wondrak, A. Dehbi, W. Bartel, Y. Ousten, and B. Levrier, "Defect detection in multilayer ceramic capacitors," *Microelectron. Rel.*, vol. 46, pp. 1926–1931, 2006.
- [13] Y. C. Chan, F. Yeung, G. Jin, N. Bao, and P. S. Chung, "Nondestructive detection of defects in miniaturized multilayer ceramic capacitors using digital speckle correlation techniques," *IEEE Trans. Compon., Packag., Manuf. Technol. A*, vol. 18, no. 3, pp. 677–684, Oct. 1995. [Online]. Available: <http://search.proquest.com/docview/27455226?accountid=136582>
- [14] D. L. Commare, "Nondestructive evaluation of MLCCs," *Ceramic Ind.*, vol. 140, no. 6, pp. 38–41, 1993.
- [15] G. F. Kieran, "A comparison of screening techniques for ceramic capacitors," in *Proc. Symp. NASA Conf. Capacitor Technol., Appl. Rel.*, 1981, pp. 111–117.
- [16] J. D. Prymak, "Piezoelectric effects ceramic chip capacitors (singing capacitors)," *Arrow Asian Times article*, KEMET Electronics Corporation, Aug. 2006. [Online]. Available: <http://www.kemet.com/Lists/TechnicalArticles/Attachments/88/2006%2007%20ArrowAsiaTimes%20-%20MLC%20Noise.pdf>
- [17] J. Chen and Z. Feng, "X7r dielectric multilayer ceramic capacitors show good micro-actuating properties with little hysteresis," *Electron. Lett.*, vol. 50, no. 7, pp. 538–540, Mar. 2014.
- [18] S. Levikari, T. J. Kärkkäinen, C. Andersson, J. Tamminen, and P. Silventoinen, "Acoustic phenomena in damaged ceramic capacitors," *IEEE Trans. Ind. Electron.*, vol. 65, no. 1, pp. 570–577, Jan. 2018.
- [19] W. L. Johnson, S. A. Kim, G. S. White, and J. Herzberger, "Nonlinear resonant acoustic detection of cracks in multilayer ceramic capacitors," in *Proc. IEEE Int. Ultrason. Symp.*, Sep. 2014, pp. 244–247.
- [20] W. L. Johnson, S. A. Kim, G. S. White, J. Herzberger, K. L. Peterson, and P. R. Heyliger, "Time-domain analysis of resonant acoustic nonlinearity arising from cracks in multilayer ceramic capacitors," in *Proc. AIP Conf. Proc.*, 2016, vol. 1706.
- [21] W. L. Johnson, J. L. Herzberger, S. A. Kim, K. L. Peterson, P. R. Heyliger, and G. S. White, "Resonant acoustic frequency shifts associated with cracks in multilayer ceramic capacitors," *IEEE Trans. Device Mater. Rel.*, vol. 17, no. 2, pp. 316–323, Jun. 2017.
- [22] T. J. Kärkkäinen, J. P. Talvitie, O. Ikonen, M. Kuisma, P. Silventoinen, and E. Mengotti, "Sounds from semiconductors – acoustic emission experiment with a power module," in *Proc. 16th Eur. Conf. Power Electron. Appl.*, Aug. 2014, pp. 1–6.
- [23] T. J. Kärkkäinen *et al.*, "Acoustic emission in power semiconductor modules – first observations," *IEEE Trans. Power Electron.*, vol. 29, no. 11, pp. 6081–6086, Nov. 2014.
- [24] T. J. Kärkkäinen, J. P. Talvitie, M. Kuisma, P. Silventoinen, and E. Mengotti, "Acoustic emission caused by the failure of a power transistor," in *Proc. IEEE Appl. Power Electron. Conf. Expo.*, Mar. 2015, pp. 2481–2484.
- [25] C. Cortes and V. Vapnik, "Support-vector networks," *Mach. Learn.*, vol. 20, no. 3, pp. 273–297, Sep. 1995. [Online]. Available: <https://doi.org/10.1007/BF00994018>
- [26] S. Levikari, T. J. Kärkkäinen, P. Silventoinen, C. Andersson, and J. Tamminen, "Acoustic detection of cracks and delamination in multilayer ceramic capacitors," in *Proc. IEEE 11th Int. Symp. Diagnostics Electr. Mach., Power Electron. Drives*, Aug. 2017, pp. 622–627.
- [27] S. Levikari, "Detection of cracks: Acoustic experiments on multilayer ceramic capacitors," M.Sc. thesis, Lappeenranta Univ. Technol., Lappeenranta, Finland, 2018.
- [28] S. Levikari, T. J. Kärkkäinen, C. Andersson, and J. Tamminen, "MLCC acoustic data set," Lappeenranta Univ. Technol., Lappeenranta, Finland, 2018. [Online]. Available: <http://urn.fi/urn:nbn:fi:csc-kata20180302153714692880>
- [29] S. Siuly, Y. Li, and Y. Zhang, *EEG Signal Analysis and Classification*. New York, NY, USA: Springer, 2016.
- [30] M. Li, X. Liu, and X. Liu, "Infrasound signal classification based on spectral entropy and support vector machine," *Appl. Acoust.*, vol. 113, pp. 116–120, 2016. [Online]. Available: <http://www.sciencedirect.com/science/article/pii/S0003682X16301761>
- [31] G. Dougherty, *Pattern Recognition and Classification: An Introduction*. New York, NY, USA: Springer, 2013, ch. 9.
- [32] T. Fawcett, "An introduction to ROC analysis," *Pattern Recognit. Letters*, vol. 27, no. 8, pp. 861–874, 2006.
- [33] JCGM, *100:2008 Evaluation of Measurement Data – Guide to the Expression of Uncertainty in Measurement*, corrected version 2010 ed. JCGM, 2010.
- [34] L. Råde and B. Westergren, *Mathematics Handbook for Science and Engineering*. Lund, Sweden: Studentlitteratur, 1988, 2004.



**Saku Levikari** (M'18) was born in 1991 in Finland. He received the B.Sc. and M.Sc. degrees from Lappeenranta University of Technology (LUT), Lappeenranta, Finland, in May and June of 2018, respectively.

He is currently a Doctoral Student with LUT School of Energy Systems, Laboratory of Applied Electronics. His main research topics include the field of data analytics and machine learning, with main focus on wearable electronics and the reliability of power electronics.



**Tommi J. Kärkkäinen** (M'12) was born in 1987 in Finland. He received the B.Sc., M.Sc., and D.Sc. degrees from Lappeenranta University of Technology (LUT), Lappeenranta, Finland, in 2010, 2011, and 2015, respectively.

He is currently a Postdoctoral Researcher with LUT School of Energy Systems. His main research topic is the reliability of power electronic devices and systems, and the utilization of machine learning algorithms to improve the reliability and productivity of various systems.



**Caroline Andersson** (M'10) was born 1983 in Sweden. She received the M.Sc. degree from Lund University, Lund, Sweden, and the Ph.D. degree from Swiss Federal Institute of Technology, Zurich, Switzerland.

She is currently a Senior Scientist with ABB Corporate Research Center, Baden, Switzerland, on the topic of reliability of power electronics. The main focus of her research area is accelerated life testing, physics of failure, and reliability of components and systems.



**Juha Tamminen** was born in 1980 in Finland. He received the B.Eng. degree in electronics in 2006 from Espoo-Vantaa University of Applied Sciences, Vantaa, Finland.

He is currently a Design Manager with ABB Drives, Helsinki, Finland, in the field of production testing. His work concentrates on improving production testing concepts in pursue of better quality and productivity.



**Pertti Silventoinen** (M'09) was born in Simpele, Finland, in 1965. He received the D.Sc. degree from Lappeenranta University of Technology, Lappeenranta, Finland, in 2001.

He became a Professor of applied electronics in 2004. His current research interests include power electronics systems in various applications.

## **Publication III**

Levikari S., Kärkkäinen T., Andersson C., Tamminen J., and Silventoinen P.  
**Nondestructive Acoustic Testing of Ceramic Capacitors using One-Class Support  
Vector Machine with Automated Hyperparameter Selection**

Reprinted under Creative Commons (CC BY 4.0) from

*IEEE Access*

Online, 2020

Vol. 8, December 2020, pp. 226337–226351

© 2020, CC BY 4.0



# Nondestructive Acoustic Testing of Ceramic Capacitors using One-Class Support Vector Machine with Automated Hyperparameter Selection

SAKU LEVIKARI<sup>1</sup>, (Member, IEEE), TOMMI J. KÄRKKÄINEN<sup>1</sup>, (Member, IEEE), CAROLINE ANDERSSON<sup>2</sup>, (Member, IEEE), JUHA TAMMINEN<sup>3</sup>, (Member, IEEE), MIKKO NYKYRI<sup>1</sup>, (Member, IEEE), PERTTI SILVENTOINEN<sup>1</sup>, (Member, IEEE)

<sup>1</sup>LUT University, Lappeenranta, Finland (e-mail: firstname.lastname@lut.fi)

<sup>2</sup>ABB Schweiz AG, Turgi, Switzerland (e-mail: caroline.andersson@ch.abb.com)

<sup>3</sup>ABB Oy Drives, Helsinki, Finland (e-mail: juha.tamminen1@fi.abb.com)

Corresponding author: Saku Levikari (e-mail: saku.levikari@lut.fi).

This work was supported by Business Finland through the project SolarX.

**ABSTRACT** The energy transition and electrification across many industries place increasingly more weight on the reliability of power electronics. A significant fraction of breakdowns in electronic devices result from capacitor failures. Multilayer ceramic capacitors, the most common capacitor type, are especially prone to mechanical damage, for instance, during the assembly of a printed circuit board. Such damage may dramatically shorten the life span of the component, eventually resulting in failure of the entire electronic device. Unfortunately, current electrical production line testing methods are often unable to reveal these types of damage. While recent studies have shown that acoustic measurements can provide information about the structural condition of a capacitor, reliable detection of damage from acoustic signals remains difficult. Although supervised machine learning classifiers have been proposed as a solution, they require a large training data set containing manually inspected damaged and intact capacitor samples. In this work, acoustic identification of damaged capacitors is demonstrated without a manually labeled data set. Accurate and robust classification is achieved by using a one-class support vector machine, a machine learning model trained solely on intact capacitors. Furthermore, a new algorithm for optimizing the classification performance of the model is presented. By the proposed approach, acoustic testing can be generalized to various capacitor sizes, making it a potential tool for production line testing.

**INDEX TERMS** Ceramic capacitors, acoustic emission, nondestructive testing, support vector machines

## I. INTRODUCTION

THE ONGOING ENERGY TRANSITION has resulted in exponential growth in the market for power electronics, with applications such as inverters and drives gaining ground in renewable energy production and the electrification of transport [1]. This places more weight on the reliability of power electronics devices, as their abrupt failure will cause costly repairs, downtime, and in worst cases, even life-threatening situations. It has been estimated that 30% of failures in electronics are caused by capacitors [2], the most widely used type of which is the multilayer ceramic capacitor (MLCC) with more than  $10^{12}$  units produced yearly [3].

Cracks are the most prevalent failure mode in ceramic capacitors [4]. The reason for this can be traced back to the structure of the MLCC, which consists of interleaved metal electrodes with ceramic dielectric (typically barium titanate,  $\text{BaTiO}_3$ ) in between. The ceramic material gives the capacitors a high permittivity [5], but also makes them fragile. Thus, MLCCs can be damaged during the assembly of the printed circuit board (PCB), for example, as a result of thermal stresses during soldering or mechanical mishandling of the circuit board. Common examples of stress-induced damage include cracks in the dielectric material and delamination between internal electrodes or between the capacitor body

and its end terminations or solder joints [6]. Defects related to the manufacturing process of the component are also likely to increase the probability of damage during assembly [4]. Large case sizes (1812 and up) in particular have been shown to be prone to bending damage [7], and while the majority of the MLCC demand is focused on smaller case sizes found in consumer electronics and automotive industry [8], larger case sizes remain common in industrial applications and power electronics [9].

Detecting a faulty MLCC can be difficult, because the damage may not be visible on the outside of the component. If a crack occurs within the active area of the capacitor, for example cutting through a portion of the internal electrodes, the damage can be observed as a reduced capacitance. On the other hand, if a crack or delamination resides in the passive region of the MLCC or at the solder joints, the electrical operation of the component is likely to remain unaffected at first [10]. However, the damaged location may grow in size over time, leading to a reduced capacitance, open- or short-circuit [11], or deterioration of the dielectric material as moisture gets inside the capacitor [12], [13]. While the probability of failure for a single capacitor is very low, capacitor failures contribute to a significant fraction of faults in the field owing to the high number of components that are used [4]. A fast and reliable postassembly MLCC screening method would therefore be a highly valuable quality tool for quality assurance.

#### A. DETECTING DAMAGE IN MLCCs

Various methods for detecting damaged MLCCs have been proposed over the years, with a thorough survey on the topic available for instance in [4]. As pointed out in the survey, techniques commonly found in screening and quality assurance applications include electrical, optical, and non-contact ultrasound measurements. However, these methods are mainly applied to detecting manufacturing defects instead of damage caused later on in the production line. Moreover, the crack detection capability of these methods is limited, with electrical measurements often unable to detect cracks and optical methods limited to the surface of the component. C-scan ultrasonic microscopy has traditionally been capable of detecting only horizontally spanning defects in MLCCs, even though a newer technique capable of observing vertical damage has also been developed. However, this method is mainly used in R&D and pilot production [14] as it includes submerging the component in water, and it is not able to reveal damage in areas covered by end terminations [4].

For a more thorough inspection, a capacitor can be chemically etched [15] or mechanically microsectioned [16] in order to reveal damage in the ceramic body, but these methods are slow, laborious, and destructive to the component. Recently, X-ray imaging methods with sufficient accuracy for detecting cracks [16] and dielectric breakdown defects [17] have been developed. However, these methods require manual interpretation of the X-ray images. Moreover, delamination between the ceramic body and the solder joints cannot

be seen by X-ray imaging, and cracks in the capacitor body are only visible from certain angles.

#### B. ACOUSTIC EMISSIONS IN MLCCs

MLCCs are known to generate acoustic emissions when subjected to alternating voltage. This phenomenon arises from the piezoelectric properties of the ceramic dielectric, making the capacitor body physically vibrate as the ceramic material deforms under an AC field [18]. To date, there are several studies about observing cracks in the ceramic body of an MLCC by changes in its resonant behavior [19]–[21]. These experiments are mainly based on ferroelectric transduction, where a DC-biased MLCC is excited using short radio frequency tone bursts, and the decay of the MLCC “ringing” after the burst is observed.

A more recent method introduced by the authors is based on electrically exciting the component to vibration, simultaneously measuring the vibrations using a point contact sensor [22]. However, while the acoustic emissions carry information about the structural condition of a capacitor, the signs of damage can be hard to detect. The amplitudes and frequencies of the mechanical resonances exhibited by MLCCs show variation even between intact components, and although mechanical damage often manifests as new resonant peaks, such peaks do not always appear [23]. Moreover, factors such as electromagnetic interference and variations in the mechanical contact between the sensor and the capacitor can cause artifacts that could be misinterpreted as signs of damage. Supervised machine learning algorithms were proposed in [23] as a solution on a small number of damaged MLCCs, yet the accuracy and applicability of the method remained inconclusive. A major disadvantage of such an approach is that a supervised machine learning model requires a large annotated data set on which the model is trained. This, in turn, requires acoustic measurements on a number of capacitors, which are then labeled as intact or damaged. The labeling process itself has to be carried out manually for instance by microsectioning, which itself is a laborious and error-prone procedure.

In this study, the authors continue their prior work reported in [22] and [23] by showing that MLCC acoustic emission measurement can be used as a practical quality assurance testing method without the need for a laborious and error-prone labeling process. This is successfully demonstrated by identifying damaged MLCCs using the one-class support vector machine, a machine learning model trained only on pristine capacitor samples. Furthermore, a new algorithm for optimizing the hyperparameters of the model is introduced. By combining the proposed algorithm with proper feature extraction, the model can be made robust against error sources in the measurement setup and intrinsic variations between individual components.

## II. METHODS AND RATIONALE

The task of acoustically detecting damaged MLCCs was approached as a machine learning problem, because it is in-



feasible to manually set the classification rules [23]. Machine learning models commonly employ a supervised learning strategy, in other words, the model is trained on a data set of annotated samples. In the case of detecting faulty MLCCs, a two-class classifier would be a natural solution, as the main interest is to know whether a capacitor is damaged (class 1) or not (class 0). To this end, the model would require a training data set consisting of MLCC acoustic signatures, each associated with a class label, 0 or 1. However, the process of constructing such a data set is work-intensive and prone to error, as a sufficiently large number (dozens or hundreds) of examples from both classes are needed for the training process. While the acoustic characterization process itself is relatively simple and fast, annotating the capacitor samples for instance by microsectioning or X-ray is time consuming. Visual interpretation of the results is also an error-prone process, which leads to training data with mislabeled examples. This degrades the performance of the classifier and makes the evaluation of the model more difficult. Different failure modes are also likely to induce different characteristics in the acoustic response, and thus, dozens or hundreds of capacitors with cracks and delaminations are needed. Moreover, the size and internal structure of an MLCC affect both the acoustic characteristics and the most prevalent failure modes of the component. Thus, each MLCC size and capacitance should preferably have a data set of its own.

To overcome these limitations, a one-class support vector machine (OSVM), a machine learning model that learns from only a single class of examples, is employed. The model is used to determine whether a new acoustic signature is similar to known pristine signatures or not, thereby eliminating the need for annotated examples of damaged MLCCs. However, the performance of the model strongly depends on its hyperparameters, which are set before the learning process. Several methods for optimizing these parameters exist, but they typically require either beforehand knowledge of the classification problem, or counter examples, which in the case of MLCCs are costly to obtain. To facilitate fully automated hyperparameter optimization with no counter examples or *a priori* knowledge of the problem, a new algorithm is presented. The proposed approach can drastically reduce the amount of work on constructing a labeled data set of acoustic emissions, as only a few samples will be needed for testing the performance of the model. While the use of an OSVM in the context of screening MLCCs is novel, it has previously been used in other damage detection and condition monitoring applications, where data representing anomalous instances are difficult or expensive to collect [24]–[27].

The experimental section of this paper is organized as follows: first, an acoustic data set is composed of measurements performed by the authors in a prior study [23] on a set of intact and mechanically damaged MLCCs. For each capacitor, a set of numerical features are extracted from the raw acoustic data. Each MLCC is then attached with a label indicating whether the component is damaged or not.

**TABLE 1.** Equipment used for Acoustic Emission measurements (refer to Fig. 2)

Device	Make and model
Signal generator	Agilent 33250A
Point contact sensor	KRN Services KRNBB-PC
Preamplifier	KRN Services AMP-1BB-J
Oscilloscope	Keysight InfiniiVision MSO-X 4104A

For automated detection of damaged MLCCs, an OSVM model is trained using data only from intact components. To achieve a high detection rate with few false alarms, an algorithm for optimizing the hyperparameters of the model is introduced and tested on commonly used benchmark data sets. Finally, the performance of the OSVM model is tested against damaged and undamaged capacitors.

#### A. ACOUSTIC EMISSION MEASUREMENTS ON MLCCS

The raw data used in this study originate from measurements performed by the authors in [22] and [23]. The measurements were conducted by subjecting soldered MLCCs to an excitation signal, simultaneously measuring the acoustic response of the capacitor using a piezoelectric point contact sensor placed on top of the component (see Fig. 1). An AC voltage chirp with pulsed waveform (duty cycle 80%,  $\pm 10$  V<sub>peak-to-peak</sub>) was used as the excitation signal, with frequency linearly increasing from 100 Hz to 2 MHz over a duration of 100 ms. This study was performed on 2220-size MLCCs, as larger capacitors are more likely to be affected by damage related to soldering and assembly. The capacitors were from two manufacturers, all rated at 24 V and 22  $\mu$ F, and soldered on the test PCBs in three different azimuthal orientations (0°, 45°, and 90°). The acoustic emission measurement setup is depicted in Fig. 2 along with other preprocessing and analysis steps, and the measurement equipment is listed in Table 1.

The capacitors were soldered on two identical custom-made test boards (PCB 1 and PCB 2) with 60 MLCCs each. Each capacitor was acoustically characterized, after which the capacitors on PCB 1 were mechanically damaged by subjecting the board to a controlled four-point bending setup with an average bending strain of 6000  $\mu$ Str. The capacitors on PCB 1 were then recharacterized, cut from the PCB, and inspected for damage using cross-sectioning. Both cracks and delaminations were found during the inspection, with the length of the delaminations ranging from 200  $\mu$ m to 500  $\mu$ m and the smallest cracks being only 100  $\mu$ m in size. A selected set of the MLCCs were also inspected for cracks with X-ray imaging because their acoustic signatures appeared slightly anomalous. The cross-sectioning and X-ray imaging were performed in the same study as the acoustic measurements; more comprehensive descriptions of the methods are available in [22] and [23].



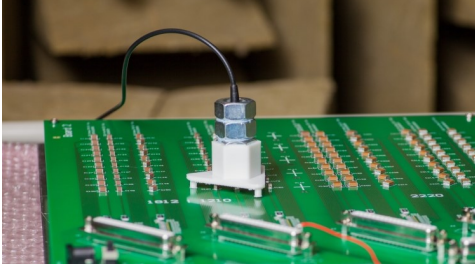


FIGURE 1. Acoustic measurement setup [22] showing the point contact sensor placed on top of an MLCC. The sensor itself is housed in a 3D-printed fixture.

### B. PREPROCESSING OF ACOUSTIC DATA

The raw acoustic waveforms (see Fig. 3A) were filtered using interval-dependent wavelet denoising. A second-order biorthogonal wavelet with eight vanishing moments was chosen for accurate signal approximation and smooth reconstructed waveform. After denoising, the waveforms were high-pass filtered in order to remove the high-amplitude burst below 150 kHz seen in Fig. 3A, likely related to PCB resonances [28], using a fourth-order Butterworth filter with a cutoff frequency of 150 kHz. After this, the harmonics caused by the pulsed waveform of the excitation signal were removed. To achieve this without losing the content of the acoustic signal at the excitation frequency, the signal was divided into 64 blocks with a 50% overlap. To facilitate an accurate overlap-add decomposition [29], each block was windowed using the von Hann function, and then low-pass filtered using a fourth-order Butterworth filter with a cutoff frequency of 1.3 times the excitation frequency at the endpoint of the block to remove the frequency content above the first harmonic. Finally, the filtered signal  $u(t)$  was reconstructed from the filtered blocks using the overlap-add method. The aforementioned steps were performed using zero-phase forward-backward filtering to avoid distorting the phase of the signal.

After filtering, the envelope  $e(t)$  (see Fig. 3B) was calculated from the filtered signal  $u(t)$  using the Hilbert transform  $\mathcal{H}$  as

$$e(t) = \text{DS} \left\{ \text{lpf} \left[ \sqrt{(u(t))^2 + \text{Re} \{ \mathcal{H}(u(t)) \}^2} \right] \right\}, \quad (1)$$

where DS and lpf denote downsampling and low-pass filtering, and Re denotes the real part of the Hilbert transform. The envelope can be seen as the acoustic amplitude response of the capacitor. In addition, the instantaneous phase response (see Fig. 3C) was calculated for each MLCC as

$$\phi(t) = \text{DS} \left\{ \text{lpf} \left[ \angle \mathcal{H} \left( \frac{u(t)}{C(t)} \right) \right] \right\}, \quad (2)$$

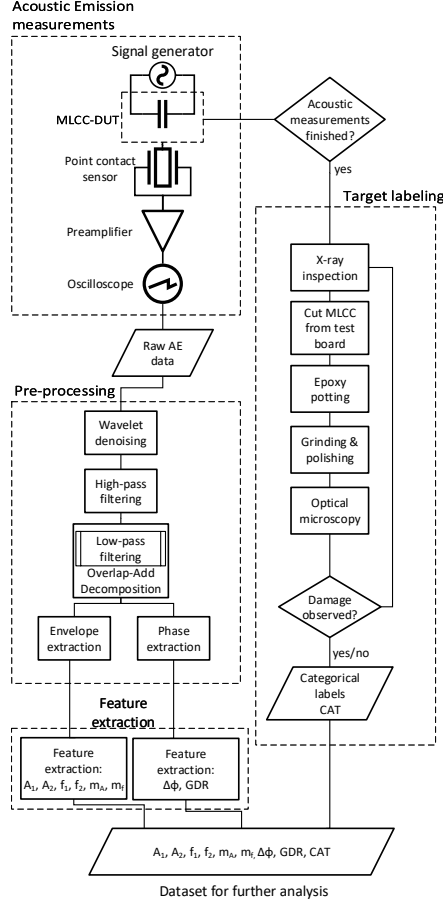


FIGURE 2. Flowchart of the procedure for composing the acoustic emission (AE) data set (from top to bottom). Raw acoustic data, optical microscopy images, and X-ray images originate from prior work of the authors [22], [23]. The data set used in this study was composed by processing the raw acoustic data and inspecting the cross-sectional and X-ray images. A total of 180 MLCC samples from two test boards were included in the data set: 60 intact capacitors from PCBs 1 and 2 each, and 60 capacitors from PCB 1 after a controlled bending procedure. The extracted features and categorical labels were used as input and output variables for the OSVM model.

where  $C$  is a linear sinusoidal chirp whose frequency sweep corresponds to the acoustic excitation signal. Finally, the resulting amplitude and phase responses were downsampled to 10 000 points each for feature extraction. All parameters related to signal processing were chosen empirically by examining acoustic data from both damaged and undamaged capacitors.

### C. FEATURE EXTRACTION

Feature engineering is a critical part of constructing a machine learning model, as its purpose is to reduce the dimensionality of the data and provide the model with only relevant information about the problem. To this end, a set of numerical features were extracted for each capacitor sample after preprocessing the raw acoustic waveforms.

While machine learning models using raw waveforms have been developed [30], such models are usually trained on large data sets with tens or hundreds of thousands of samples. Training a model with plain acoustic waveforms is unfeasible in this case, because the size of the data set is limited, and only a small fraction of the points in a single waveform are relevant. Moreover, the acoustic waveforms cannot be downsampled to under 500 points without losing the characteristics of the data, whereas most machine learning models perform poorly when the dimensionality of the data is higher than the number of samples [31].

Because the total number of capacitors was only 180, the number of features had to be limited to a number much smaller than the size of the data set. Furthermore, the features themselves had to be robust so that no external factor, such as EMI noise or variations in the sensor-capacitor contact, would bias the classification results. Based on these conditions, eight numerical features shown in Table 2 were extracted for each MLCC. The resonant peak amplitudes  $A_1$  and  $A_2$  along with their corresponding resonance frequencies  $f_1$  and  $f_2$  were chosen, as past studies [20], [21], [23] have suggested that these resonance peaks might indicate the presence of damage. However, especially  $A_1$  and  $A_2$  displayed notable systematic differences between two intact PCBs, probably related to external factors such as the level of ambient EMI, as the two boards were characterized on different occasions. Nevertheless, resonant peaks were assumed to be a very likely indicator of physical damage, and thus, the feature set was appended with the median amplitude  $m_A$  and frequency  $m_f$  of ten of the highest resonant peaks below 700 kHz. Furthermore, it was assumed that mechanical damage would cause distortions in the acoustic phase response of a capacitor body. Therefore, the total phase shift  $\Delta\phi$  was calculated for each capacitor. Finally, as an additional indicator of phase distortions, the mean group delay ripple  $GDR$  was calculated as the mean value of deviations from a linear frequency slope, as shown in Fig. 3D.

Finally, an acoustic data set (see Table 3) was composed by combining the extracted acoustic features with the microsectioning and X-ray results. Thus, the acoustic response of each MLCC is represented as a vector

$$x_i = (A_1, A_2, f_1, f_2, \Delta\phi, m_A, m_f, GDR) \quad (3)$$

and the data set  $X$  consists of pairs of feature vector  $x_i$  and class label  $y_i$

$$X = \{(x_i, y_i) | x_i \in \mathbb{R}^8, y_i \in \{0, 1\}\} \quad (4)$$

where  $i = 1 \dots 180$ ,  $y = 0$  denotes nondamaged and  $y = 1$  damaged MLCC. All data in  $X$  were standardized to zero

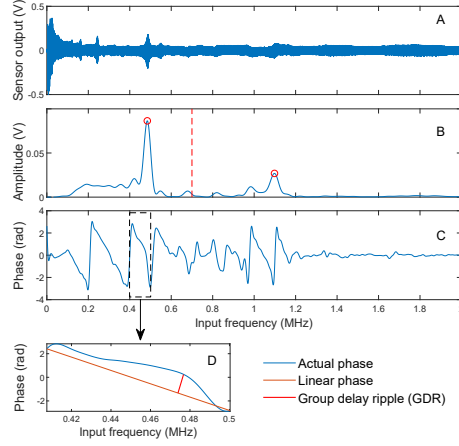


**FIGURE 3.** Numerical features (see Table 2) were extracted from raw acoustic signatures (example shown in A). From the signal envelope (B), amplitudes and frequencies of the highest peaks below and above 700 kHz (the dashed red line) were used as features (marked with red circles). Additionally, the median amplitude and frequency of all resonance peaks in B were chosen as features. From the phase graph (shown in C), total phase shift and group delay ripple (zoomed-in section D) were used as features.

**TABLE 2.** Features extracted from the acoustic responses

(1)	$A_1$	Amplitude of the highest peak below 700 kHz, typically found at approx. 500 kHz
(2)	$A_2$	Amplitude of the highest peak above 700 kHz
(3)	$f_1$	Frequency of $A_1$
(4)	$f_2$	Frequency of $A_2$
(5)	$\Delta\phi$	Total phase shift calculated from (2) as $\Delta\phi = \int_t  \phi(t)  dt$
(6)	$m_A$	Median amplitude of all resonance peaks in the acoustic spectrum
(7)	$m_f$	Median frequency of all resonance peaks in the acoustic spectrum
(8)	$GDR$	Mean group delay ripple. For each descending slope in the instantaneous phase curve, group delay ripple was calculated as the maximum deviation from the corresponding linear slope (see Fig. 3, bottom graph). The feature $GDR$ was composed as the mean of all calculated group delay ripple values.

mean and unit variance according to the mean and variance of the data from PCB 2.

In order to avoid any external influences affecting the outcome of the tests, the model was trained on data from the intact PCB 2, and then tested on data from PCB 1 before and after bending. This approach ensures that the model is trained and tested on different individual components, which gives more realistic results on the performance of the model. The model was trained solely on data from pristine components

( $y = 0$ ), in which case the target labels can be considered accurate. However, the labels for the bent PCB 1 cannot be guaranteed to be fully accurate as the image inspection was done by eye, and small cracks and delaminations, in particular, can be difficult to spot. The acoustic data and target labels for PCB 2 (after bending) were also used as the basis of the analysis in a prior publication [23].

**TABLE 3.** Summary of the MLCC acoustic data set. The MLCCs on PCB 2 were used for training the OSVM model and hyperparameter optimization

	Total samples	No damage ( $y=0$ )	Damage ( $y=1$ )
PCB 1 (before bending)	60	60	0
PCB 1 (after bending)	60	23	37
PCB 2 (no bending)	60	60	0
Total	180	143	37

#### D. ONE-CLASS SUPPORT VECTOR MACHINE

As the motivation of this work was to distinguish damaged MLCCs based solely on intact examples, common supervised machine learning classifiers were unsuitable for the task. Instead, an outlier detection approach was employed using the one-class support vector machine (OSVM), which uses data from only a single class (intact capacitors) during the learning phase. Thus, the one-class SVM has been regarded as a semisupervised method [32], [33], even though the term semisupervised commonly refers to methods that use both labeled and unlabeled data [34], [35].

The OSVM [36] is a variant of the normal support vector machine (SVM), which works by fitting a hyperplane into the feature space so that it divides the data points into different categories by a largest possible margin [37]. However, with data available from only one class, the OSVM separates the data points from the origin in a high-dimensional transformed feature space constructed using a transformation  $\phi$ . The transformed data set is created from the original feature space by a kernel mapping  $\kappa$ ,

$$\kappa(x_i, x_j) = \langle \phi(x_i), \phi(x_j) \rangle \quad (5)$$

that is, the training data that the model receives are the inner products of the samples in the original feature space [36]. For this work, the widely used Radial Basis Function (Gaussian) kernel

$$\kappa(x_i, x_j) = e^{-\frac{\|x_i - x_j\|^2}{\gamma}} \quad (6)$$

was chosen, as it is typically the best-performing and even the only viable kernel for one-class problems [38]. A trained OSVM model is described by a plane in the transformed feature space, defined by the support vectors (boundary points) of the training data set. A new data point is classified by evaluating its kernel mapping with the support vectors, thus defining onto which side of the plane the point falls.

#### E. OSVM HYPERPARAMETERS

The complexity of the OSVM decision surface is controlled by two hyperparameters,  $\nu$  and  $\gamma$ . The parameter  $\nu \in ]0, 1]$  sets both the lower limit for the fraction of the support vectors out of all training samples and the upper limit for the fraction of misclassifications allowed within the training data. On the other hand,  $\gamma > 0$  controls the kernel bandwidth in (6), that is, the range of influence of the support vectors. In general, increasing  $\nu$  and  $\gamma$  result in a tighter, more complex decision boundary surrounding the target class, whereas smaller values result in a decision boundary that encloses the training data points with a wider margin.

In order to reliably detect damaged capacitors without false alarms, the hyperparameters ( $\nu, \gamma$ ) need to be properly tuned. When fitting the OSVM to data from intact MLCCs, the resulting decision surface should enclose the data points compactly enough to detect any anomalous instances. On the other hand, any new data points from the target class should fall within the decision boundary so as to avoid false alarms.

Grid search [39] is a common strategy for hyperparameter optimization: a model is trained and validated over a grid of ( $\nu, \gamma$ ) values, and the combination of parameters yielding the best classification performance is selected. However, this approach needs data from both classes, because both positive and negative samples are needed to evaluate the performance of the model. In the context of this study, this would translate into using the intact and damaged MLCC samples both for tuning the model parameters and evaluating the performance. While this could be achieved by means of nested cross-validation, this approach was not chosen as the sample size was limited, and systematic differences between test boards could be present, as discussed in section II-C.

Several methods have been proposed for optimizing the OSVM hyperparameters using data from one class only. Such methods typically apply heuristics-based rules to select the parameters or generate synthetic outliers, which can then be used to optimize the parameters using conventional techniques such as grid search [40]. Many of the proposed approaches, such as [24], [41], [42], optimize for kernel parameter  $\gamma$  only and require determining the value for  $\nu$  beforehand. Some of the more recent approaches, such as [40] and [42], rely on detecting edge patterns, that is, training samples that lie on the edge of the group data points. One such method, based on artificial outlier generation [40], was implemented and tested on the MLCC data. Although the algorithm rivals or outperforms most other algorithms on benchmark data sets, it did not yield unambiguous values for  $\nu$  and  $\gamma$  in the case of the capacitor data set. Instead, several ( $\nu, \gamma$ ) pairs with equal preference were discovered. This was likely due to a high ratio of data dimensionality and number of data points, which resulted in nearly all data points being detected as edge patterns. Because the algorithm generates one synthetic outlier per edge pattern, selecting all training data as edge patterns essentially results in overfitting the OSVM model to the training data.

## F. PROPOSED HYPERPARAMETER SELECTION ALGORITHM

To optimize the hyperparameter of the OSVM using data from the target class (intact MLCCs) only, a simple heuristic hyperparameter optimization algorithm was designed. Essentially, the algorithm performs a grid search across a plane of  $(\nu, \gamma)$  values, evaluating the performance of the OSVM at each grid point to find the optimal hyperparameters. However, in the absence of outlier data (damaged MLCCs), the model is evaluated on target class samples only. Because the training data comprises only dozens of data points, the evaluation is performed by leave-one-out cross-validation, that is, training the model on all but one sample of data, and evaluating the performance on the left-out sample. By repeating this process over each sample in the data set, the mean target class accuracy of the model can be estimated. Fig. 4 illustrates how the cross-validated target class accuracy depends on the choice of the parameters  $\nu$  and  $\gamma$ , showing a distinct “plateau” where the model reaches its maximum target class accuracy.

As discussed in Section II-E, the choice of parameters  $(\nu, \gamma)$  affects the margin between the OSVM decision surface and the training data points, as well as the complexity of the decision surface. Selecting the points  $(\nu, \gamma)$  from the middle of the “plateau” in Fig. 4 will result in a decision surface with a large margin for the training data, which translates into a high target class accuracy. Such a model will rarely, if ever, yield a false alarm on an intact component. However, if the margin between the decision surface and the training data is too large, the model will be insensitive to anomalous instances, such as small signs of mechanical damage in an acoustic signal. Conversely, selecting the hyperparameters such that the target class accuracy is low will result in a model that is oversensitive to outliers and often yields false alarms.

The fundamental premise of the proposed algorithm is that the optimal hyperparameters  $(\nu_{\text{opt}}, \gamma_{\text{opt}})$  can be found at the edge of the plateau in the hyperparameter space (see Fig. 4). By selecting such a point, 1) the cross-validated accuracy within the target class is close to 100%, and 2) even a small increase in the complexity of the decision plane results in a significant reduction in the target class accuracy. Heuristically, condition 1 ensures that the model gives very few false alarms on target class data, whereas the purpose of condition 2 is to minimize the margin between the decision boundary and the training samples, resulting in a classifier sensitive to outliers.

The algorithm<sup>1</sup> was implemented in two parts. Algorithm 1 constructs a 2D map (as in Fig. 4) of the target class accuracy  $\mathbf{A} \in \mathbb{R}^{n_{\text{grid}} \times n_{\text{grid}}}$  for the OSVM by evaluating the model over a log-spaced grid of hyperparameters  $\nu$  and  $\gamma$ . The evaluation is performed using the method of leave-one-out

cross validation, which uses as much of the data for training the model as possible. The second part, Algorithm 2, finds a “critical” point  $(\nu_c, \gamma_c)$  on the accuracy surface  $\mathbf{A}$  where the target class accuracy of the model starts falling most steeply, that is, where the downward curvature of the surface reaches its highest value. This point can be found where the Laplacian of  $\mathbf{A}$  reaches its highest negative value:

$$(\nu_c, \gamma_c) = \arg \min_{\nu, \gamma} (\nabla^2 \mathbf{A}). \quad (7)$$

In other words, the algorithm locates the sharpest part of the “cliff” on the accuracy surface, as seen in Fig. 4. Hence, the algorithm was named Cliffhanger.

In order to validate the basic principle of finding the optimal hyperparameters according to (7), the algorithm was tested on several benchmark data sets from the UCI machine learning repository. The test results indicate that such a choice of hyperparameters indeed generally yields classification performance on a par with other hyperparameter selection techniques, with a more in-depth analysis provided in Appendix. However, the good overall performance of the algorithm was achieved at the cost of a number of false alarms because the target class accuracy of the model at  $(\nu_c, \gamma_c)$  did not reach 100%. In some applications, such as detecting damaged MLCCs, avoiding false alarms should be prioritized. For such tasks, an optional threshold condition was imposed on the selection of  $\nu$  and  $\gamma$ . When using the threshold, Algorithm 2 checks whether the cross-validated accuracy at  $(\nu_c, \gamma_c)$  is above a given threshold value  $T$ . If the condition is not satisfied, the algorithm locates the point  $(\nu, \gamma)$  closest to  $(\nu_c, \gamma_c)$  in terms of grid coordinates such that the cross-validated accuracy at  $(\nu, \gamma)$  is exceeded. For this study, a strict threshold value of

$$T = \max(\mathbf{A}) \quad (8)$$

was imposed. Such a condition was chosen because in the case of detecting faulty components, false alarms can be considered more costly than false negative results. If a false alarm from a single component results in the rejection of the entire device, the ratio of false alarms should be kept as low as possible. It was also experimentally verified that by using the threshold  $T$  instead of  $(\nu_c, \gamma_c)$  yielded significantly less false alarms on pristine MLCCs.

After finding the values for  $\nu_{\text{opt}}$  and  $\gamma_{\text{opt}}$ , the output value for  $\nu_{\text{opt}}$  in Algorithm 2 is scaled by a factor of  $1 - 1/N$ . This is done because the parameter  $\nu$  sets the minimum fraction of how many data points within the training set are used as support vectors. As the cross-validation results in Algorithm 1 are obtained with training sets of  $N - 1$  points each, the final value for  $\nu_{\text{opt}}$  must be rescaled for training data of  $N$  points. After optimizing the hyperparameters using Algorithms 1 and 2, the final OSVM model is trained using the full data set.

The functionality of the Cliffhanger algorithm was verified against other OSVM hyperparameter optimization methods on six commonly used data sets from the UCI machine

<sup>1</sup>Note that in this study, damaged MLCC samples (outliers) were denoted by the label 1, which is to be understood as a positive test result. However, literature on OSVM algorithms commonly refers to the target class samples as 1 and outliers as 0. The results for the benchmark data sets follow the latter convention.

learning repository, with the results listed in Appendix. The algorithm was evaluated both with the threshold (8) (Cliffhanger-T), and without it (Cliffhanger). Based on the results, Cliffhanger generally performs on a par with the reference methods, whereas Cliffhanger-T yields significantly fewer false alarms at the cost of overall performance. However, Cliffhanger-T was selected for this study, as avoiding false alarms is of high priority. While the proposed algorithm has a high computational complexity owing to the combination of grid search and cross-validation, the results in Appendix indicate that it is suitable for situations where the number of samples is low and the ratio  $D/N$  is high.

---

**Algorithm 1**  $(\nu, \gamma)$ -performance surface mapping

---

**Require:** Input data matrix  $\mathbf{X} = (\mathbf{x}_1 \dots \mathbf{x}_n)^T \in \mathbb{R}^{N \times D}$  (intact MLCCs)  
*#Set parameters for grid mapping*  
Set  $n_{\text{grid}} \leftarrow 20$   
Set log-spaced range of  $n_{\text{grid}}$  points  $\nu \leftarrow \{10^{-2} \dots 10^0\}$   
Set log-spaced range of  $n_{\text{grid}}$  points  $\gamma \leftarrow \{10^{-3} \dots 10^2\}$   
Preallocate accuracy matrix  $\mathbf{A} = (a_{i,j}) \in \mathbb{R}^{n_{\text{grid}} \times n_{\text{grid}}}$   
*#Partition data for leave-one-out cross-validation*  
**for**  $n = 1$  to  $N$  **do**  
*#Perform grid mapping over hyperparameter space using partitioned data*  
Set  $(\mathbf{X}_{\text{train}}, \mathbf{Y}_{\text{train}}) = (\mathbf{X} \setminus \{\mathbf{x}_n\}, \mathbf{0}^{(N-1) \times 1})$   
Set  $(\mathbf{X}_{\text{test}}, \mathbf{Y}_{\text{test}}) = (\mathbf{x}_n, 0)$   
**for**  $i = 1$  to  $n_{\text{grid}}$  **do**  
**for**  $j = 1$  to  $n_{\text{grid}}$  **do**  
Train one-class SVM( $\nu_i, \gamma_j$ ) on  $(\mathbf{X}_{\text{train}}, \mathbf{Y}_{\text{train}})$   
Evaluate the SVM on  $(\mathbf{X}_{\text{test}}, \mathbf{Y}_{\text{test}})$   
Calculate evaluation accuracy  $acc_{\nu, \gamma}$   
Update  $a_{i,j} \leftarrow a_{i,j} + acc_{\nu, \gamma}$   
**end for**  
**end for**  
**end for**  
**return**  $(1/N) \cdot \mathbf{A}$

---



---

**Algorithm 2** Hyperparameter selection

---

**Require:** Accuracy matrix  $\mathbf{A} = (a_{i,j})$   
**Require:** Hyperparameter grid  $(\nu, \gamma)$   
**Require:** Threshold switch  $s \in \{\text{True}, \text{False}\}$   
**Require:** Threshold value  $T$   
Calculate discrete Laplacian  $\nabla^2 \mathbf{A}$   
Find grid coordinates  $(i_c, j_c) \leftarrow \arg \min_{i,j} (\nabla^2 \mathbf{A})$   
Set critical point  $(\nu_c, \gamma_c) = (\nu(i_c), \gamma(j_c))$   
**if**  $s = \text{False}$  **or**  $\mathbf{A}(i_c, j_c) \geq T$  **then**  
Set  $(\nu_{\text{opt}}, \gamma_{\text{opt}}) \leftarrow (\nu_c, \gamma_c)$   
**else**  
Set  $(\nu_{\text{opt}}, \gamma_{\text{opt}}) \leftarrow \arg \min_{(i,j) \in \arg \max \mathbf{A}} \|(i, j) - (i_c, j_c)\|_2$   
**end if**  
**return**  $((1 - 1/N)\nu_{\text{opt}}, \gamma_{\text{opt}})$

---

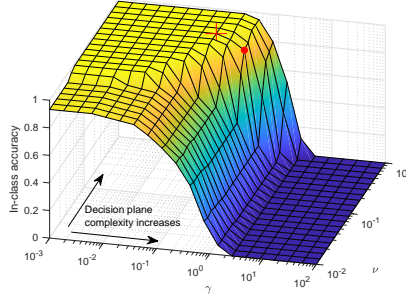


**FIGURE 4.** Hyperparameters were optimized by mapping the target class accuracy of the OSVM model across a grid of points. At each point, the in-class accuracy of the model was computed using leave-one-out cross-validation. The red dot marks the critical point with the steepest downward curvature in accuracy, defined as the minimum of the Laplacian of the performance plane. The red cross indicates the point of optimal hyperparameters, defined as the point closest to the critical point where the mean accuracy reaches its maximum value, that is, no false alarms are triggered within the training data.

## G. EVALUATION METHODS

After optimizing the hyperparameters and training the OSVM on intact capacitors from PCB 2, its classification performance was tested on measurements from PCB 1 both before and after bending. The performance of the model was evaluated using a confusion matrix, which is a common tool for visualizing the output of a classifier model as

$$\begin{array}{c} \text{Outputs} \\ \begin{pmatrix} \text{TP} & \text{FP} \\ \text{FN} & \text{TN} \end{pmatrix} \end{array} \quad (9)$$

$$\begin{array}{c} 1 \quad 0 \\ \text{Targets} \end{array}$$

where TP = True Positive (damaged), FP = False Positive, FN = False Negative, and TN = True Negative (intact). When evaluating the model on intact components only, accuracy (correct outputs/incorrect outputs) was used as the main evaluation metric. When both damaged and nondamaged components were present, precision, recall, and Matthews Correlation Coefficient (MCC) were used as the indicators of performance. In short, precision describes how many of the positive outputs (alarms) are relevant, whereas recall tells how many of the positive samples were discovered by the model. MCC can be seen as a balanced performance score, which accounts for the relative frequencies of each category in the data. Precision, recall, and MCC can be calculated from the data in the confusion matrix as



$$\begin{aligned}
\text{Precision} &\in [0, 1] = \frac{TP}{TP + FP} \\
\text{Recall} &\in [0, 1] = \frac{TP}{TP + FN} \\
\text{MCC} &\in [-1, 1] = \frac{TP \cdot TN - FP \cdot FN}{\sqrt{(TP + FP)(TP + FN)(TN + FP)(TN + FN)}}
\end{aligned} \quad (10)$$

In addition to the metrics derived from the confusion matrix, the performance of the model was evaluated using the Receiver Operating Characteristic (ROC) graph, along with the Area-Under-Curve value (AUC-ROC) [43].

### III. RESULTS

After extracting the features in Table 2 and composing the data set according to Table 3, the classification performance of the OSVM was evaluated for two objectives: to discover damaged MLCCs and to avoid false alarms on undamaged capacitors. To this end, the data were divided into training and testing sets based on how the components populated the test PCBs. The data from intact PCB 2 were used for optimizing the hyperparameters using Cliffhanger (Algorithms 1 and 2), after which the OSVM was trained on the same data. The model was then tested on two separate groups of data: intact MLCCs from PCB 1 before the bending procedure, and the same components after the PCB had undergone the bending. This approach was chosen over more commonly used cross-validation techniques, such as the k-fold cross-validation, for two reasons. First, each PCB underwent the acoustic measurements on different occasions, which might translate into data bias even between two sets of intact capacitors, as discussed in Section II-C. Secondly, because the data originated from only two PCBs (PCB 1 was measured twice), this approach allowed for conducting the training and evaluation process for the damaged MLCCs on different individual components, as opposed to using components from PCB 1 for both training and testing the model, potentially causing data leakage.

Ideally, the model should not be able to distinguish the pristine components on PCB 1 from those on PCB 2, whereas components on PCB 1 damaged in the bending process should be detected by their anomalous acoustic signatures. Furthermore, in order to find out which features in the acoustic signal are reliable indicators of damage without being sensitive to changes between intact components, the OSVM was tested on several combinations of features, grouped according to the physical quantity (amplitude, frequency, phase) they represent.

Test results for components from PCB 1 before and after bending are shown in Table 4. The results on intact MLCCs (PCB 1, before bending) show that by using amplitude- and frequency-related information, the model sees little difference between intact components on PCB 1 and those within the training set (PCB 2). However, the inclusion of frequency-related features consistently yielded a significant

number of false alarms, making them unfit for the fault detection application using the current experimental setup. However, this does not necessarily mean that the frequency-related features do not carry information about the condition of the component, as the result could be explained by how the frequency-related features are extracted from the peaks in the acoustic signal.

The results for MLCCs on PCB 1 after bending show that the model is able to discover the majority of the damaged capacitors, except when using only frequency-related features. The best classification performance in terms of accuracy, recall, and MCC is obtained using the combination of all eight features, which, however, results in a high error rate on pristine MLCCs. For all feature combinations, the model yields significantly more false alarms on data from PCB 1 after bending compared to pre-bending data, even though the data originate from the same components. This might result from failing to notice some signs of damage during the optical inspection, while another explanation is that the structure of some of the components was affected by the bending procedure, while not resulting in actual damage.

To summarize the results, the model outputs for data before and after the bending procedure were combined. Using MCC as the indicator of performance, the best results were obtained by using amplitude-related features only. The combination of amplitude and phase yielded a higher recall rate than amplitude alone, while also giving more false alarms on the bent PCB. The addition of phase information may have actually led to discovering damaged capacitors on the bent board, which were left undetected during the optical inspection. As the goal would be to avoid false alarms as much as possible while maintaining a decent recall rate, the best feature combinations would thus be either amplitude only, or amplitude combined with phase information. The ROC graphs for the model in Fig. 5 also show that amplitude, phase, and the combination of the two clearly dominate over the rest of the feature combinations in terms of classification performance, further confirmed by the AUC-ROC scores in Table 4.

The results on amplitude-based features were selected for further analysis due to the highest MCC score on the combined data and good precision on the bent PCB 1, even though the combination of amplitude and phase reached the highest AUC-ROC score. Confusion matrices based on amplitude-based input features in Fig. 6 show that the model fails to detect nine out of 37 damaged MLCCs, while yielding six false alarms. However, only two false alarms are given on the pre-bending data even though the same individual components are in question.

In order to shed more light on the misclassified MLCC samples, the data set was visualized using the t-distributed Stochastic Neighborhood Embedding (t-SNE) algorithm [44]. The algorithm embeds the original, high-dimensional data in a 2-D presentation while attempting to retain the structure of the data set such that the neighboring points in the original space are also close to each other in the

Input features	(feat.#)	PCB 1, before bending	PCB 1, after bending				Before & after combined	
		Accuracy (%)	Accuracy (%)	Precision	Recall	MCC	MCC	AUC-ROC
Amplitude	(1,2,6)	96.67	75.00	0.8235	0.7567	0.4865	<b>0.6655</b>	0.8574
Frequency	(3,4,7)	30.00	43.33	0.8000	0.1081	0.1137	-0.3879	0.2318
Phase	(5,8)	<b>98.33</b>	68.33	0.7364	0.7568	0.3248	0.6155	0.8460
Amplitude + Freq	(1,2,3,4,6,7)	43.33	78.33	<b>0.8333</b>	0.8108	0.5458	0.3081	0.6724
Amplitude + Phase	(1,2,5,6,8)	96.67	73.33	0.7692	0.8108	0.4276	0.6605	<b>0.9049</b>
Freq + Phase	(3,4,5,7,8)	23.33	61.67	0.7059	0.6487	0.2098	-0.0255	0.4865
All	(1-8)	51.67	<b>80.00</b>	0.8205	<b>0.8649</b>	<b>0.5714</b>	0.4018	0.6923

**TABLE 4.** OSVM classification results using various performance metrics. Hyperparameter optimization and model training was performed on components from another circuit board (PCB 2). The optimization-training-process was repeated separately on various combinations of input features, which were grouped according to the physical quantity (amplitude, frequency, phase) they represent. The ROC graphs for the combined before/after data are shown in Fig. 5.

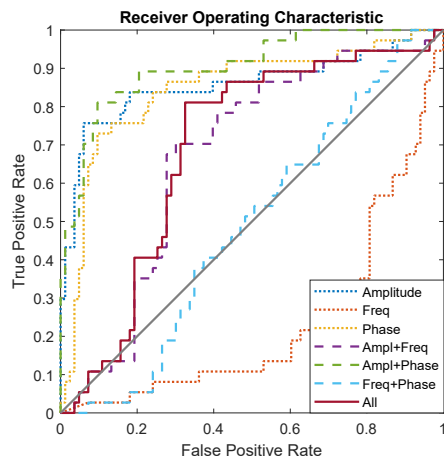


**FIGURE 5.** ROC graph describing the performance of the OSVM model using different feature groups on the combination of data from before and after bending PCB 1. The Area-Under-Curve scores are listed in Table 4.

Before bending		After bending	
Output Class	Target Class	Output Class	Target Class
	0		0
0	58 96.7%	17 28.3%	15.0%
1	2 3.3%	6 10.0%	17.6%
	96.7% 3.3%		73.9% 26.1%
	NaN% NaN%		75.7% 24.3%
	96.7% 3.3%		82.4% 17.6%
	NaN% NaN%		75.0% 25.0%

(a) PCB 1, before bending

(b) PCB 1, after bending

**FIGURE 6.** Confusion matrices for PCB 1 before and after bending the circuit board. The model was trained using only amplitude-related features, as this feature set yielded the highest MCC score on the combination of pre- and post-bending data. Class 1 = damaged component, class 0 = no damage.

2D embedding. The t-SNE visualization of the entire data set is shown in Fig. 7 along with the OSVM classification

results from Fig. 6b. The majority of the capacitors labeled as damaged constitute a cluster separate from the intact samples, suggesting that mechanical damage affects the acoustic signature of an MLCC in a consistent manner. The way in which the OSVM specifically classifies the capacitors in this cluster as anomalous further supports this observation. However, five or six samples within this cluster appear to be false positives. In contrast, seven to ten out of 37 samples labeled as "damaged" are misclassified by the OSVM, and the majority of these samples appear to lie well within the group of intact capacitor samples.

Given that the capacitors were manually labeled by visually inspecting the cross-sectional and X-ray images, it is likely that some damage was left unseen. In contrast, artifacts such as scratches in the epoxy may have led to labeling of some undamaged MLCCs as damaged. To further verify the inspection results, the cross-sectional images from the six false positive and nine false negative samples in Fig. 6b were reinspected. Two false positive samples indeed showed a small crack in the lower corner of the capacitor body, and two others showed potential signs of delamination between the end termination and the solder joint. As for the false negatives, only two out of seven definitely showed cracks, and these findings were also confirmed by X-ray. Possible small cracks were seen in three other samples, and the cracks observed previously in the rest of the samples were probably scratches in the epoxy surface of the cross-section samples. Considering these reinspection results, there is a possibility that four out of six false positives were actually true positives, and four out of nine false negatives were actually true negatives. If the labels were to be corrected according to the reinspection, the model would reach 88.3% accuracy, 86.5% recall, and 94.1% precision on the bent PCB 1 according to the confusion matrix in Fig. 8. However, the outcomes in the original confusion matrix in Fig. 6b are reported as the final results.

#### IV. DISCUSSION

Acoustic characterization is a promising method for non-destructive testing of MLCCs, especially because it can be performed on soldered components on assembled circuit boards. However, in order to generalize the method to capac-

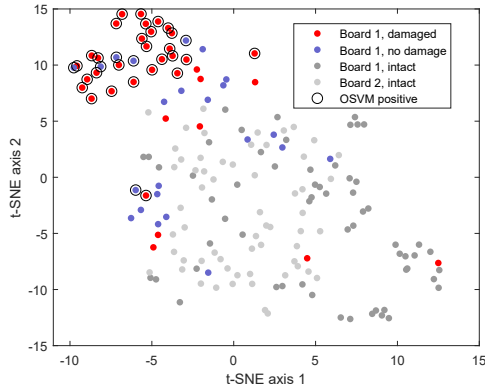


**FIGURE 7.** t-SNE visualization of the acoustic data set, showing the eight-dimensional data embedded in two dimensions. MLCCs from intact PCBs 1 and 2 are indicated by gray, whereas the red and blue markers indicate the microsectioning and X-ray inspection results for the capacitors on the bent PCB 1. The ring symbols indicate the capacitors marked by the OSVM (using amplitude features only) as anomalous.

		After bending (CORRECTED LABELS)		
Output Class	0	21 35.0%	5 8.3%	80.8% 19.2%
	1	2 3.3%	32 53.3%	94.1% 5.9%
		91.3% 8.7%	86.5% 13.5%	88.3% 11.7%
		Target Class		

**FIGURE 8.** Confusion matrix for bent PCB 1 after correcting the target labels (four false positives and four false negatives) according to cross-sectional and X-ray data. The model was trained using only amplitude-related features.

itors of various sizes and capacitances, it should be possible to detect damaged components based on pristine examples only. The results of this study show that by using a one-class SVM in conjunction with the proposed combination of preprocessing, feature extraction, and hyperparameter optimization, 75–80% of damaged MLCCs can be detected, while maintaining a false detection rate below 4% on pristine components. However, the performance values on damaged capacitors contain some uncertainty, as the reinspection of the component samples revealed that eight out of fifteen misclassified capacitors were actually mislabeled. Thus, the method can be expected to reach a detection rate of over 90% if a larger data set with more accurate labels is available. Nevertheless, the classification results are in good agreement with the way the data are clustered in the t-SNE visualization.

While the model should be sensitive enough to reveal damaged components, a low ratio of false alarms should be prioritized over a high ratio of true positives. As the number of capacitors per device can be high, false alarms can become

very costly, whereas the occurrence of faulty components in a real-life situation is much lower than in this study. Given these requirements, the introduced Cliffhanger hyperparameter optimization algorithm performs successfully in selecting the parameters of the OSVM. Even though the false alarms rate of approx. 4% can still be considered too high for production line screening, this number can be decreased by introducing more intact samples in the training data. The results of this study also highlight the importance of feature extraction: while the best detection rate on the bent PCB was achieved by using the full feature set, the misclassification rate on the intact PCB was also over 50%. This result can be explained by the way in which the feature values are distributed: even though some acoustic features may be strongly correlated with structural damage in MLCCs, intrinsic deviations in the physical parameters of the components and environmental factors will cause feature values from two difference populations of intact components to overlap. By appropriate feature selection, a nonoverlapping region between the two classes can be found.

This study built upon prior research [23], where the use of resonant frequencies  $A_1$  and  $A_2$  was evaluated as input features for an ordinary two-class SVM, reporting an accuracy of 78.3%. Because the study was only performed on capacitors on a single bent PCB assembly (PCB 1), no information of the performance on pristine capacitors is available from the study. Nevertheless, the classification performance of the one-class SVM on the bent PCB 1 is similar to that of the binary SVM in [23], while the OSVM maintains a low false alarm rate on the same exact components prior to PCB bending. While these observations confirm that the proposed feature extraction and hyperparameter optimization methods are applicable for the task of detecting faulty MLCCs, they also further suggest that the performance results may be at least partially limited by the labeling process.

A comprehensive comparison with other proposed damage detection approaches is difficult as there is only limited information available on the accuracy of the other methods. However, the insulation resistance measurement, a common quality assurance tool, is typically capable of revealing only a minority of cracks [4]. The electromechanical resonance spectrum measurement [19] has been suggested to be an accurate method for larger cracks, but less sensitive for instance to small thermal cracks, and it is also affected by the prehistory of the component [4]. Furthermore, the method might be impractical for production PCB assemblies, as it requires electrical measurements, which are easily affected by other components on the assembly. In contrast, the acoustic method used in this study can be isolated to a single capacitor even if there are parallel components on the path of the excitation signal, given that the excitation voltage source has a sufficiently low source impedance.

While the proposed method performs successfully in detecting damaged MLCCs, the accuracy should be verified and improved using a larger number of capacitors. Even though this study was performed on capacitors of only a



single case size, prior studies [22], [23], [28] have shown that MLCCs of other case sizes exhibit similar changes in acoustic behavior when mechanically damaged, suggesting that the method should be applicable to other case sizes as well. Moreover, the higher amplitude of acoustic emissions observed in smaller case sizes [22] will likely result in a better signal-to-noise ratio, making the acoustic identification of damage easier for smaller MLCCs. However, validating this method on MLCCs of other case sizes and capacitances is a matter of further study. In addition, component sample misclassifications should be reduced by incorporating other labeling methods, such as the C-scan ultrasonic microscopy. On the other hand, the performance may vary with different capacitor sizes as well as types and degrees of physical damage, and thus, further study is required. Nonetheless, the proposed method performs well and could be a valuable tool for end-of-line testing of PCB assemblies with large MLCCs, which are especially prone to flex cracking. As the experiments were performed on data from custom-built test boards, the method should also be tested on a production PCB assembly.

## V. CONCLUSION

Cracks and delaminations in MLCCs related to soldering, PCB assembly, and handling remain problematic, as there are no commonly used tools for fast and reliable screening for these types of damage. In this work, an acoustic nondestructive testing method for MLCCs was demonstrated on assembled PCBs. For detecting damaged or anomalous capacitors, the method employs a one-class support vector machine, a machine learning model trained solely on pristine capacitor examples. Furthermore, an algorithm for optimizing the hyperparameters of the model is presented.

First, acoustic measurement data from MLCCs was obtained from a prior study. The data contained measurements from 120 intact capacitors on two test PCBs, and another 60 measurements after one of the boards was subjected to controlled bending. The measurement data were preprocessed and composed into a data set, with each bent sample labeled as damaged or nondamaged according to cross-sectional and X-ray images. An OSVM model was then optimized and trained on data from intact capacitors on one PCB, and the classification accuracy was tested with MLCCs from another PCB before and after bending. The results show that through proper feature engineering and hyperparameter optimization, the model is capable of successfully identifying damaged MLCCs with dozens of intact capacitors as training data, while maintaining a low rate of false alarms on pristine capacitors.

## REFERENCES

- [1] R. Randoll, W. Wondrak, and A. Schletz, "Lifetime and manufacturability of integrated power electronics," *Microelectronics Reliability*, vol. 64, pp. 513 – 518, 2016, proceedings of the 27th European Symposium on Reliability of Electron Devices, Failure Physics and Analysis. [Online]. Available: <http://www.sciencedirect.com/science/article/pii/S0026271416301767>
- [2] B. Sood. (2013, Mar) Root cause failure analysis of electronics. University of Maryland. [Online]. Available: [https://www.smta.org/chapters/files/Philadelphia\\_SMTA\\_Philly\\_Rev2.pdf](https://www.smta.org/chapters/files/Philadelphia_SMTA_Philly_Rev2.pdf)
- [3] J. Ho, T. R. Jow, and S. Boggs, "Historical introduction to capacitor technology," *IEEE Electrical Insulation Magazine*, vol. 26, no. 1, pp. 20–25, January 2010.
- [4] A. Teverovsky, "Cracking problems in low-voltage chip ceramic capacitors," NASA, techreport GSFC-E-DAA-TN65668, Mar 2018. [Online]. Available: <https://ntrs.nasa.gov/archive/nasa/casi.ntrs.nasa.gov/20190001592.pdf>
- [5] D. Brown, "Oxygen vacancy migration in mlccs," in 2018 Pan Pacific Microelectronics Symposium (Pan Pacific), Feb 2018, pp. 1–6.
- [6] J. A. Ahmar and S. Wiese, "A finite element modelling and fracture mechanical approach of multilayer ceramic capacitors," in 16th International Conference on Thermal, Mechanical and Multi-Physics Simulation and Experiments in Microelectronics and Microsystems, 2015.
- [7] M. Keimasi, M. H. Azarian, and M. G. Pecht, "Flex cracking of multilayer ceramic capacitors assembled with pb-free and tin-lead solders," *IEEE Transactions on Device and Materials Reliability*, vol. 8, no. 1, pp. 182–192, March 2008.
- [8] D. Han, "Material Shortage & Price Trend," Silecta Inc., 206-308 Leggett Drive, Kanata, Ontario, Canada, techreport, Feb. 2018, accessed: 2019-02-22. [Online]. Available: <https://lyticafasttrack.files.wordpress.com/2018/03/material-shortage-price-trend-report.pdf>
- [9] D. M. Zogbi, "MLCC Shortages by Case Size: 2018," tti Inc., techreport, Jan. 2018, accessed: 2019-02-22. [Online]. Available: <https://www.ttiinc.com/content/ttiinc/en/resources/marketeye/categories/passives/me-zogbi-20180930.html>
- [10] C. Andersson, O. Kristensen, E. Varescon, and F. Iannuzzo, "Impact of bending speed and setup on flex cracks in multilayer ceramic capacitors," in 2017 IEEE 11th International Symposium on Diagnostics for Electrical Machines, Power Electronics and Drives (SDEMPED), Aug 2017, pp. 608–614.
- [11] S. R. Kahn and R. W. Checkaneck, "Acoustic emission testing of multilayer ceramic capacitors," *IEEE Transactions on Components, Hybrids and Manufacturing Technology*, 1983.
- [12] C. Andersson, O. Kristensen, S. Miller, T. Gloor, and F. Iannuzzo, "Lock-in thermography failure detection on multilayer ceramic capacitors after flex cracking and temperature-humidity-bias stress," *IEEE Journal of Emerging and Selected Topics in Power Electronics*, vol. 6, no. 4, pp. 2254–2261, Dec 2018.
- [13] D. N. Donahoe, M. Pecht, I. K. Lloyd, and S. Ganesan, "Moisture induced degradation of multilayer ceramic capacitors," *Microelectronics Reliability*, vol. 46, no. 2, pp. 400 – 408, 2006. [Online]. Available: <http://www.sciencedirect.com/science/article/pii/S0026271405001022>
- [14] T. Adams, "Preventing MLCC failures," *Circuits Assembly*, Aug 2009. [Online]. Available: <http://www.sonoscanchina.cn/us/images/Preventing-MLCC-Failures-Circuits-Assembly-August-09.pdf>
- [15] G. Vogel, "Analytical tool for a reliable failure analysis and guideline for positioning cercaps on pcbs," *Microelectronics Reliability*, 2015.
- [16] C. Andersson, J. Ingman, E. Varescon, and M. Kiviniemi, "Detection of cracks in multilayer ceramic capacitors by x-ray imaging," *Microelectronics Reliability*, 2016.
- [17] J. Ingman, J. Jormanainen, A. Vulli, J. Ingman, K. Maula, T. J. Kärkkäinen, and P. Silventoinen, "Localization of dielectric breakdown defects in multilayer ceramic capacitors using 3d x-ray imaging," *Journal of the European Ceramic Society*, vol. 39, no. 4, pp. 1178 – 1185, 2019. [Online]. Available: <http://www.sciencedirect.com/science/article/pii/S0955221918306617>
- [18] B.-H. Ko, S.-G. Jeong, Y.-G. Ahn, K.-S. Park, N.-C. Park, and Y.-P. Park, "Analysis of the correlation between acoustic noise and vibration generated by a multi-layer ceramic capacitor," *Microsystem Technologies*, vol. 20, no. 8, pp. 1671–1677, Aug 2014. [Online]. Available: <https://doi.org/10.1007/s00542-014-2209-5>
- [19] L. Bechou, S. Mejdji, Y. Ousten, and Y. Danto, "Non-destructive detection and localization of defects in multilayer ceramic chip capacitors using electromechanical resonances," *Quality and reliability engineering international*, 1996.
- [20] W. L. Johnson, S. A. Kim, G. S. White, and J. Herzberger, "Nonlinear resonant acoustic detection of cracks in multilayer ceramic capacitors," in 2014 IEEE International Ultrasonics Symposium, Sept 2014, pp. 244–247.
- [21] W. I. Johnson, J. L. Herzberger, S. A. Kim, K. L. Peterson, P. R. Heytler, and G. S. White, "Resonant acoustic frequency shifts associated with

- cracks in multilayer ceramic capacitors," IEEE Transactions on Device and Materials Reliability, vol. PP, no. 99, pp. 1–1, 2017.
- [22] S. Levikari, T. J. Kärkkäinen, C. Andersson, J. Tamminen, and P. Silventoinen, "Acoustic Phenomena in Damaged Ceramic Capacitors," IEEE Transactions on Industrial Electronics, 2018.
- [23] S. Levikari, T. J. Kärkkäinen, C. Andersson, J. Tamminen, and P. Silventoinen, "Acoustic detection of cracks and delamination in multilayer ceramic capacitors," IEEE Transactions on Industry Applications, vol. 55, no. 2, pp. 1787–1794, March 2019.
- [24] A. Anaissi, N. L. D. Khoa, and Y. Wang, "Automated parameter tuning in one-class support vector machine: an application for damage detection," International Journal of Data Science and Analytics, vol. 6, pp. 311–325, 2018. [Online]. Available: <https://doi.org/10.1007/s41060-018-0151-9>
- [25] S. Das, A. N. Srivastava, and A. Chattopadhyay, "Classification of damage signatures in composite plates using one-class svms," in 2007 IEEE Aerospace Conference, 2007, pp. 1–19. [Online]. Available: <https://doi.org/10.1109/AERO.2007.352912>
- [26] K. Yan, Z. Ji, and W. Shen, "Online fault detection methods for chillers combining extended kalman filter and recursive one-class svm," Neurocomputing, vol. 228, pp. 205 – 212, 2017, advanced Intelligent Computing: Theory and Applications. [Online]. Available: <http://www.sciencedirect.com/science/article/pii/S0925232126312528>
- [27] B. Mun, M. Lim, and S. Bae, "Condition monitoring scheme via one-class support vector machine and multivariate control charts," Journal of Mechanical Science and Technology, 2020.
- [28] S. Levikari, "Detection of Cracks – Acoustic Experiments on Multilayer Ceramic Capacitors," Master's thesis, Lappeenranta University of Technology, Lappeenranta, Finland, 2018.
- [29] S. W. Smith, The Scientist and Engineer's Guide to Digital Signal Processing. California Technical Publishing, 1997. [Online]. Available: <http://www.dspguide.com/ch18/1.htm>
- [30] Y. Hoshen, R. J. Weiss, and K. W. Wilson, "Speech acoustic modeling from raw multichannel waveforms," in 2015 IEEE International Conference on Acoustics, Speech and Signal Processing (ICASSP), 2015, pp. 4624–4628.
- [31] G. Dougherty, Pattern Recognition and Classification: An Introduction, 1st ed. Springer, 2013.
- [32] V. Hodge and J. Austin, "A Survey of Outlier Detection Methodologies," Artificial Intelligence Review, vol. 22, pp. 85–126, Oct 2004. [Online]. Available: <https://doi.org/10.1007/s10462-004-4304-y>
- [33] V. Chandola, A. Banerjee, and V. Kumar, "Anomaly detection: A survey," ACM Comput. Surv., vol. 41, no. 3, Jul. 2009. [Online]. Available: <https://doi.org/10.1145/1541880.1541882>
- [34] X. Zhu and A. B. Goldberg, Introduction to Semi-Supervised Learning. Morgan and Claypool, 2009. [Online]. Available: <https://doi.org/10.2200/S00196ED1V01Y200906AIM006>
- [35] I. Triguero, S. García, and F. Herrera, "Self-labeled techniques for semi-supervised learning: taxonomy, software and empirical study," Knowledge and Information Systems, vol. 42, pp. 245–284, 2013. [Online]. Available: <https://doi.org/10.1007/s10115-013-0706-y>
- [36] B. Schölkopf, J. C. Platt, J. Shawe-Taylor, A. J. Smola, and R. C. Williamson, "Estimating the support of a high-dimensional distribution," Neural Computation, vol. 13, no. 7, pp. 1443–1471, July 2001.
- [37] C. Cortes and V. Vapnik, "Support-vector networks," Machine Learning, vol. 20, no. 3, pp. 273–297, Sep 1995. [Online]. Available: <https://doi.org/10.1007/BF00994018>
- [38] A. Bounsiar and M. G. Madden, "Kernels for one-class support vector machines," in 2014 International Conference on Information Science Applications (ICISA), 2014, pp. 1–4.
- [39] I. Goodfellow, Y. Bengio, and A. Courville, Deep Learning. MIT Press, 2016, <http://www.deeplearningbook.org>.
- [40] S. Wang, Q. Liu, E. Zhu, F. Porikli, and J. Yin, "Hyperparameter selection of one-class support vector machine by self-adaptive data shifting," Pattern Recognition, vol. 74, pp. 198 – 211, 2018. [Online]. Available: <http://www.sciencedirect.com/science/article/pii/S0031320317303564>
- [41] R. Unnthorsson, R. T. Runarsson, and T. M. Johnson, "Model selection in one class nu-svms using rbf kernels," in 16th conference on Condition Monitoring and Diagnostic Engineering Management, 2003. [Online]. Available: <https://web.archive.org/web/20070207080622/http://www.hi.is/~runson/svm/paper.pdf>
- [42] Y. Xiao, H. Wang, and W. Xu, "Parameter selection of gaussian kernel for one-class svm," IEEE Transactions on Cybernetics, vol. 45, no. 5, pp. 941–953, May 2015.
- [43] T. Fawcett, "Roc graphs: Notes and practical considerations for researchers," HP Laboratories, Tech. Rep., 2004.
- [44] L. van der Maaten and G. Hinton, "Visualizing data using t-sne," Journal of Machine Learning Research, vol. 9, Nov. 2008. [Online]. Available: <http://jmlr.org/papers/volume9/vandermaaten08a/vandermaaten08a.pdf>
- [45] S. Wang, J. Yu, E. Lapira, and J. Lee, "A modified support vector data description based novelty detection approach for machinery components," Applied Soft Computing, vol. 13, no. 2, pp. 1193 – 1205, 2013. [Online]. Available: <http://www.sciencedirect.com/science/article/pii/S1568494612004899>
- [46] H. Deng and R. Xu, "Model selection for anomaly detection in wireless ad hoc networks," in 2007 IEEE Symposium on Computational Intelligence and Data Mining, 2007, pp. 540–546.
- [47] P. F. Evangelista, M. J. Embrechts, and B. K. Szymanski, "Some properties of the gaussian kernel for one class learning," in Artificial Neural Networks – ICANN 2007, J. M. de Sá, L. A. Alexandre, W. Duch, and D. Mandic, Eds. Berlin, Heidelberg: Springer Berlin Heidelberg, 2007, pp. 269–278.
- [48] S. Khazai, S. Homayouni, A. Safari, and B. Mojaradi, "Anomaly detection in hyperspectral images based on an adaptive support vector method," IEEE Geoscience and Remote Sensing Letters, vol. 8, no. 4, pp. 646–650, 2011.

## APPENDIX. TEST RESULTS ON UCI MACHINE LEARNING DATA SETS

The proposed hyperparameter selection algorithm was tested on eight commonly used data sets from the UCI machine learning repository<sup>2</sup>: Breast Cancer Wisconsin (Diagnostic), Heart Disease, Pima Indians Diabetes, Connectionist Bench (Sonar, Mines vs. Rocks), Wine, Glass Identification, Statlog (Vehicle Silhouettes), and Connectionist Bench (Vowel Recognition - Deterding Data). The data sets have previously been used for testing one-class support vector machine hyperparameter optimization in [24] and [42], and a summary of the data sets is shown in Table 5.

The performance of the proposed algorithm was compared against other hyperparameter optimization algorithms, following the procedure in [42]. The data sets were first preprocessed by removing rows with missing values, as well as removing all-constant columns. The feature variables were then standardized to zero mean and unit variance. For each data set, the target class was selected as in [42], and randomly selected 80% of the target samples were used for hyperparameter optimization and training the model. The model was then tested on the outlier instances, plus the remaining 20% of the target data. As in [42], the evaluation process was repeated 20 times, randomly partitioning the target data each time. The performance of the model was evaluated using the geometric mean (G-mean) of True Positive Rate (TPR, i.e., Recall) and True Negative Rate (TNR)

$$G\text{-mean} = \sqrt{TPR \cdot TNR} \quad (11)$$

The G-mean scores of the Cliffhanger algorithm were compared against those of five other algorithms, as reported in [42]: MIES [42], Min#SV+MaxL (MSML) [45], SKEW [46], VM [47] and MD [48]. Two versions of the Cliffhanger algorithm are compared with the reference methods: Cliffhanger, which selects the point  $(\nu_c, \gamma_c)$  as the optimum hyperparameters; and Cliffhanger-T, the version used for the MLCC data which imposes an additional condition  $(\nu, \gamma) \in \arg \max \mathbf{A}$  for the hyperparameters. The performance of these algorithms in terms of the G-mean score,

<sup>2</sup><https://archive.ics.uci.edu/ml/datasets.php>

Data set	Dimensions	Targets	Outliers
Cancer	9	458	241
Heart	13	164	139
Diabetes	8	500	268
Sonar	60	111	97
Wine	13	48	130
Glass	9	70	144
Vehicle	18	199	647
Vowel	10	48	480

TABLE 5. UCI ML repository data sets

as reported in [42] is listed in Table 6. To highlight the differences between Cliffhanger and the thresholded version, Cliffhanger-T, the raw confusion matrix elements (refer to (9)) are given in Table 7.

The results in Table 6 show that the performance of the Cliffhanger algorithm is generally on a par with the reference methods. In terms of G-mean scores, Cliffhanger yielded better results than the reference methods on three out of eight data sets. On the other hand, Cliffhanger-T, which imposes a more strict requirement for the hyperparameters, performs comparably with other methods only on Cancer, Wine, Glass, and Vowel data sets. The raw confusion matrix values for both variants of the Cliffhanger algorithm in Table 7 shows that Cliffhanger-T has a significantly lower rate of false alarms (FPR) than the non-thresholded version of the algorithm, at the cost of the ability of discovering positive instances. This makes the Cliffhanger-T better suited for applications where some missed positive instances are acceptable, but false alarms are very costly.

It must be noted that the performance of the Cliffhanger algorithm ultimately depends on the given data: if the plateau of maximal in-class accuracy is close to the point  $(\nu_c, \gamma_c)$  (see Fig. 4), the resulting model is more sensitive for detecting outliers than if the plateau is further away from  $(\nu_c, \gamma_c)$ . For MLCC data, the plateau extends close to  $(\nu_c, \gamma_c)$ , in which case it is justifiable to impose stricter requirements for the hyperparameters. All in all, the Cliffhanger algorithm performs adequately when compared with the results reported by [42]. However, the authors would like to stress that the results for the reference methods in Table 6 were obtained from another study. While the testing methodology of the study was followed as precisely as possible, there might still be differences between data preprocessing, splitting, and selection. Therefore, these results should be viewed as general indicators of the performance of Cliffhanger, and a deeper analysis of the algorithm is a matter of further study.



SAKU LEVIKARI (M'18) was born in 1991 in Finland. He received the B.Sc. and M.Sc. degrees from Lappeenranta University of Technology (LUT), Finland, in May and June of 2018, respectively. He is currently a doctoral student with the Laboratory of Applied Electronics, LUT School of Energy Systems. His main research topics are in the field of applied data analytics and machine learning, with main focus on forecasting and diagnostics on applications such as power electronics, electric grids, and biosignal measurements.



TOMMI J. KÄRKKÄINEN (M'12) was born in 1987 in Finland. He received the B.Sc., M.Sc., and D.sc. degrees from Lappeenranta University of Technology (LUT), Lappeenranta, Finland, in 2010, 2011, and 2015, respectively.

He is currently a Post-Doctoral Researcher with LUT School of Energy Systems. His main research topic is the reliability of power electronic devices and systems, and the utilization of machine learning algorithms to improve the reliability and productivity of various systems.



CAROLINE ANDERSSON (M'10) was born 1983 in Sweden. She received the M.Sc. degree from the faculty of engineering at Lund University (LTH) in Sweden, and her PhD from the Swiss Federal Institute of Technology (ETH) in Zurich, Switzerland. She is currently working as a senior R&D engineer at ABB Traction in Switzerland on the topic of reliability of power electronics. The main focus of her research area is accelerated life testing, physics of failure, and reliability of components and systems.



JUHA TAMMINEN was born in 1980 in Finland. He received his B.Eng. in Electronics in 2006 from Espoo-Vantaa University of Applied Sciences. He is currently working as a design manager at ABB Drives in Finland in the field of production testing. His work concentrates on improving production testing concepts in pursuit of better quality and productivity.



MIKKO NYKYRI (M'19) was born in 1993 in Finland. He received B.Sc. and M.Sc. degrees from Lappeenranta University of Technology (LUT) in 2017 and 2018, respectively. He is currently a doctoral student with the Laboratory of Applied Electronics, LUT School of Energy Systems. His main research topic is utilization of data analytics, machine learning and IoT in industrial predictive maintenance.

Data set	Cliffhanger-T	Cliffhanger	MIES	MSML	SKEW	VM	MD
Cancer	0.791	0.875	<b>0.880</b>	0.634	0.693	0.570	0.845
Heart	0.259	0.622	0.661	<b>0.697</b>	0.655	0.694	0.684
Diabetes	0.129	0.613	0.707	0.722	<b>0.724</b>	0.716	0.414
Sonar	0.034	0.357	<b>0.711</b>	0.679	0.668	0.654	0.692
Wine	<b>0.968</b>	0.965	0.863	0.743	0.849	0.708	0.900
Glass	0.669	0.722	0.721	0.680	0.721	0.628	<b>0.781</b>
Vehicle	0.450	<b>0.870</b>	0.850	0.772	0.739	0.695	0.781
Vowel	0.890	<b>0.943</b>	0.614	0	0	0	0.530

**TABLE 6.** Test results on UCI ML data sets in terms of average G-mean scores across 20 trials. The results for MIES, MSML, SKEW, VM and MD were obtained from [42].

Data set	Metric	Cliffhanger-T	Cliffhanger
Cancer	TPR	1.000	0.934
	TNR	0.569	0.996
	FPR	0.431	0.004
	FNR	0.000	0.067
Heart	TPR	0.969	0.844
	TNR	0.102	0.460
	FPR	0.898	0.540
	FNR	0.03	0.156
Diabetes	TPR	1.000	0.920
	TNR	0.015	0.437
	FPR	0.985	0.563
	FNR	0.000	0.080
Sonar	TPR	1.000	1.000
	TNR	0.000	0.082
	FPR	1.000	0.918
	FNR	0.000	0.000
Wine	TPR	1.000	0.900
	TNR	0.962	1.000
	FPR	0.038	0.000
	FNR	0.000	0.100
Glass	TPR	1.000	0.857
	TNR	0.472	0.590
	FPR	0.528	0.410
	FNR	0.000	0.143
Vehicle	TPR	1.000	0.800
	TNR	0.192	0.862
	FPR	0.808	0.138
	FNR	0.000	0.200
Vowel	TPR	0.700	1.000
	TNR	0.629	1.000
	FPR	0.371	0.000
	FNR	0.300	0.000

**TABLE 7.** Confusion matrix elements (refer to (9)) for the proposed Cliffhanger algorithm in terms of average values across 20 trials.



PERTTI SILVENTOINEN (M'09) was born in Simpele, Finland, in 1965. He received the D.Sc degree from Lappeenranta University of Technology (LUT), Lappeenranta, Finland, in 2001. He became a professor of applied electronics in 2004. His current research interests include power electronics systems in various applications.

...



## ACTA UNIVERSITATIS LAPPEENRANTAENSIS

973. MUSONA, JACKSON. Sustainable entrepreneurial processes in bottom-of-the-pyramid settings. 2021. Diss.
974. NYAMEKYE, PATRICIA. Life cycle cost-driven design for additive manufacturing: the frontier to sustainable manufacturing in laser-based powder bed fusion. 2021. Diss.
975. SALWIN, MARIUSZ. Design of Product-Service Systems in printing industry. 2021. Diss.
976. YU, XINXIN. Contact modelling in multibody applications. 2021. Diss.
977. EL WALI, MOHAMMAD. Sustainability of phosphorus supply chain – circular economy approach. 2021. Diss.
978. PEÑALBA-AGUIRREZABALAGA, CARMELA. Marketing-specific intellectual capital: Conceptualisation, measurement and performance. 2021. Diss.
979. TOTH, ILONA. Thriving in modern knowledge work: Personal resources and challenging job demands as drivers for engagement at work. 2021. Diss.
980. UZHEGOVA, MARIA. Responsible business practices in internationalized SMEs. 2021. Diss.
981. JAISWAL, SURAJ. Coupling multibody dynamics and hydraulic actuators for indirect Kalman filtering and real-time simulation. 2021. Diss.
982. CLAUDELIN, ANNA. Climate change mitigation potential of Finnish households through consumption changes. 2021. Diss.
983. BOZORGMEHRI, BABAK. Finite element formulations for nonlinear beam problems based on the absolute nodal coordinate formulation. 2021. Diss.
984. BOGDANOV, DMITRII. Transition towards optimal renewable energy systems for sustainable development. 2021. Diss.
985. SALTAN, ANDREY. Revealing the state of software-as-a-service pricing. 2021. Diss.
986. FÖHR, JARNO. Raw material supply and its influence on profitability and life-cycle assessment of torrefied pellet production in Finland – Experiences from pilot-scale production. 2021. Diss.
987. MORTAZAVI, SINA. Mechanisms for fostering inclusive innovation at the base of the pyramid for community empowerment - Empirical evidence from the public and private sector. 2021. Diss.
988. CAMPOSANO, JOSÉ CARLOS. Integrating information systems across organizations in the construction industry. 2021. Diss.
989. LAUKALA, TEIJA. Controlling particle morphology in the in-situ formation of precipitated calcium carbonate-fiber composites. 2021. Diss.
990. SILLMAN, JANI. Decoupling protein production from agricultural land use. 2021. Diss.
991. KHADIM, QASIM. Multibody system dynamics driven product processes. 2021. Diss.
992. ABDULKAREEM, MARIAM. Environmental sustainability of geopolymer composites. 2021. Diss.

- 993.** FAROQUE, ANISUR. Prior experience, entrepreneurial outcomes and decision making in internationalization. 2021. Diss.
- 994.** URBANI, MICHELE. Maintenance policies optimization in the Industry 4.0 paradigm. 2021. Diss.
- 995.** LAITINEN, VILLE. Laser powder bed fusion for the manufacture of Ni-Mn-Ga magnetic shape memory alloy actuators. 2021. Diss.
- 996.** PITKÄOJA, ANTTI. Analysis of sorption-enhanced gasification for production of synthetic biofuels from solid biomass. 2021. Diss.
- 997.** MASHLAKOV, ALEKSEI. Flexibility aggregation of local energy systems—interconnecting, forecasting, and scheduling. 2021. Diss.
- 998.** NIKITIN, ALEKSEI. Microwave processes in thin-film multiferroic heterostructures and magnonic crystals. 2021. Diss.
- 999.** VIITALA, MIRKA. The heterogeneous nature of microplastics and the subsequent impacts on reported microplastic concentrations. 2021. Diss.
- 1000.** ASEMOKHA, AGNES. Understanding business model change in international entrepreneurial firms. 2021. Diss.
- 1001.** MUSTO, JIRI. Improving the quality of user-generated content. 2021. Diss.
- 1002.** INKERI, EERO. Modelling of component dynamics and system integration in power-to-gas process. 2021. Diss.
- 1003.** GARIFULLIN, AZAT. Deep Bayesian approach to eye fundus image segmentation. 2021. Diss.
- 1004.** ELFVING, JERE. Direct capture of CO<sub>2</sub> from air using amine-functionalized resin - Effect of humidity in modelling and evaluation of process concepts. 2021. Diss.
- 1005.** KOMLEV, ANTON. Magnetism of metal-free graphene-based materials. 2021. Diss.
- 1006.** RISSANEN, MATTI. EcoGame and Ecosystem Profiler: solutions for business ecosystem management. 2021. Diss.
- 1007.** VANHAMÄKI, SUSANNA. Implementation of circular economy in regional strategies. 2021. Diss.
- 1008.** LEHTINEN, VESA. Organisaation emergentti itseohjautuvuus, case sinfoniaorkesteri: "Miksi orkesteri soittaa hyvin, vaikka sitä johdettaisiin huonosti?". 2022. Diss.
- 1009.** KÄHKÖNEN, TIINA. Employee trust repair in the context of organizational change – identification and measurement of active trust repair practices. 2022. Diss.
- 1010.** AHONEN, AILA. Challenges in sport entrepreneurship: cases in team sport business. 2022. Diss.







ISBN 978-952-335-779-2  
ISBN 978-952-335-780-8 (PDF)  
ISSN-L 1456-4491  
ISSN 1456-4491  
Lappeenranta 2022